2022-12

DYNAMICS, STABILITY, AND MAINTENANCE MECHANISMS OF SUPER LONG-LIVED OCEAN VORTICES

Gulliver, Larry T.

Monterey, CA; Naval Postgraduate School

NAVAL POSTGRADUATE SCHOOL

MONTEREY, CALIFORNIA

DISSERTATION

DYNAMICS, STABILITY, AND MAINTENANCE MECHANISMS OF SUPER LONG-LIVED OCEAN VORTICES

by

Larry T. Gulliver

December 2022

Dissertation Supervisor: Timour Radko

THIS PAGE INTENTIONALLY LEFT BLANK

REPORT DOCUMENTATION PAGE			*Form Approved OMB No. 0704-0188*

1. AGENCY USE ONLY *(Leave blank)*	**2. REPORT DATE** December 2022	**3. REPORT TYPE AND DATES COVERED** Dissertation

4. TITLE AND SUBTITLE
DYNAMICS, STABILITY, AND MAINTENANCE MECHANISMS OF SUPER LONG-LIVED OCEAN VORTICES

5. FUNDING NUMBERS

6. AUTHOR(S) Larry T. Gulliver

7. PERFORMING ORGANIZATION NAME(S) AND ADDRESS(ES)
Naval Postgraduate School
Monterey, CA 93943-5000

8. PERFORMING ORGANIZATION REPORT NUMBER

9. SPONSORING / MONITORING AGENCY NAME(S) AND ADDRESS(ES)
N/A

10. SPONSORING / MONITORING AGENCY REPORT NUMBER

11. SUPPLEMENTARY NOTES The views expressed in this thesis are those of the author and do not reflect the official policy or position of the Department of Defense or the U.S. Government.

12a. DISTRIBUTION / AVAILABILITY STATEMENT
Approved for public release. Distribution is unlimited.

12b. DISTRIBUTION CODE
A

13. ABSTRACT (maximum 200 words)

Ocean variability in the form of coherent mesoscale eddies is still poorly understood despite more than a century of persistent interest and undeniable geophysical significance. These eddies propagate for thousands of miles and distribute vast amounts of nutrients and energy throughout the world's oceans. Most intriguing is how analytical theories and physical arguments suggest that larger vortices, those with radii greater than 75 km, should become unstable and break down in the span of months, yet they are observed to last for years. This research explores two phenomena that contribute to the longevity of these features. First is their ability to adjust to ambient large-scale flows—a feature that determines the eddy's endurance. The second aspect is the role small-scale, irregular topography plays in vortex dynamics. We demonstrate that rough seafloor stabilizes surface-intensified vortices by restricting the motion in the deep layer, thereby allowing the upper ring to perpetuate unhindered. Using an analytical parameterization, we show how this "sandpaper effect" can be accounted for in quasi-geostrophic and full Navier-Stokes models. This research will ultimately allow the U.S. Navy to improve global ocean forecasts without dramatically increasing the spatial resolution.

14. SUBJECT TERMS ocean dynamics, vortices, ocean rings, baroclinic instability, seafloor topography	**15. NUMBER OF PAGES** 115
	16. PRICE CODE

17. SECURITY CLASSIFICATION OF REPORT	**18. SECURITY CLASSIFICATION OF THIS PAGE**	**19. SECURITY CLASSIFICATION OF ABSTRACT**	**20. LIMITATION OF ABSTRACT**
Unclassified	Unclassified	Unclassified	UU

NSN 7540-01-280-5500

Standard Form 298 (Rev. 2-89)
Prescribed by ANSI Std. 239-18

THIS PAGE INTENTIONALLY LEFT BLANK

Approved for public release. Distribution is unlimited.

DYNAMICS, STABILITY, AND MAINTENANCE MECHANISMS OF SUPER LONG-LIVED OCEAN VORTICES

Larry T. Gulliver
Civilian, Department of the Navy
BS, State University of New York, Maritime College, 2006
CERT OF COMPL, University of Plymouth, 2015
MS, Meteorology and Physical Oceanography, Naval Postgraduate School, 2017

Submitted in partial fulfillment of the
requirements for the degree of

DOCTOR OF PHILOSOPHY IN PHYSICAL OCEANOGRAPHY

from the

NAVAL POSTGRADUATE SCHOOL
December 2022

Approved by:
Timour Radko
Department of Oceanography
Dissertation Supervisor
Dissertation Chair

Tetyana Margolina
Department of Oceanography

Gregg Jacobs
Naval Research Laboratory
– Stennis Space Center

Justin M. Brown
Department of Oceanography

Lucas C. Wilcox
Department of
Applied Mathematics

Approved by:
Peter C. Chu
Chair, Department of Oceanography

Joseph P. Hooper
Vice Provost of Academic Affairs

THIS PAGE INTENTIONALLY LEFT BLANK

ABSTRACT

Ocean variability in the form of coherent mesoscale eddies is still poorly understood despite more than a century of persistent interest and undeniable geophysical significance. These eddies propagate for thousands of miles and distribute vast amounts of nutrients and energy throughout the world's oceans. Most intriguing is how analytical theories and physical arguments suggest that larger vortices, those with radii greater than 75 km, should become unstable and break down in the span of months, yet they are observed to last for years. This research explores two phenomena that contribute to the longevity of these features. First is their ability to adjust to ambient large-scale flows—a feature that determines the eddy's endurance. The second aspect is the role small-scale, irregular topography plays in vortex dynamics. We demonstrate that rough seafloor stabilizes surface-intensified vortices by restricting the motion in the deep layer, thereby allowing the upper ring to perpetuate unhindered. Using an analytical parameterization, we show how this "sandpaper effect" can be accounted for in quasi-geostrophic and full Navier-Stokes models. This research will ultimately allow the U.S. Navy to improve global ocean forecasts without dramatically increasing the spatial resolution.

THIS PAGE INTENTIONALLY LEFT BLANK

TABLE OF CONTENTS

LIST OF FIGURES

LIST OF TABLES

THIS PAGE INTENTIONALLY LEFT BLANK

LIST OF ACRONYMS AND ABBREVIATIONS

AACC	Ant-Arctic circumpolar current
AGR	Agulhas rings
BCI	baroclinic instability
CNES	Centre National D'Etudes Spatiales (France)
GSR	Gulf Stream rings
HYCOM	hybrid coordinate ocean model
Meddy	Mediterranean Eddy
MITgcm	Massachusetts Institute of Technology global circulation model
NOAA	National Oceanic and Atmospheric Administration
PIV	Particle Image Velocimetry
PV	potential vorticity
QG	quasi-geostrophic
R_d	radius of deformation
Ro	Rossby number
TAVS	translationally adjusted vortex state

THIS PAGE INTENTIONALLY LEFT BLANK

ACKNOWLEDGMENTS

First, I want to acknowledge that I would not be here today if not for Jesus. Only as a product of His grace and mercy could this once high school drop-out be transformed into a naval officer and PhD. “For I can do everything through Christ, who gives me strength.” — Philippians 4:13.

I also cannot express in words just how deeply grateful I am to Timour Radko for taking me on as his student for these many years, and for believing in me enough to give me the ability to achieve my lifelong dream. Of the hundreds of leaders I’ve met throughout my life, Timour’s humble intellect, calmness in adversity, and adaptable vision make him one of the best people I’ve ever worked for, and a good friend.

I would like to thank the members of my dissertation committee: Gregg, Lucas, Tetyana and Justin, whose encouragement and tutelage were instrumental in making this research a success and in growing me as a scientist. NPS has been like a home to me for several years, and every day I’m grateful and honored to be a part of this institution.

In addition, I wish to thank my friends and family who stood by me through all the late nights and early rises. You’ve provided me with motivation, courage, support and prayers that dragged me through it all, sometimes by the suspenders.

To Nines, my boys, Uncle Tim, Tim B., Sharon, my aunts, uncles, nieces and nephews, and my dog Mitch, whose prayers, reassurance, and companionship have been, and continue to be, the foundation of my successes.

And lastly, I dedicate this to my mother, Theresa, whose pursuit of education late in life was the cornerstone of my drive to step up to the plate and make this dream a reality.

I miss you, mom and dad. This one is for you.

THIS PAGE INTENTIONALLY LEFT BLANK

I. INTRODUCTION

The purpose of this investigation is to improve our understanding of mesoscale ocean vortices, otherwise known as coherent eddies or rings. This study specifically strives to address the long-standing longevity conundrum: Why the ocean rings last for several years, seemingly violating prevailing theoretical views on their stability. Here I provide the reader with a brief history of eddy research followed by an overview of the present contribution. This discussion inevitably conveys the alluring nature of vortex theory, which for many decades compelled intense interest from scientists across a vast array of disciplines. The reasons for this attention, both practical and esthetical, will become apparent after reviewing the spectrum of applications involving ocean eddies.

A. A BRIEF HISTORY OF EDDY RESEARCH

Eddies have had a sizeable breadth of formal definitions, which attests to their variability in the ocean. According to NOAA, an eddy is defined as a "circular current of water." Tomzack and Godfrey (2003)'s definition adds that it is "a closed circular or elliptical system that can be either cyclonic or anti-cyclonic" (Tomczak and Godfrey 2003). An even broader definition is given by Robinson (2012), which includes "All types of variable flow" such as meanders, cast-off rings, advective lenses and planetary waves. Other definitions often associate the term "eddies" with features that have strong vorticity signatures but possibly lack cohesive structure. For instance, the widely used Okubo-Wiess condition (Okubo 1970; Weiss 1991) emphasizes the excess of vorticity relative to the strain rate in coherent eddies. Along these lines, Haller (2005) developed an objective definition of a coherent vortex as "a set of fluid trajectories along which the strain acceleration tensor is indefinite over directions of zero strain." This more formal mathematical definition restricts the term "eddy" to a set of stable elliptical flows, which provides us with a more suitable definition for this paper.

The main thrust of our efforts is on long-lived nearly axisymmetric structures that maintain their shape and transport water masses trapped in their interior. These structures can be as large as 150 km in diameter with depths of 1000 m, like the Agulhas rings, or as

small as intra-thermocline lenses which are found within the thermocline ranging 25 km across and only a couple hundred meters thick (Dugan et al. 1982). Eddies travel in various directions, and with different physical properties depending on background flow, cause of formation, size, and latitude. A better understanding of these plentiful ocean features is afforded by the chronological review of their discovery, subsequent observations, and theoretical ideas.

The first documented reference to ocean rings is attributed to Benjamin Franklin's grandnephew, Jonathan Williams. While taking ocean temperatures on a voyage from Halifax to New York in the summer of 1790, Williams found a region where the Gulf-Stream temperatures were too far north. He assumed that it must be "whirlpools of the eddy of the gulph stream" (Williams 1793; Robinson 2012). It was not until the 1930s that P.E. Church discovered a similar phenomenon while reviewing thermograph records from ships crossing the Atlantic (Church 1932, 1937). In 1936, Iselin investigated these features while taking salinity and temperature readings from *The Atlantis* and concluded them to be permanent (Iselin 1936). By the 1940s he and other researchers began using LORAN and bathythermographs to track and collect data on, what they discovered to be, Gulf Stream "meanders" (Talley et al. 2011; Robinson 2012).

With the creation of National Oceanic and Atmospheric Administration (NOAA), the 1970s was launched as the International Decade of Ocean Exploration. This period also coincided with a series of technological breakthroughs in the development of ocean-observing instrumentation. New observational survey equipment such as the eXpendable Bathy-Thermograph (XBT) and SOund Fixing And Ranging (SOFAR or RAFOS) floats collected data on the vertical structure of eddies. Another major advancement in this area was the invention of satellite-tracked drifting buoys, and Seasat-A was launched into space with infrared sensing capability (Robinson 2012; Rossby et al. 1986; Pinet 2019). The 1970s was also a decade of several ocean research expeditions, such as the Mid-Ocean Dynamics Experiment (MODE) and POLYMODE from which spawned Polygon 70, a Russian experiment that revealed the widespread presence of synoptic scale ocean eddies (Talley, 2011). Between 1976–1977, six cold-core Gulf Stream Rings (GSRs) were tracked in four expeditions by a team of eight multi-disciplinary researchers known as the Ring

Group (1981). Research such as this initiated the discovery of various other types of vortices, including intra-thermocline saline lenses (Armi and Zenk 1984; Dugan et al. 1982). Eddies were deemed to be of such importance that the Naval Oceanographic Office began publishing *The Gulf Stream*, a monthly summary dedicated to observations of GSRs (Robinson 2012).

The predominantly observational research of ocean rings from the 1970s was soon followed by analytical efforts with many theories developed to explain the physics of coherent eddies using governing principles. Motivated by measurements of GSRs, McWilliams and Flierl (1979) developed a first predictive and testable theory of eddies. This model even attempted to represent eddy signatures in the abyssal zone, where observational data were, and still are, sparse. They used a quasi-geostrophic, one and two layer theoretical model to examine the propagation of a vortex through a motionless medium. They concluded that: 1) an eddy's center of mass should move westward at the rate equal to the speed of long Rossby waves, 2) the meridional drift and westward propagation tendency is affected by interplay between the barotropic and baroclinic modes, and 3) the decay of vortices is controlled by the potential vorticity and lateral friction.

Doron Nof (1985) extended this research by analyzing isolated vortices in three-layer analytical models. His theory was based on Euler's momentum theorem, which he applied to a Gaussian vortex and a lens with either bottom slope or β-effect, i.e., the change in Coriolis force with latitude (Nof, 1981). The model explained the westward migration of the individual vortices due to planetary lift. Planetary lift is a side-acting pressure force that develops from the geostrophic balance of the displaced fluid around the eddy that acts poleward but forces westward motion due to the Coriolis effect. While pioneering, this theoretical model was still oversimplified. In particular, it ignored influences from the deep layer, such as the effects of variable topography and the advection by ambient flows, all of which can ultimately affect vortex motion.

Mathieu Mory (1985) furthered Nof's integral model in experiments where eddies were placed on the bottom and surface of the ocean respectively, demonstrating the possibility for eastward flow under certain conditions. Killworth (1986) extended this work

even further, developing an N-layer shallow water model to determine eddy translational velocity. Assuming a compact eddy pattern, the rigid lid approximation, and a motionless bottom layer he was able to predict eddy zonal velocity. The generality of these calculations, despite the simplifications of the model, made this discovery quite astounding. It is interesting that these theories assumed uniformly propagating vortices. However, the very existence of such structures was uncertain at that time since observational capabilities were limited, and high-performance computing was in its infancy.

Despite these advances in the theoretical understanding of eddies, the questions regarding stability and longevity had yet to be resolved. The celebrated theorem by Charney and Stern (1962) declared that if the potential vorticity (PV) gradient of a parallel flow maintains the same sign throughout the entire depth of a water column, the system will be baroclinically stable. Dritschel (1988) generalized this theory to include axisymmetric circulation patterns. However, analytical arguments for large rings demand that there would be a reversal of PV gradient at some depth. Since mesoscale vorties are known for their longevity and resilience to external perturbations, the question can be asked: what mechanism reduces baroclinic effects and stabilizes the ocean vortices?

B. EDDY BEHAVIOR AND SIGNIFICANCE

Eddies are often generated by baroclinic instability, which transfers potential energy stored in sloping isopycnals into kinetic reservoir and, ultimately, leads to mixing. The instabilities of major large-scale currents like the Gulf Stream and Kuroshio often create circular flows with distinct water-masses trapped within their cores (Kamenkovich et al. 1986). Satellite data has also allowed us to discover more about eddy behavior. Rings observed in the Gulf of Mexico and in the vicinity of the Agulhas Retroflection (AGR) commonly have radii in excess of 150 km (Olson 1991; Byrne et al. 1995). Many ocean rings have been tracked by satellite altimetry for well over 4 years (Chen and Han 2019; Cheng et al. 2014). Cyclonic eddies tend to drift meridionally northward while anticyclonic eddies drift southward, an effect attributed to the conservation of potential vorticity and the

variation in the Coriolis parameter across the eddy (Chelton et al. 2007, 2011; Fu et al. 2010; Chen and Han 2019).

Eddy phenomenology is based on several observable characteristics (Olson 1991). Other than core temperature and size, they can also be classified by the point of origin, by the parent current, or by their unique temperature-salinity profiles. Some eddies emerge from growing meanders such as GSR and AGR, while others owe their existence to the effects of wind, topography, ocean fronts or eddy/mean-field interactions (Dugan et al. 1982; Jia et al. 2011). Consequentially, some eddies are surface-intensified, yet others represent intra-thermocline lenses with very limited expression at the sea-surface. Meddies, for example, develop from warm and salty Mediterranean waters that overflow from the strait of Gibraltar onto the Iberian slope (Radko and Sisti 2017). These eddies last for years as they travel across the Sargasso Sea at depths of ~1000 m (Ienna et al. 2022).

Another interesting fact about eddies is how they distribute the properties of seawater across the World Ocean. Because they are numerous, diverse, long-lasting and large, they can transfer heat, salinity, pollutants and nutrients over thousands of miles (Byrne et al. 1995; Ganachaud and Wunsch 2003; Griffies et al. 2015). Recent observations from Argos floats, which have made it possible to analyze over 250 eddies, suggest that eddy heat transport across the 45° latitude may be as high as ½ of the total heat transport in the ocean, or 0.8 petawatts (Sun et al. 2019). At any given time, thousands of eddies can be identified and tracked at the sea-surface alone (Fu et al. 2010). This ability of eddies to transfer water masses into regions with dissimilar properties has major repercussions for climate science, as eddy-induced heat transport may play a key role in ice sheet melting (Maslowski and Lipscomb 2003; Griffies et al. 2015). These eddies also transport nutrients and sea life that affects the larger ocean biome (Bakun 2006; Godø et al. 2012; Robinson 2012; Watanabe et al. 2014). Most recently, the observations of white sharks tracked in the Gulf Stream revealed that they extensively use anticyclonic (warm-core) eddies where prey is easily accessible and the need for thermoregulation is reduced (Gaube et al. 2018).

C. THE PRESENT CONTRIBUTION

What once was mere theory can now be proven, or disproven, through technological advancements. Aldous Huxley wrote once "Technological progress has merely provided us with more efficient means of going backward" (Huxley 2012). Although his words contain an element of sarcasm, the concept of using modern technology to revisit old-school wisdom represents a perfectly valid approach. This philosophy, which encourages the application of cutting-edge methods to previously garnered principles, permeates the present attempt to address the age-old but still unresolved puzzle of eddy longevity. With this approach, this paper explores three controlling mechanisms for vortex stability: (i) the ability to adjust, (ii) stability and (iii) topography-induced spin-down.

This dissertation is organized as follows. Chapter II explores the dynamics of large-scale coherent vortices embedded in large-scale shear flows. This effort is motivated by the lack of consistency between observed vortex speeds and predictions of earlier models, which often disagree by as much as an order of magnitude. The proposed analytical theory builds on seminal works of Nof (1981, 1983) and Killworth (1986) who analyzed the eddy drift rates in a quiescent ocean. The present model, however, incorporates the effects of vortex advection by large-scale shear. One of the key questions addressed is the possibility of quasi-uniform vortex propagation, an assumption that is usually taken for granted in earlier drift-rate theories. The tendency of eddies to evolve towards this translationally adjusted vortex state (TAVS) is highly dependent on flow direction and the presence of background instability. In addition, we discover the direct link between vortex's ability to conform to this adjusted state and its longevity.

Chapters III and IV explore the effects of irregular small-scale topography on eddy stability and dynamics. The ultimate goal is the development of rigorous parameterizations of the effects of rough topography in global circulation models, such as HyCOM (Hybrid Co-ordinate Ocean Model). This development, in turn, is expected to improve operational forecasts without a substantial increase in computational cost. Chapter III proposes that the bottom roughness can dramatically enhance the stability of ocean eddies. This stabilization is invoked as a plausible explanation for why large ocean vortices retain their structure for

several years. By systematically exploring various topographic heights, including a flat bottom case, it is shown that increasing the height of the topography increases vortex lifespan in what is now known as the "sandpaper effect." In addition, a critical depth variance exists above which the vortex is linearly stable, and this condition is commonly met in the ocean.

Chapter IV builds upon the previous chapter by increasing the complexity and realism of the model, which integrates the full Navier–Stokes equations using MITgcm (Massachusetts Institute of Technology global circulation model). We also address the possibility of laboratory modeling of the sandpaper effect. To this end, we perform a series of spin-down "virtual laboratory experiments" modeling the flow over irregular topography in the rotating tank. This virtual laboratory study provides guidance for future rotating tank experiments and flow analysis using particle image velocimetry (PIV). Additionally, novel analytical descriptions of the sandpaper effect are developed and validated by numerics. Finally, Chapter V contains the conclusions of this dissertation.

THIS PAGE INTENTIONALLY LEFT BLANK

II. ON THE PROPAGATION AND TRANSLATIONAL ADJUSTMENT OF ISOLATED VORTICES IN LARGE-SCALE SHEAR FLOWS

A. INTRODUCTION

Coherent vortices are fascinating ocean features. They affect the ambient environment and have an immense impact on the dynamics of the world's oceans (Kamenkovich et al. 1986; Robinson 2012; Griffies et al. 2015; Vallis 2017). Eddies can propagate for thousands of miles from their points of origin and last anywhere from a few weeks to several years (Chelton et al. 2011; Chen and Han 2019). Due to their strength, size, propagation range, and quantity, they play a major role in the transport of energy, heat, pollutants, and nutrients (Robinson 2012; Byrne et al. 1995; Klocker and Abernathey 2014; Griffies et al. 2015; Vallis 2017; Brach et al. 2018). The present study strives to improve our understanding of eddy motion patterns and longevity, which can ultimately enhance their representation in the predictive climate models.

The first documented observation of a coherent long-lived ocean vortex dates back to the discovery of a warm-core eddy in 1790 by Jonathan Williams—Benjamin Franklin's grandnephew (Williams 1793; Robinson 2012). However, the widespread appreciation of the abundance and significance of coherent mesoscale vortices in the ocean interior came about only in the 1970s. A series of breakthroughs in this area was stimulated by major field programs (MODE group 1978; Ring Group 1981) that utilized the advancements in oceanographic instrumentation such as the eXpendable Bathy-Thermograph (XBT) and long-range Swallow, or SOund Fixing And Ranging (SOFAR and RAFOS), floats (Swallow 1955; Rossby et al. 1986; Robinson 2012). More recently, researchers have used satellite altimetry to locate and track eddies throughout the ocean (Chelton et al. 2007,

2011; Sangrà et al. 2009; Samelson et al. 2014; Beron-Vera et al. 2013; Abernathey and Haller 2018; Aguedjou et al. 2019). The technological progress in this area was accompanied by the concurrent development of effective algorithms for the analysis of satellite measurements (Isern-Fontanet et al. 2004; Abernathey and Marshall 2013). One of several intriguing findings brought about by satellite-based analyses is the increased longevity of vortices embedded in westward background flows, particularly in trade wind latitudes (Sangrà et al. 2009; Dilmahamod et al. 2018; Chen and Han 2019). The mechanisms causing the dissimilar evolution of vortices in predominantly westward and eastward currents are yet to be fully explained (Sutyrin and Radko 2021) and this issue will be addressed in the present work.

Numerous attempts have been made to rationalize the observed properties of coherent vortices using dynamically transparent theoretical models (Radko and Stern 2000; Early et al. 2011; Radko 2020, 2021). In particular, observations reveal that eddy propagation is predominantly westward unless advected eastward by stronger ocean currents, as seen in the Gulf Stream and ACC (Fu et al. 2010; Chen and Han 2019). Current vortex theories rationalize this tendency from first principles and offer analytical estimates of drift rates (McWilliams and Flierl 1979; Nof 1983; Killworth 1986; Cushman-Roisin et al. 1990; Radko and Stern 1999; Klocker and Abernathey 2014). While the general theory of vortex propagation is still not fully developed, there is a broad consensus on the key physical mechanisms at play. Translation of rings is caused by the latitudinal variation in Coriolis parameter, advection by large-scale currents, as well as the effects of winds and topography (Rossby 1948; Olson 1991; Cornillon et al. 1989; Nof et al. 2011).

The key limitation of classical drift-rate theories is the lack of uniform quantitative consistency of their predictions with the observed speeds of coherent mesoscale vortices. While oceanic vortices generally exhibit westward propagation tendencies, theoretical predictions and observations often differ by as much as an order of magnitude (Cornillon et al. 1989; Chassignet et al. 1990; Byrne et al. 1995; Nof et al. 2011). The most natural and commonly invoked explanation of such disagreements is the advection by background flows (Chen and Han 2019). Most drift-rate models assume from the outset that the vortex exterior is largely quiescent (McWilliams and Flierl 1979; Nof 1983, 1981; Killworth

1986; Nycander 1988; Cushman-Roisin et al. 1990; Benilov 1996). This assumption is likely based on the expectation that the advective effects of the background flow field could be trivially incorporated a posteriori, by superposing the beta-induced and advective tendencies. The present study questions this assumption and attempts to generalize earlier drift-rate theories by explicitly including background zonal shears in model formulation. We discover that the evolution of isolated vortices in large-scale flows can be surprisingly complex and counterintuitive. In addition to the direct advective effects, geostrophically balanced large-scale currents are associated with isopycnal potential vorticity (PV) gradients that could be comparable to the planetary beta-effect. These PV gradients strongly influence the propagation of coherent vortices, offsetting the direct advective tendency of large-scale flows. On the other hand, we find that background shears can strongly affect the vortex dynamics and propagation by substantially modifying the vortex structure.

Another major assumption of most drift-rate theories (e.g., Killworth, 1986) is the existence of adjusted quasi-steady vortical states, characterized by uniform zonal motion. The present investigation shows that while some vortices indeed tend to evolve towards the "ultimate" equilibrium states, this tendency is strongly regime-dependent, and the existence of such balanced configurations should not be taken for granted. In particular, vortices embedded in westward flows are more likely to equilibrate than their counterparts in eastward flows, which usually spin down and disintegrate more rapidly. This finding could be viewed as a plausible explanation for the observed tendency of westward flows to harbor particularly long-lived vortices (e.g., Fu et al. 2010; Aguedjou et al. 2019; Chaigneau et al. 2011; Chen and Han 2019; Dilmahamod et al. 2018).

Yet another uncertain aspect of extant drift-rate theories is their disregard of transient ambient variability. In the ocean, coherent vortices propagate through an active and disorganized mesoscale field, which is induced and maintained by the baroclinic instability of background currents. Thus, the question arises whether a significant revision of drift-rate models is required to take this variability into account. We perform a series of simulations with baroclinically unstable background flows, characterized by representative levels of mesoscale variability, and explore its impact on the vortex propagation velocities.

In this regard, our findings are generally comforting. The effects of mesoscale variability on the drift rates of isolated vortices are secondary, which enhances the prospects of describing their motion patterns using explicit analytical models.

This manuscript is organized as follows. The propagation and translational adjustment of long-lived mesoscale vortices are studied using an isopycnal quasi-geostrophic reduced gravity β-plane model, which is described in Sec. 2. Sec. 3 develops an analytical framework for vortex propagation in zonal large-scale shears. Sections 4 and 5 present a series of numerical experiments that explore the dynamics of isolated vortices in baroclinically stable westward and eastward shear flows, respectively. In particular, we examine a wide range of governing parameters to determine, in each case, whether or not the isolated vortex evolves to a quasi-equilibrium state characterized by uniform zonal motion. The latter configuration will be referred to as the Translationally Adjusted Vortex State (TAVS). We argue that the vortex longevity is contingent on its ability to approach the TAVS limit. Sec. 6 examines the evolution of vortices in eddying, baroclinically unstable flows. The objective of this section is to determine the applicability of the drift-rate theories to turbulent systems that are more representative of typical oceanic conditions. We summarize our results and draw conclusions in Sec. 7.

B. FORMULATION

This study is based on the quasi-geostrophic *n*-and-a-half layer model (e.g., Pedlosky 1987), which represents flow in *n* active layers overlying the deep and motionless abyssal zone. We assume that the flow pattern includes a laterally homogeneous zonal current—a configuration maintained indefinitely by the mechanical and thermodynamic forcing of the system. The laterally uniform basic flow approximation is commonly employed in theoretical vortex propagation models (e.g., Vandermeirsh et al. 2002; Sutyrin et al. 2021). This approximation applies to eddies located in broad interior flows, outside of swift and narrow currents. It is justified by recognizing the substantial differences in scales of coherent vortices and the background circulation patterns in the interior of ocean gyres.

In the following model, U_i^*, H_i^*, and ρ_i^* represent the basic speed, depth, and density of layer i, where $i = 1,...,n$. The asterisks denote dimensional quantities. Theoretical development is simplified by assuming identical density differences between adjacent layers $\Delta\rho^* = \rho_i^* - \rho_{i-1}^*$ although the generalization to the variable $\Delta\rho$ is relatively straightforward. In this configuration, the governing quasi-geostrophic equations (Charney 1948, 1971; Pedlosky 1983) take the form:

$$\begin{cases} \dfrac{\partial Q_1^*}{\partial t^*} + J(\Psi_1^*, Q_1^*) = \nu^* \nabla^4 \Psi_1^*, \\ \dfrac{\partial Q_i^*}{\partial t^*} + J(\Psi_i^*, Q_i^*) = \nu^* \nabla^4 \Psi_i^*, \quad i = 2,...,n-1 \\ \dfrac{\partial Q_n^*}{\partial t^*} + J(\Psi_n^*, Q_n^*) = \nu^* \nabla^4 \Psi_n^*, \end{cases} \tag{1}$$

where Ψ_i^* is the streamfunction, $g'^* = g\dfrac{\Delta\rho^*}{\rho_0^*}$, $\beta^* = \dfrac{\partial f^*}{\partial y^*} = const$, and ν^* is the lateral viscosity. Q_i^* denotes the potential vorticity (PV) in layer i, which is expressed in terms of streamfunctions as follows:

$$\begin{cases} Q_1^* = \nabla^2 \Psi_1^* + \dfrac{f_0^{*2}}{g'^* H_1^*}\left(\Psi_2^* - \Psi_1^*\right) + \beta^* y^* \\ Q_i^* = \nabla^2 \Psi_i^* + \dfrac{f_0^{*2}}{g'^* H_i^*}\left(\Psi_{i-1}^* + \Psi_{i+1}^* - 2\Psi_i^*\right) + \beta^* y^* \qquad i = 2,...,n-1 \\ Q_n^* = \nabla^2 \Psi_n^* + \dfrac{f_0^{*2}}{g'^* H_n^*}\left(\Psi_{n-1}^* - 2\Psi_n^*\right) + \beta^* y^*. \end{cases} \tag{2}$$

The total zonal velocities in each layer are separated into background components $\left(U_i^*, 0\right)$ and perturbations $\left(u_i^*, v_i^*\right)$. These velocity fields are readily expressed in terms of streamfunction: $\left(U_i^* + u_i^*, v_i^*\right) = \left(-\dfrac{\partial \Psi_i^*}{\partial y^*}, \dfrac{\partial \Psi_i^*}{\partial x^*}\right)$. The net streamfunction in each layer (Ψ_i^*) is similarly separated into the basic state representing the background current $(\overline{\Psi}_i^* = -U_i^* y^*)$ and the perturbation (ψ_i^*). To reduce the number of controlling parameters,

we non-dimensionalize the governing equations using the speed of the basic current in the first layer $\left|U_1^*\right|$ as the unit of velocity. The unit of length is the radius of deformation based on the net depth of the thermocline $H^* = \sum_{i=1}^{n} H_i^*$:

$$R_d^* \equiv \frac{\sqrt{g'^* H^*}}{f_0^*} \tag{3}$$

where f_0^* is the reference value of the Coriolis parameter (f^*) in the beta-plane approximation.

The governing equations are then expressed in terms of perturbations ψ_i^*, and subsequently non-dimensionalized, resulting in

$$\begin{cases} \dfrac{\partial q_1}{\partial t} + J(\psi_1, q_1) + \beta \dfrac{\partial \psi_1}{\partial x} + \delta F_1 (U_1 - U_2) \dfrac{\partial \psi_1}{\partial x} + \delta \dfrac{\partial q_1}{\partial x} = \nu \nabla^4 \psi_1, \\ \dfrac{\partial q_i}{\partial t} + J(\psi_i, q_i) + \beta \dfrac{\partial \psi_i}{\partial x} + \delta F_i (2U_i - U_{i-1} - U_{i+1}) \dfrac{\partial \psi_i}{\partial x} + \delta U_i \dfrac{\partial q_i}{\partial x} = \nu \nabla^4 \psi_i, \quad i = 2, ..., n\text{-}1 \\ \dfrac{\partial q_n}{\partial t} + J(\psi_n, q_n) + \beta \dfrac{\partial \psi_n}{\partial x} + \delta F_n (2U_n - U_{n-1}) \dfrac{\partial \psi_n}{\partial x} + \delta U_n \dfrac{\partial q_n}{\partial x} = \nu \nabla^4 \psi_n, \end{cases} \tag{4}$$

where $F_i = \dfrac{H^*}{H_i^*}$, $U_i = \dfrac{U_i^*}{U_1^*}$, $\beta = \dfrac{\beta^* R_d^{*2}}{\left|U_1^*\right|}$, $\nu = \dfrac{\nu^*}{R_d^* \left|U_1^*\right|}$, and $\delta = \dfrac{U_1^*}{\left|U_1^*\right|} = \pm 1$ are the governing parameters. The PV perturbations in non-dimensional form reduce to

$$\begin{cases} q_1 = \nabla^2 \psi_1 + F_1 (\psi_2 - \psi_1), \\ q_i = \nabla^2 \psi_i + F_i (\psi_{i+1} + \psi_{i-1} - 2\psi_i), \quad i = 2, ..., n\text{-}1 \text{ .} \\ q_n = \nabla^2 \psi_n + F_n (\psi_{n-1} - 2\psi_n) \text{ .} \end{cases} \tag{5}$$

C. THEORETICAL MODEL OF PROPAGATION

The model (4) is used here to explore the propagation tendencies of coherent long-lived vortices embedded in large-scale zonal shear flows. We shall focus on the configurations where the strength of vertical shear is insufficient to induce the vortex splitting. The ability of coherent vortices to withstand the shearing action of background flows was considered by Vandermeirsh et al. (2002) in the oceanographic context and by Reasor et al. (2004) for tropical cyclones in the atmosphere. In particular, Vandermeirsh et al. (2002) proposed a physics-based splitting criterion and concluded that the vertical shear in most large-scale flows is below the critical strength required for vortex splitting. This conclusion is further supported by our numerical simulations (Sections D-F), in which all vortices evolved as single coherent entities.

Numerous theories (McWilliams and Flierl 1979; Nof 1981, 1983; Mory 1985; Killworth 1986; Cushman-Roisin et al. 1990; Benilov 1996) attempt to predict the translational velocities of isolated vortices in the quiescent ocean. A conspicuously effective approach to the problem involves formulating integral relationships between the broadly defined "average" speed of a vortex, its spatial structure, and the background stratification. The first and simplest example of this approach is the centroid theorem for an isolated vortex in the equivalent-barotropic ocean (McWilliams and Flierl 1979). One of the key results of this study is an explicit expression for the propagation speed of the center of vortex mass anomaly, which was obtained by multiplying the quasi-geostrophic PV equation by (x, y) and integrating the result over the horizontal plane. The centroid theorem predicts that the center of mass propagates westward with the speed of long Rossby waves. Somewhat counterintuitively, this result is still valid for vortices embedded in steady large-scale flows. This "anti-Doppler" effect (Nycander 1994) is caused by the variation in the first layer thickness associated with the large-scale geostrophic current. The resulting PV gradient induces motion in the direction opposite to the ambient current, thereby canceling the advective tendency of the large-scale flow.

The following model generalizes the centroid theorem to more complex and realistic multilayer systems in the presence of a zonal shear flow. For that, we consider relatively compact coherent vortices, characterized by a rapid decrease in the far-field: $|\psi| \le O\left(r^{-2}\right)$. To evaluate the zonal propagation velocities, the governing equations are multiplied by x and integrated horizontally, yielding

$$\begin{cases} \dfrac{\partial}{\partial t}\left(F_1 \int x(\psi_2 - \psi_1)dxdy\right) - \left[\beta + \delta F_1 (U_1 - U_2)\right] \cdot \int \psi_1 dxdy - \delta U_1 F_1 \int (\psi_2 - \psi_1)dxdy = 0, \\ \dfrac{\partial}{\partial t}\left(F_i \int x(\psi_{i+1} + \psi_{i-1} - 2\psi_i)dxdy\right) - \left[\beta + \delta F_i (2U_i - U_{i-1} - U_{i+1})\right] \cdot \int \psi_i dxdy - \delta U_i F_i \int (\psi_{i+1} + \psi_{i-1} - 2\psi_i)dxdy = 0, \\ \dfrac{\partial}{\partial t}\left(F_n \int x(\psi_{n-1} - 2\psi_n)dxdy\right) - \left[\beta + \delta F_n (2U_n - U_{n-1})\right] \cdot \int \psi_n dxdy - \delta U_n F_n \int (\psi_{n-1} - 2\psi_n)dxdy = 0 \,, \end{cases}$$

(6)

where $i = 2,...,n\text{-}1$.

The interpretation of the integral relation (6) is simplified when we recognize that

$$S_i \equiv \int \psi_i \, dxdy, \quad i = 1,...,n \tag{7}$$

represents the strength of circulation in each layer and

$$x_{ci} \equiv \frac{\int x\psi_i \, dxdy}{\int \psi_i \, dxdy}, \quad i = 1,...,n \tag{8}$$

is the x-coordinate of the streamfunction centroid in layer i. The rate of change in this quantity represents the speed of the zonal displacement of the vortex center,

$$c_i = \frac{dx_{ci}}{dt} = S_i^{-1} \frac{\partial}{\partial t} \int x\psi_i \, dxdy \;, \tag{9}$$

provided that the integrated thickness anomaly in each layer is preserved in time and therefore $S_i = const$. Using (7) and (9), we rewrite the integral balances (6) as follows:

$$\begin{cases} F_1\left(c_2 S_2 - c_1 S_1\right) = \left[\beta + \delta F_1 (U_1 - U_2)\right] S_1 + \delta U_1 F_1 (S_2 - S_1), \\ F_i\left(c_{i-1} S_{i-1} + c_{i+1} S_{i+1} - 2 c_i S_i\right) = \left[\beta + \delta F_i (2U_i - U_{i-1} - U_{i+1})\right] \cdot S_i + \delta U_i F_i (S_{i-1} + S_{i+1} - 2S_i) = 0, \\ F_n\left(c_{n-1} S_{n-1} - 2 c_n S_n\right) = \left[\beta + \delta F_n (2U_n - U_{n-1})\right] \cdot S_n + \delta U_n F_n (S_{n-1} - 2S_n) . \end{cases}$$

(10)

Note that (10) represents a linear homogeneous system for S_i and therefore vector $[S_1, S_2, ...S_n]^T$ lies in the null-space of the corresponding $n \times n$ matrix.

For any assumed vortex structure, characterized by a set of prescribed values of S_i, the system (10) yields a solution with *n* distinct – and generally dissimilar – values of the translational velocity c_i. This result appears to be counter-intuitive in view of the longevity and resilience of oceanic vortices, which can survive for several years. The translation of such vortices as coherent entities implies that the propagation velocities in each layer (c_i) should be equal:

$$c_1 = c_2 = ... = c_n \ . \tag{11}$$

Such a scenario, in turn, implies that the initially introduced distribution of circulation strengths in different layers (S_i) would undergo a major readjustment, creating a new vortex state that conforms to the condition (11). The present investigation attempts to shed light on the dynamics of such a transformation, which is referred to hereafter as the "translational adjustment," and on the selection of the preferred vortex speed.

An alternative approach to the drift-rate problem (e.g., Killworth 1986) involves the derivation of a single relation for the propagation velocity that reflects the net force balance on the vortex as a whole. In this spirit, instead of focusing on individual layers, we integrate (6) over the entire volume as done by Killworth (1986) for the shallow water model, which yields

$$c = -\beta \frac{\sum_{i=1}^{n} S_i F_i^{-1}}{S_n} \ . \tag{12}$$

Remarkably, the drift rate in this model is uniquely determined by the eddy pattern (S_i), stratification (F_i), and the beta-effect, while the background flow has no direct impact on c. The eddy propagation is westward for these simulations, regardless of the background flow direction. This finding represents a spectacular manifestation of the "anti-Doppler" effect, which has been introduced in the context of the equivalent-barotropic model (Nycander 1994) but here is shown to be much more general.

To be more specific—and conform to the following numerical simulations (Sections 4–6)— we also list the theoretical results for the two-and-a-half (n=2) model, which reduces (10) to

$$\begin{cases} F_1\left(c_2S_2 - c_1S_1\right) = \beta S_1 - \delta U_2 F_1 S_1 + \delta U_1 F_1 S_2, \\ F_2\left(c_1S_1 - 2c_2S_2\right) = \beta S_2 - \delta U_1 F_2 S_2 + \delta U_2 F_2 S_1 . \end{cases} \tag{13}$$

This system can be readily solved for the propagation speeds of the active layers:

$$\begin{aligned} c_1 &= \frac{\delta U_2 F_1 F_2 S_1 - \delta U_1 F_1 F_2 S_2 - 2\beta F_2 S_1 - \beta F_1 S_2}{F_1 F_2 S_1} \\ c_2 &= -\frac{\beta(F_2 S_1 + F_1 S_2)}{F_2 F_1 S_2}. \end{aligned} \tag{14}$$

It is interesting that when the integral expression (12) is re-written for n = 2, we find that

$$c = c_2. \tag{15}$$

This indicates that the eddy's full-column translational velocity (12) is controlled by the vorticity balance for the lowest active layer. This result is surprising and counterintuitive, as one would expect the propagation velocity to be determined by the combination of processes in all density layers. Eq. (15), however, suggests that the effects of the upper layers on the drift rate are indirect and involve the modification of the eddy pattern. The resulting changes in (S_1, S_2), in turn, influence the propagation speed. It should also be emphasized that (15) pertains only to adjusted, uniformly translating

vortices. As will be seen shortly (Sections 4–6), such adjusted states may not always be achieved.

While the vertical vortex pattern in (13)-(14) is expressed in terms of the integrated streamfunction (S_i), another—and perhaps more convenient—representation is based on the PV integrals (B_i):

$$B_i = \int q_i \, dxdy \, . \tag{16}$$

These streamfunction and PV signatures can be readily linked using **(5)**:

$$\begin{aligned} B_1 &= \left(F_1 S_2 - F_1 S_1\right) \\ B_2 &= \left(F_2 S_1 - 2F_2 S_2\right). \end{aligned} \tag{17}$$

If the vortex eventually evolves to uniform quasi-steady drift—the assumption that should not be taken for granted—then $c_1 = c_2$. This condition can therefore be used as a quantitative criterion for the translational adjustment.

To express this necessary condition for the Translationally Adjusted Vortex State (TAVS) in terms of (B_1,B_2), we combine (11), (13), and (17), which yields

$$B_2 = \frac{(-3\delta U_2 F_1 F_2 + 2\delta U_1 F_1 F_2 - \beta F_1 + 2\beta F_2 \pm \sqrt{D}) \cdot B_1}{2F_1(\delta U_2 F_1 - \delta U_1 F_1 - \beta)} \tag{18}$$

where

$$D = \delta^2 U_2^2 F_1^2 F_2^2 + 2\delta\beta U_2 F_1^2 F_2 - 4\delta\beta U_2 F_1 F_2^2 + 4\delta\beta U_1 F_1 F_2^2 + \beta^2 F_2^2 \, . \tag{19}$$

Thus, real solutions for (B_1,B_2) are possible only if the discriminant D is positive. On the other hand, if $D<0$, no real solutions can be found. This indicates that the very existence of TAVS is not guaranteed but depends on the background stratification and the vertical shear profile. Since U_1, U_2, F_1, F_2 and δ are prescribed for each simulation, the temporal variation of $B_1(t)$ and $B_2(t)$ determines whether the vortex tends to undergo the adjustment towards the quasi-equilibrium state (18).

Finally, before exploring a plethora of evolutionary scenarios using numerical simulations, it becomes necessary to specify conditions for baroclinic stability/instability of the basic flow. The celebrated Charney-Stern theorem attributes the instability of inviscid zonal flows to the change in the sign of the basic PV gradients (Charney and Stern 1962). The meridional gradients of the net basic PV (β_i) in layers *i*=1,2 are given by

$$\begin{aligned} \beta_1 &= \beta + \delta F_1 (U_1 - U_2) \\ \beta_2 &= \beta + \delta F_2 (2U_2 - U_1). \end{aligned} \tag{20}$$

Thus, in the context of the two-and-a-half layer model, the Charney-Stern theorem implies the following instability condition:

$$\beta_1 \beta_2 < 0 . \tag{21}$$

Since the direction variable $\delta = \pm 1$ explicitly enters (20), the specific instability conditions for westward and eastward flows are considerably different. These conditions are expressed in terms of β, U_1, U_2, F_1 and F_2 in Table 1.

Table 1. Conditions for baroclinic instability (Charney & Stern, 1962) of westward ($\delta = -1$) and eastward ($\delta = 1$) flows in the two-and-a-half layer model expressed in terms of the basic velocities in each layer.

δ	Condition	Stable	Unstable
- 1	$U_2 < U_1 \frac{(F_1 + F_2)}{(F_1 + 2F_2)}$	$\beta \geq -\delta F_1 (U_1 - U_2)$ or $\beta \leq -\delta F_2 (2U_2 - U_1)$	$\beta < -\delta F_1 (U_1 - U_2)$, and $\beta > -\delta F_2 (2U_2 - U_1)$
- 1	$U_2 > U_1 \frac{(F_1 + F_2)}{(F_1 + 2F_2)}$	$\beta \leq -\delta F_1 (U_1 - U_2)$ or $\beta \geq -\delta F_2 (2U_2 - U_1)$	$\beta > -\delta F_1 (U_1 - U_2)$ and $\beta < -\delta F_2 (2U_2 - U_1)$
1	$0 < U_2 < \frac{U_1}{2}$	$\beta \geq -\delta F_2 (2U_2 - U_1)$	$\beta < -\delta F_2 (2U_2 - U_1)$
1	$U_1 > U_2 > \frac{U_1}{2}$	always	never
1	$U_2 > U_1$	$\beta \geq -\delta F_1 (U_1 - U_2)$	$\beta < -\delta F_1 (U_1 - U_2)$

D. COHERENT VORTICES IN STABLE WESTWARD SHEAR FLOWS

Because of dissimilarities in the evolution of vortices in westward and eastward shears, these configurations are considered separately. This section will focus on baroclinically stable westward flows ($\delta = -1$), while their eastward counterparts ($\delta = 1$) will be discussed in Sec. 5. The analysis is based on a series of numerical simulations performed using the pseudospectral dealiased algorithm (e.g., Radko and Kamenkovich 2017) which assumes doubly periodic boundary conditions for ψ_i and performs temporal integrations using a fourth-order Runge-Kutta scheme.

To introduce an isolated coherent vortex in simulations, we assume a Gaussian structure for its potential vorticity:

$$\overline{q}_i = A_i \exp(-ar^2), \tag{22}$$

where A_i is the maximal vortex PV value in each active layer (i=1,2), r is the distance from its center, and a controls the lateral extent of the vortex. For the vortex itself to be baroclinically stable, the radial PV gradients should be of the same sign. In the context of the Gaussian PV model, this criterion implies that the A_i values are of the same sign as well. Given the invariance of quasi-geostrophic equations with respect to the transformation $(\psi, y) \to (-\psi, -y)$ the evolutionary patterns of anticyclonic and cyclonic vortices mirror each other. Thus, without loss of generality, we shall consider only cyclonic eddies: $A_i > 0$.

The vortex characteristics A_i and a can be readily connected to the integrated PV signatures in each layer (B_i),

$$B_i = A_i \pi / a, \tag{23}$$

which were introduced in (16) and will be used throughout this investigation as key diagnostic variables. The Gaussian model (22) serves a dual purpose of initiating numerical simulations with strong coherent vortices and as a means for monitoring the eddy strength and position by fitting it to the evolving vortex PV patterns.

Figure 1 illustrates the typical evolution of a vortex embedded in the westward flow. The non-dimensional domain size is $(L_x, L_y) = (300,150)$, which is resolved by $(N_x, N_y) = (1024,512)$ grid points. The parameters of the initially introduced vortex are $B_1 = 1600$, $B_2 = 2000$, $a = 0.1$, and the stratification is $F_1 = F_2 = 2$.

Figure 1. Snapshots of the potential vorticity for a vortex in the westward stable flow.

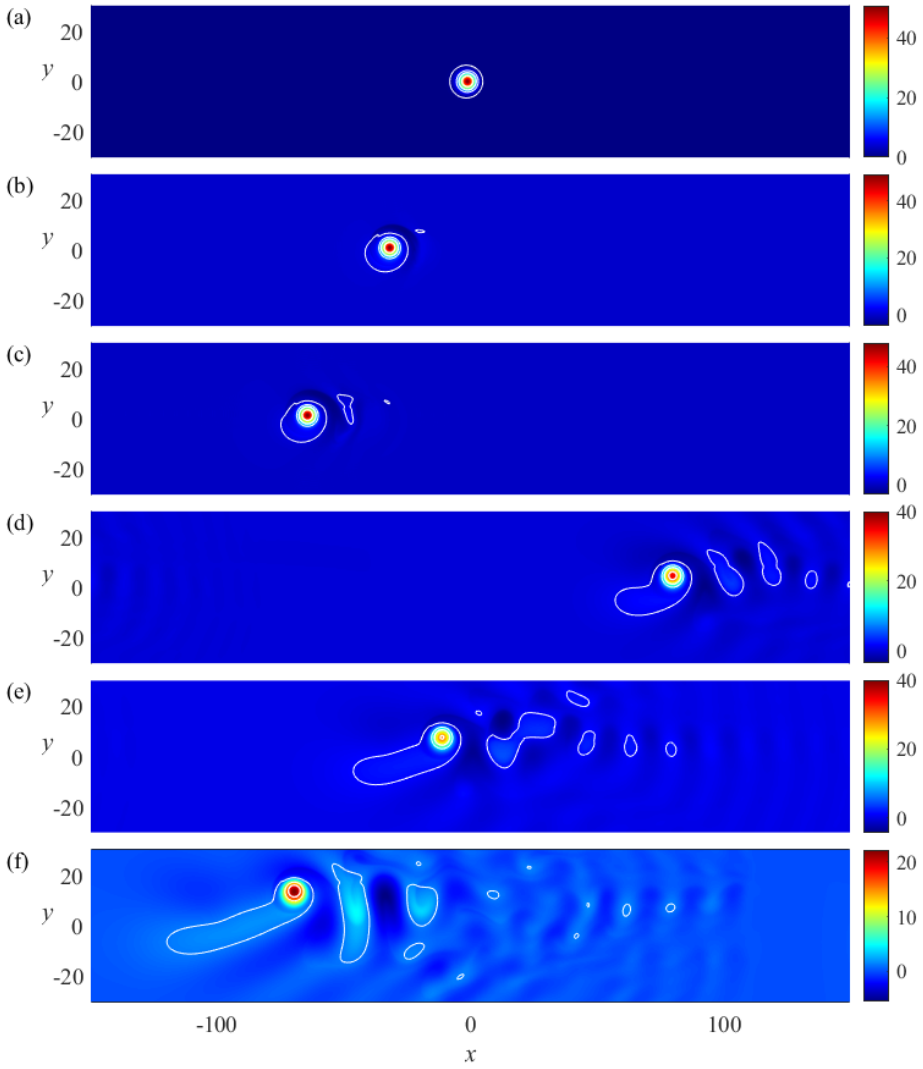

Shown at t = 1, 25, 50, 400, 700, and 1200 in (a)-(f) respectively. The color plots represent the PV patterns in upper layer (q1), and the white contours represent q2. During the experiment, the vortex makes 8.5 passes through the computational domain due to the periodicity in x. Only a central 300 x 60 area of the full 300 x 150 domain is depicted for better visualization.

To ensure that the background flow is baroclinically stable according to (21), we assume background PV gradients of the same sign: $\beta_1 = 0.25$ and $\beta_2 = 0.75$. These gradients correspond to $\beta =$ 1.08 and the second layer velocity of $U_2 = 0.585$ —the readers are reminded that $U_1 = 1$ within the chosen non-dimensionalization. For $R_d^* = 25$ km and $\left|U_1^*\right| = 10$ cm/s, the initial vortex radius is $L_{\max}^* = 62$ km, as defined by the distance between its center and the location of maximal azimuthal velocity. The maximal velocities in layers 1 and 2 are $V_{\max 1}^* = 68$ cm/s and $V_{\max 2}^* = 49$ cm/s respectively. These values represent strong coherent vortices, exemplified by the Gulf Stream rings (Olson 1991; Chelton et al. 2011). The corresponding initial Rossby numbers $(Ro_i \equiv V_{\max i}^* / f^* L_{\max}^*)$ in the first and second layers are $Ro_1 =$ 0.11 and $Ro_2 = 7.9 \times 10^{-2}$. Such relatively low values of Ro justify the quasi-geostrophic approximation (1) used throughout this study.

Notice that after initialization, the vortex in Figure 1 propagates in a predominantly westward direction with only a slight northward drift (Figure 1a-f). The experiment was extended in time for T = 2000 non-dimensional units, which is equivalent to T^* = 13.6 years. During this time, the eddy traveled the distance of ~64,000 km making 8.5 passages across the domain, with re-entry afforded by the periodic boundary conditions of the model. The color patterns representing the first layer PV and the white contours the second. Notice that the locations of the PV maxima in both layers nearly coincide, revealing that vortex signatures remain vertically aligned throughout the entire simulation. The vortex translates as a coherent entity that is remarkably resilient to the splitting tendency of the background shear.

As the vortex propagates, it inevitably generates a wake, which consists of the Rossby lee waves and more irregular time-dependent patterns as well (Nycander 2001; Kravtsov and Reznik 2019; McWilliams and Flierl 1979). Due to the periodic boundary conditions, the vortex wake eventually extends for the full domain length and makes

contact with the primary eddy like a dog chasing its tail. Following Sutyrin et al. (2021), we minimize these artificial consequences of meridional periodicity by damping PV perturbations in the region $90 \le L_{damp} \le 120$, where L_{damp} is the distance to the west of the vortex center.

Figure 1 also reveals the substantial temporal variation in the vortex intensity in both layers. In this regard, the key question is whether such variation reflects the system transition to the adjusted state (TAVS). To examine this possibility, we turn to the necessary condition (18) for TAVS and quantify the adjustment tendency using the temporal records of the vortex's net PV signatures $B_i(t)$. An interesting technical challenge is the identification of the PV patterns that are directly associated with the vortex itself. The wake generated by the vortex includes irregular time-dependent structures that extend into its far-field (e.g., Figure 1). The contribution from these distant secondary patterns to (B_1, B_2) can substantially contaminate the PV signature of the vortex, demanding their exclusion from the adjustment analysis. To that end, several algorithms have been considered, including the Okubo-Weiss criterion (Okubo 1970; Weiss 1991; Isern-Fontanet et al. 2003). Since the results proved to be largely model-independent, here we present the simplest approach based on fitting the Gaussian pattern (22) to the PV anomalies in each layer and then using (23) to evaluate (B_1, B_2). The Gaussian method allows us to simultaneously track the vortex and control the fidelity of our diagnostics. In particular, the estimates of (B_1, B_2) are considered reliable as long as the relative error $rms(q_i - q_{fit\,i}) / rms(q_i)$ of the Gaussian fit $(q_{fit\,i})$ over the vortex area $(r < a^{-0.5})$ is less than 15% in both layers. The first instant when this condition is violated $(t = \tau)$ marks the end of the simulation's "reliability interval" and the subsequent records of $B_1(t)$ and $B_2(t)$ are not considered.

A series of experiments were conducted to determine how well coherent vortices with various initial states adjust to steady zonal propagation, and the results are presented in terms of the evolutionary patterns of (B_1, B_2) in Figure 2a. In all simulations, the environmental parameters $(\beta, U_1, U_2, F_1$ and $F_2)$ were kept the same as in Figure 1 but the initial PV signatures were systematically varied. The circles represent the initial values of B_1 and B_2, the colored curves emanating from them indicate their temporal evolution, and the black dots on each curve represent intervals of $\Delta t = 125$, which is dimensionally equivalent to approximately one year. $B_1(0)$ and $B_2(0)$ in this series of experiments were chosen to ensure adequate sampling of the parameter space above and below the TAVS limit (18). To make it easier to interpret the results in Figure 2a in the context of oceanographic measurements, the corresponding dimensional maximal PV values (A_i^*), plotted on the opposing axes, are evaluated as follows:

$$A_i^* = \frac{B_i a}{\pi} \frac{\left|U_1^*\right|}{R_d^*}. \tag{24}$$

Figure 2. Vortex PV signatures in westward flow simulations.

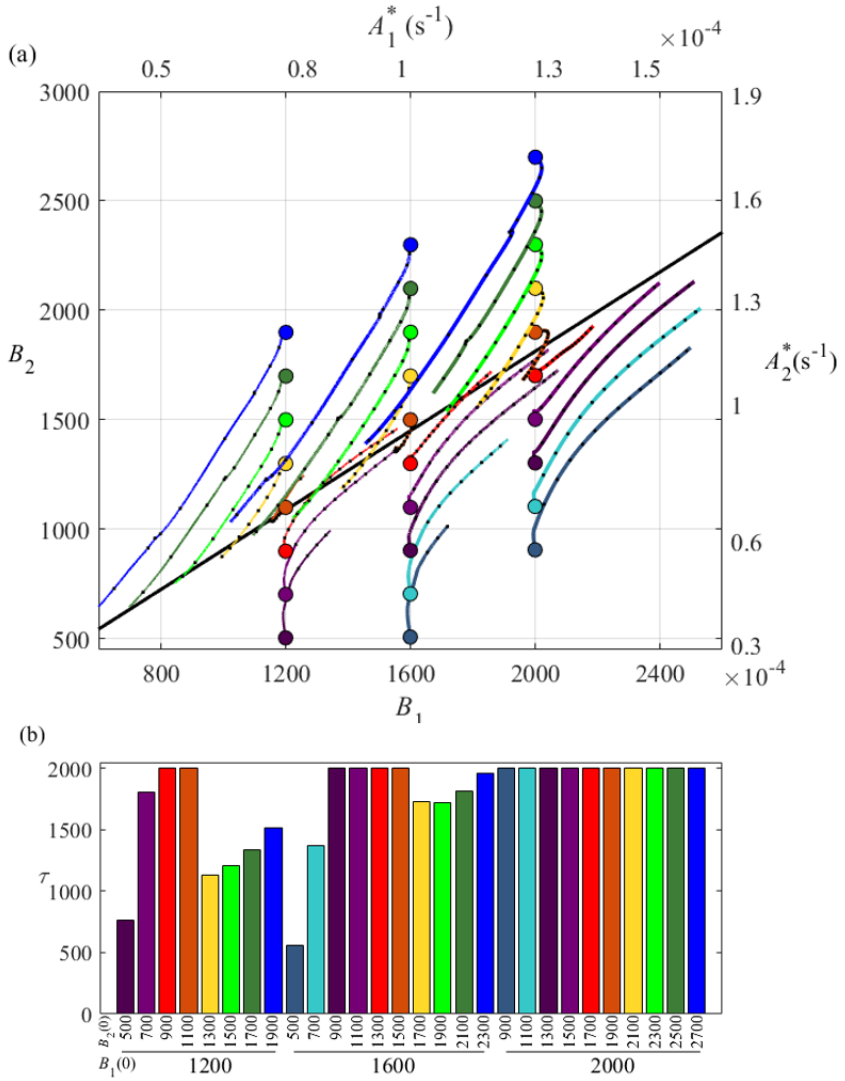

(a) The change in the vortex PV signatures $B_1(t)$ and $B_2(t)$ for stable westward flow simulations. The initial values of $B_i(0)$ are represented by the colored circles and the black dots along the curves represent increments of $\Delta t = 125$ (dimensionally equivalent to 1 yr). The solid black line represents the Translationally Adjusted Vortex State (TAVS) based on (18). The dimensional potential vorticity maxima, A_1 and A_2, are plotted on the top and right side, respectively. Note the tendency of all vortices to approach the TAVS limit. (b) The reliability intervals (τ) plotted as a function of $B_1(0)$ and $B_2(0)$.

The diagnostics in Figure 2a are highly effective in demonstrating the translational adjustment of eddies in westward flows, as the vortex strengths systematically evolve towards the TAVS limit (solid black line). Particularly interesting are the cases initiated below the TAVS limit, which offer examples of fully developed coherent vortices that spin up during the late stages of their evolution. This self-amplification tendency may be one of the contributing factors that explain the longevity of eddies in westward flows (Sutyrin and Radko 2019, 2021; Sutyrin 2020a). This result, however, should be interpreted with caution since the definition of the vortex strength may be ambiguous. For instance, the apparent intensification of the vortex PV signatures in simulations where the eddy is initiated below the TAVS limit (Figure 2a) is not accompanied by the energy gain. In these experiments, the net vortex energy levels remain roughly uniform or slightly decrease, albeit at a rate much less than that of vortices initiated above the TAVS limit. Such peculiar PV intensification that is unaccompanied by the energy growth could be the manifestation of the mechanism described by Sutyrin (2020b), who argued that the peripheral dispersion and associated reduction in the vortex radius can increase its angular momentum. Also notable is that, vortices initiated above the TAVS frequently overshoot the TAVS limit, revealing a subtle dependence of the vortex ability to adjust on the initial conditions.

Figure 2b presents the reliability intervals (τ) of all simulations as a function of $B_1(0)$ and $B_2(0)$. The vortices initiated below the TAVS limit become non-Gaussian faster than those at or above it and therefore are characterized by lower values of τ. Nevertheless, all vortices in our westward-flow simulations remain coherent throughout the entire duration of experiments (T=2000). A striking feature of vortices initiated near the TAVS limit is their ability to retain their initial PV signatures for the entire simulation. This feature is manifested in the very limited displacements of (B_1, B_2) along the TAVS line (Figure 2a).

The next set of calculations explores the change in c_1 and c_2 from the initial (typically unbalanced) state towards the final, more adjusted configuration. Figure 3a presents a series of experiments performed with various $B_2(0)$ with a constant $B_1(0) =$

1600; in Figure 3b, $B_1(0)$ is varied but $B_2(0) = 1600$ is kept constant. All other model parameters are the same as in the previous simulations (Figs. 1,2).

Figure 3. Initial and final speeds for each PV signature-westward flow simulations

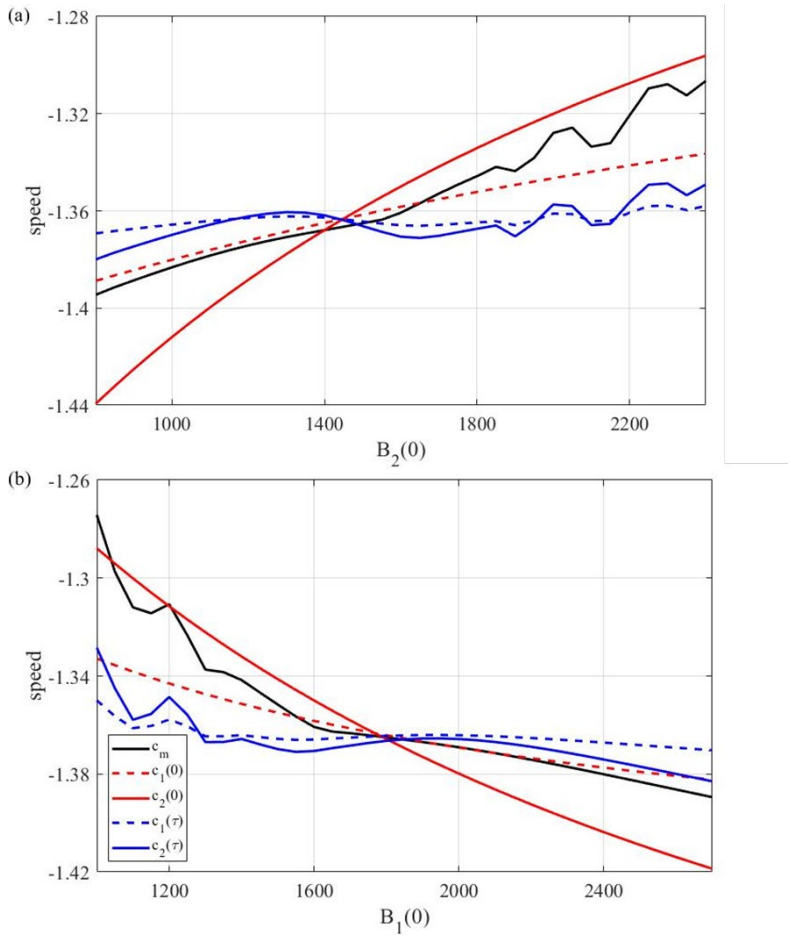

The values of c_1 (dashed curves) and c_2 (solid color curves) are plotted as functions of $B_1(0)$ and $B_2(0)$ at t=0 (red), and at $t = \tau$ (blue). The series of experiments in (a) were performed with $B_1(0) = 1600$, while $B_2(0)$ varied from 800 to 2400. In (b), $B_2(0) = 1600$ and $B_1(0)$ is varied from 1000 to 2700.

The analysis in Figure 3 addresses the conundrum posed by Equations (13) and (14) , which predict two distinct values of propagation velocity in layers 1 and 2. The simulations (e.g., Figure 1), on the other hand, reveal that eddies propagate as coherent entities, with nearly identical velocities in the first and second layers. Thus, in Figure 3, we plot the initial ($t = 0$) and final ($t = \tau$) solutions of (14) for c_1 and c_2, and the velocity diagnosed directly from the numerical model c_m. For each simulation, c_1 and c_2 were evaluated using $B_1(0), B_2(0), B_1(\tau)$, and $B_2(\tau)$. The red curves represent the initial values, and their counterparts at $t = \tau$ are shown in blue.

The crossing points of the red curves in Figure 3 correspond to the configurations where the vortices were initiated at the TAVS limit. Such vortices were in an adjusted state to begin with, while simulations to the right and left represent the evolution of non-equilibrated systems. In latter experiments, initially c_1 and c_2 differ considerably but shift towards each other at $t = \tau$. This convergence represents a salient manifestation of the translational adjustment tendency. To further quantify the extent of this adjustment, in Figure 4 we plot the relative differences between c_1 and c_2:

$$\sigma = \frac{c_1 - c_2}{c_2}, \tag{25}$$

at the beginning ($t = 0$) and the end ($t = \tau$) of each experiment. The values of σ dramatically decrease at τ in the vast majority of westward-flow simulations. The only simulations in which σ did not decrease were those initiated near the TAVS limit. These vortices remained in approximately adjusted states throughout the entire simulation, and their PV signatures were relatively steady (Figure 2a).

Figure 4. The relative difference between c_1 and c_2 (σ) plotted as a function of $B_1(0)$ and $B_2(0)$ at (a) t=0 and (b) t=τ.

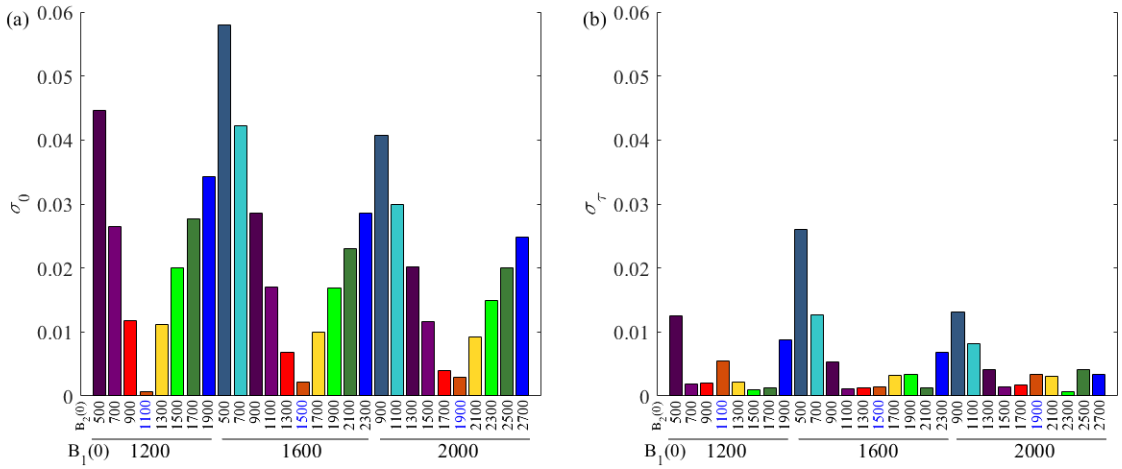

Figure 5. The temporal record of c_1 (red), c_2 (blue), and c_m (black) for two representative stable westward flow cases.

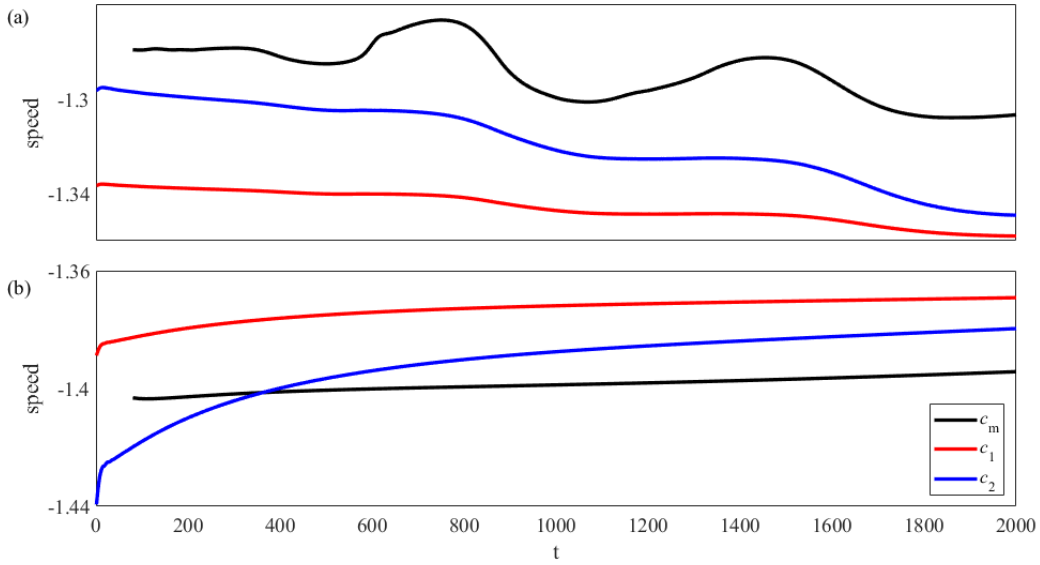

The experiment in (a) was performed with $B_1(0) = 1600$ and $B_2(0) = 2400$. For the simulations in (b), the second layer PV signature was reduced to $B_2(0) = 800$. In both cases, vortices retain their Gaussian patterns for the entire simulation period of $T = 2000$.

Figure 5 brings insight into the temporal pattern of the translational adjustment. Two representative simulations were selected from those in Figure 3 to illustrate how (c_1, c_2, c_m) change in time. Figure 5a shows a case initiated 'above' the TAVS limit with $B_1(0) = 1600$ and $B_2(0) = 2400$, whereas the corresponding 'below' simulation with $B_2(0) = 800$ is shown in Figure 5b. Both simulations are characterized by the convergence of c_1 and c_2, which reflects the eddy's long-term adjustment tendency. The convergence is not fully completed by the end of simulations, which may be attributed to the imperfections of the Gaussian model, the limited temporal extent of experiments, the influence of the trailing Rossby wave on the vortex dynamics (Early et al. 2011), or numerous other factors. A peculiar feature of the adjustment of vortices initiated above the TAVS limit in Figure 2a, is the presence of slow, multiyear oscillations in their translational speeds (Figure 5a). These oscillations indicate the presence of several mutually adverse mechanisms that affect the adjustment. Another suggestive outcome from the westward flow simulations in this section is the validation of the drift-rate model (12). In all cases, the theoretical eddy translational velocity ($c = c_2$) agrees with the speed diagnosed from simulations. At $t = \tau$, their relative difference $(c_2 - c_m)/c_m$ averaged over the entire set of experiments is merely 0.56 %, and the maximum difference is 3.8 %.

The results in Figure 5 also draw attention to the surprisingly slow timescales of the adjustment, which occurs over several years. Since the lifetime of vortices does not typically exceed 4 years (Chen and Han 2019) this finding suggests that a large fraction of ocean eddies may be in the non-adjusted or partially adjusted states. This conclusion seems particularly plausible given a wide range of the propagation speeds of coherent eddies. The observed speeds often disagree with estimates based on beta-drift theories by as much as an order of magnitude (Cornillon et al. 1989; Chassignet et al. 1990; Byrne et al. 1995; Nof et al. 2011). The most spectacular manifestation of non-adjusted dynamics is provided by

eastward propagating vortices (Chen and Han 2019) which contradict the drift theory (12) for fully adjusted vortices.

Nevertheless, the adjustment tendency discussed in this section is interesting and suggestive, particularly from a fundamental fluid dynamical perspective. Each of our simulations, only a fraction of which are presented here, indicates that the translational adjustment is a generic feature of coherent vortices embedded in westward flows. While the adjustment can be gradual and often incomplete, these dynamics still stand in stark contrast with the evolution of vortices in eastward currents, which are discussed next.

Figure 6. Snapshots of potential vorticity in the first layer (q_1) for vortex in eastward stable flow

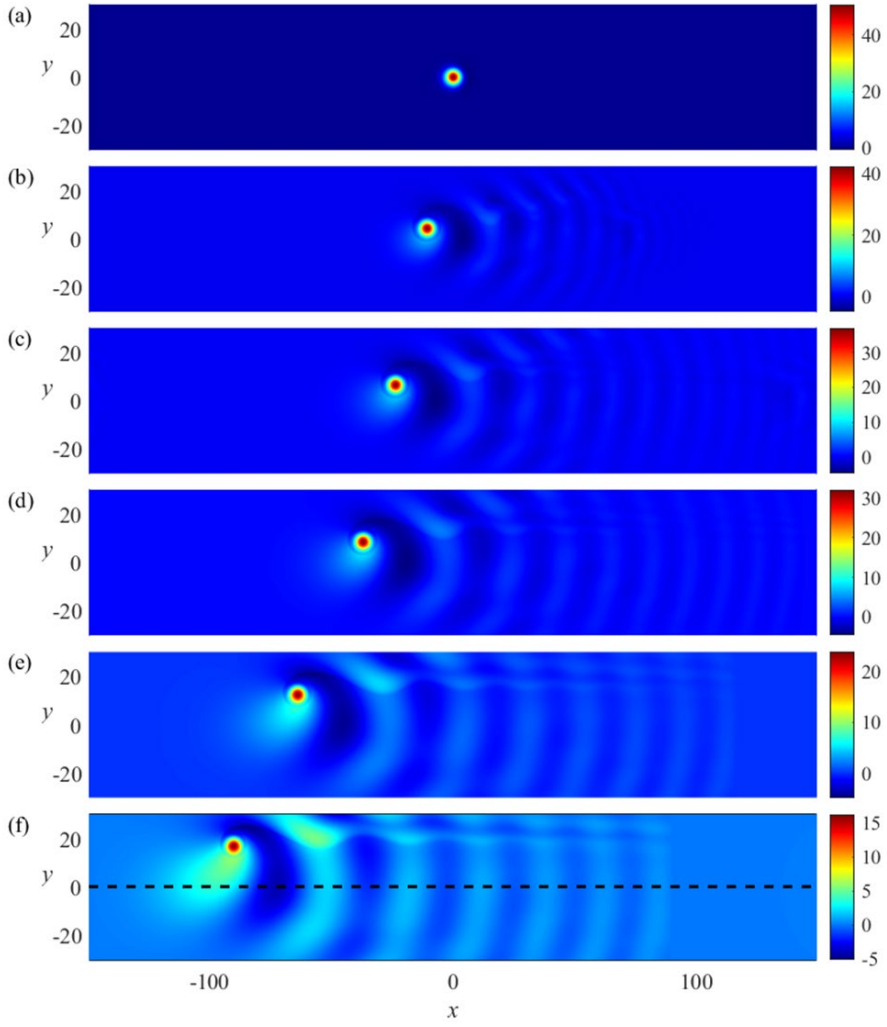

Shown at t = 1, 100, 200, 300, 500 and 700 in (a)–(f) respectively. Only a 300 x 60 area of the full 300 x 150 simulation area is depicted for better visualization. The dashed black line in (f) along y=0 is added to highlight the northward drift of the vortex.

E. COHERENT VORTICES IN STABLE EASTWARD SHEAR FLOWS

The following simulations examine the evolutionary patterns of vortices embedded in the eastward flow $(\delta = 1)$. To ensure the stability of the background current, we consider the same-sign net PV gradients of $(\beta_1, \beta_2) = (0.8, 0.8)$ which satisfy the Charney-Stern condition (21). These values correspond to U_2 =0.667 and $\beta =$ 0.133. Otherwise, the same parameters are used in eastward-flow simulations as previously in Sec. 4. The experiment in Figure 6 was performed with $B_1(0) = 1600$ and $B_2(0) =$ 2000, and therefore the initial vortex pattern is identical to that in the westward experiment in Figure 1. However, the vortex in Figure 6 is characterized by a more rapid reduction in strength, larger meridional displacement, and a stronger Rossby wake than in its westward counterpart. These features are representative of all experiments discussed in this section.

To determine whether vortices embedded in eastward flows exhibit the adjustment tendencies, we follow the analysis in Sec. 4. A set of experiments was initiated by eddies with various strengths. The resulting evolutionary patterns of (B_1, B_2) are shown in Figure 7a, along with the corresponding TAVS limit. The most dramatic difference in these diagnostics relative to their westward counterparts (Figure 2a) is the lack of pronounced translational adjustment in all simulations. The (B_1, B_2) values monotonically decrease, tracing the lines nearly parallel to the TAVS limit, but generally not approaching it. Unlike in the westward flows where PV signatures below the TAVS strengthen over time, in eastward flows there is no indication of any increase in vortex strength. Another salient feature of eastward-flow simulations is that vortices became non-Gaussian much faster, by at least a factor four than their westward counterparts. The periods of quasi-Gaussian evolution (i.e., reliability intervals τ) are shown in Figure 7b, revealing that τ did not exceed $\tau_{\max}$ = 693 in any eastward run. The substantial departure of vortices from the Gaussian pattern is followed by the loss of coherence and their eventual fragmentation.

Figure 7. Vortex PV signatures in eastward flow simulations.

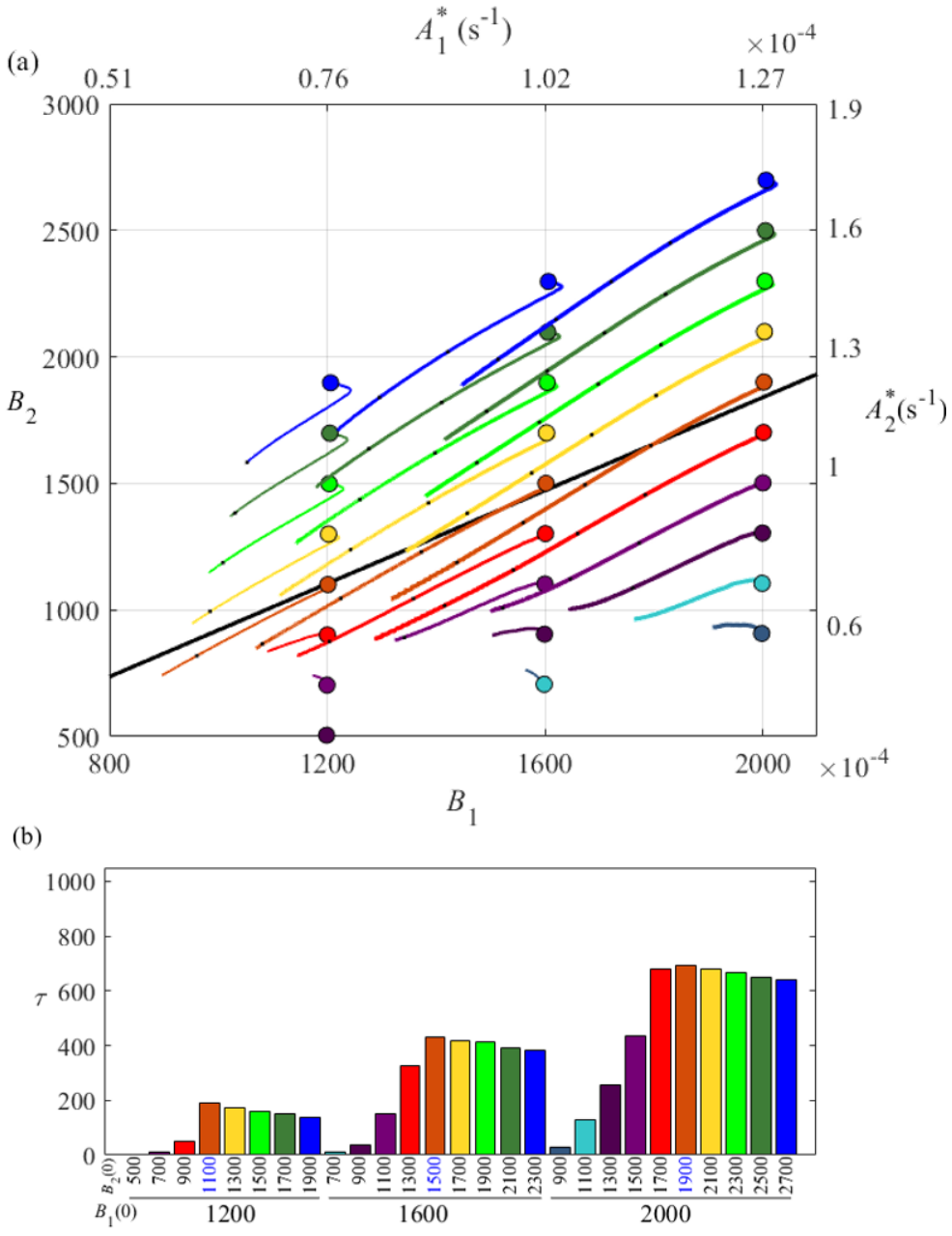

Unlike the westward-flow simulations, the present set offers no indication of the translational adjustment.

Figure 8. The reliability interval (τ) is plotted as a function of $B_1(0)$ and $B_2(0)$ for vortices in the stable eastward flow.

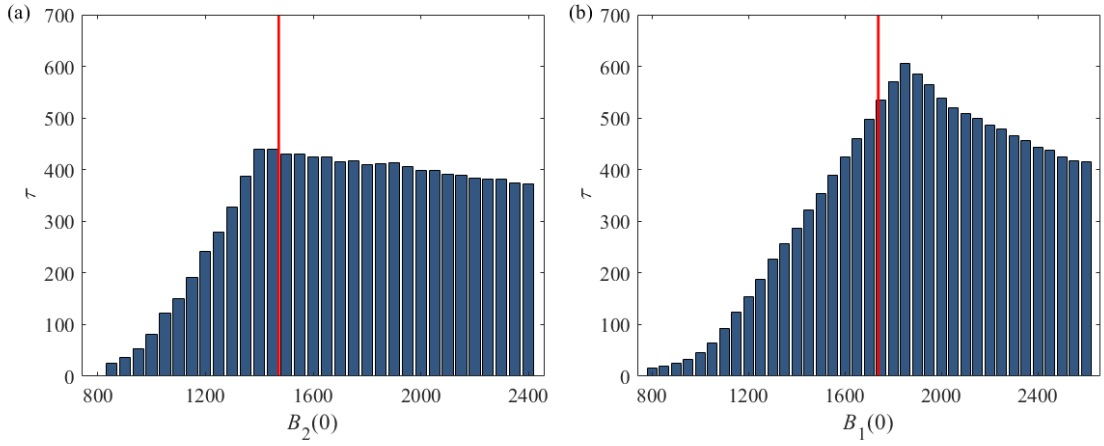

The experiments in (a) were performed with $B_1(0) = 1600$ and various values of $B_2(0)$, while $B_2(0) = 1600$ and various values of $B_1(0)$ were used in (b). The red line represents the TAVS limit.

The next set of calculations (Figure 9) analyzes the temporal variation in propagation velocities of vortices in eastward flows. The experiments in Figure 9a were performed with various $B_2(0)$ and constant $B_1(0) = 1600$; in Figure 9b, we varied $B_1(0)$ but kept $B_2(0) = 1600$. As expected, the patterns of (c_1, c_2, c_m) in Figure 9 are also different from their westward-flow counterparts (Figure 4). Most notably, c_1 and c_2 fail to converge in time for all experiments in Figure 9, which indicates the lack of adjustment. The propagation speed directly diagnosed from simulations (c_m) generally follows the pattern of c_2 (albeit with a substantial offset) and is qualitatively different from the pattern of c_1. Figure 10 presents the census of σ—the relative difference between c_1 and c_2— at the beginning (σ_0) and the end (σ_τ) of all eastward-flow simulations. These diagnostics reveal no systematic and substantial reduction of σ in time, indicating the inability of vortices in eastward flows to adjust.

Figure 9. Initial and final values of translational velocity.

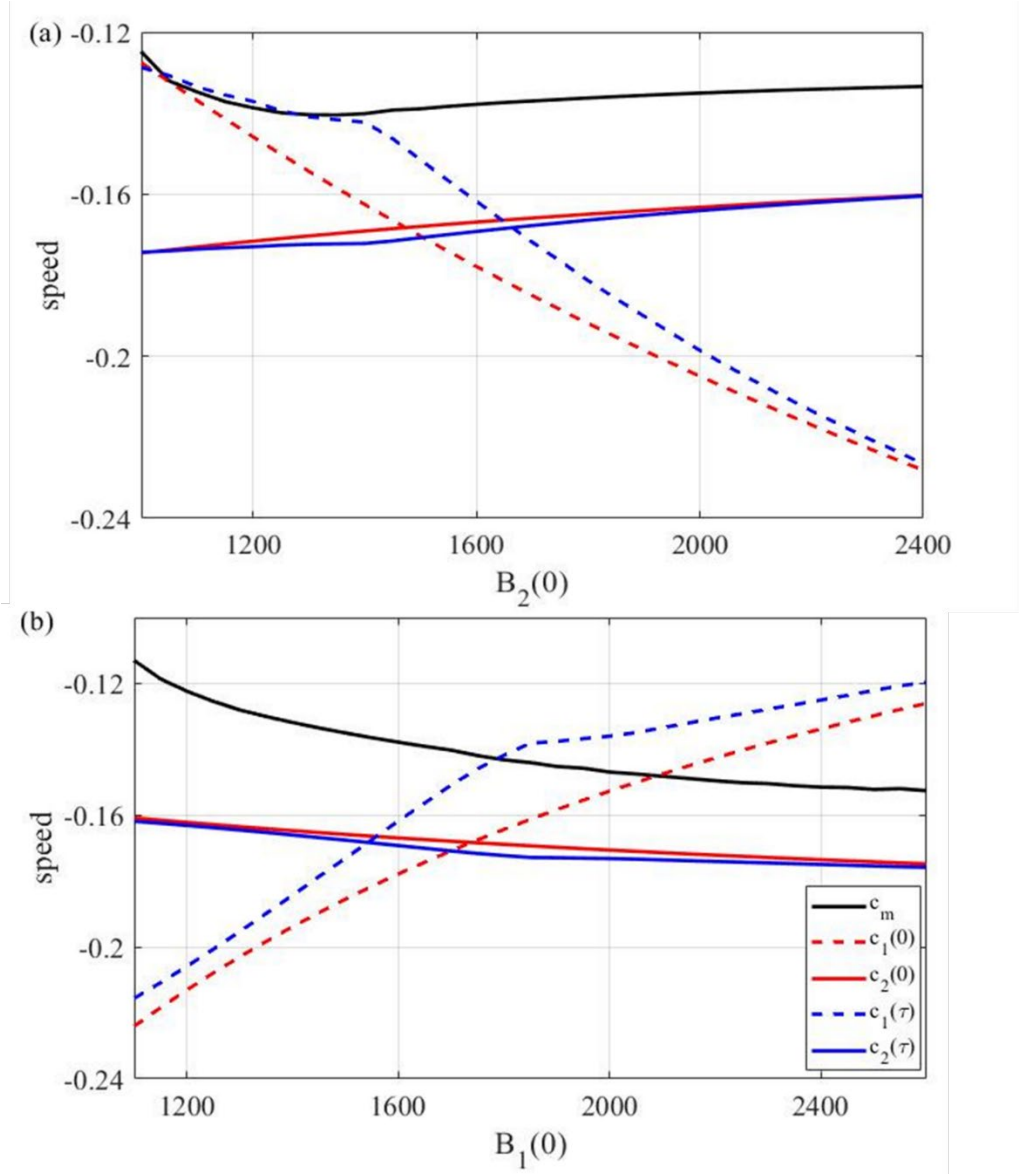

The initial (red) and final (blue) values of c_1 (dashed curves) and c_2 (solid color curves) plotted as functions of $B_1(0)$ and $B_2(0)$. The series of experiments in (a) were performed with $B_1(0) = 1600$, while $B_2(0)$ varied from 1000 to 2400. In (b), $B_2(0) = 1600$ and $B_1(0)$ is varied from 1100 to 2600

Figure 10. The same diagnostics as in Figure 4 but for the eastward flows

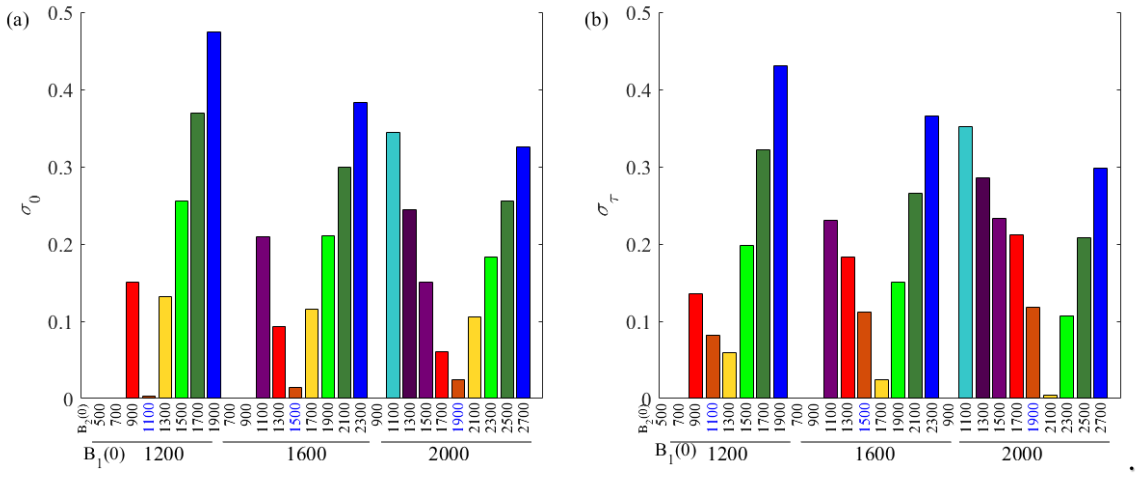

The relative difference between c_1 and c_2 (σ) is plotted as a function of $B_1(0)$ and $B_2(0)$ at (a) t=0 and (b) $t = \tau$.

In Figure 11, we focus on two representative simulations selected from the entire set in Figure 9, one above (Figure 11a) and one below (Figure 11b) the TAVS limit and examine the temporal variation of $(c_1, c_2, c_m)(c_1, c_2, c_m)$. The simulation in Figure 11a is characterized by nearly constant c_1 and c_2 through the lifespan of the eddy. The simulation in Figure 11b, initiated below the TAVS limit, even shows a divergence of c_1 and c_2. Both experiments also exhibit rather modest agreement between the theory-based (c_2) and simulated (c_m) drift rates. For the entire set of eastward flow simulations, the relative mean difference between c_2 and c_m is 22 % (maximum of 34%), which greatly exceeds the error of 0.56 % (3.8%) in the corresponding westward-flow simulations (Figure 5). This result is not surprising, since the theoretical model of propagation (Sec. 3) assumes the adjusted vortex states, and vortices in eastward flows fail to conform to this premise.

Overall, the analyses in Sections 4 and 5 highlight major differences in the dynamics and longevity of vortices embedded in westward flows and eastward flows. One

of the mechanisms causing this disparity is related to the pattern of the background PV gradients. In westward currents, the upper layer PV gradient associated with the flow

$$PVG_{flow} = \frac{\partial}{\partial y} F_1 \left(\overline{\Psi}_2 - \overline{\Psi}_1 \right) = F_1 \left(U_1 - U_2 \right) \delta \tag{26}$$

is negative (i.e., southward), and therefore it opposes the action of the planetary gradient (β>0). Thus, these two components partially cancel out, allowing the circular surface-intensified eddy to spin with minimal perturbations and meridional displacement. As a result, the vortex evolution is controlled by relatively subtle dynamics of translational adjustment. Conversely, in eastward currents where the flow PV gradient (26) and β are both positive, the effects caused by planetary vorticity are intensified. The system dynamics in this case are controlled by the vortex tendency to propagate towards the "rest latitude" of the eddy spin-down due to the conservation of the net PV (McWilliams and Flierl 1979; Rhines 1979). This tendency can be seen in Figure 6 (a-f) where the eddy is displaced northward by $\Delta L_y \approx 17$ (dimensionally equivalent to 425 km) over the course of the simulation, which is accompanied by the major (~70%) reduction of the vortex maximum PV. The translational adjustment tendency becomes secondary relative to the effects directly induced by the strong meridional PV gradient—the northward displacement and weakening of the vortex—which dramatically reduces its lifespan.

The foregoing simulations, however, were performed in baroclinically stable environments. This behooves us to determine whether active mesoscale variability, ubiquitous throughout the World Ocean, could also profoundly affect the evolution of coherent vortices. This problem is addressed next.

Figure 11. The temporal record of c_1, c_2, and c_m for two representative stable eastward flow cases.

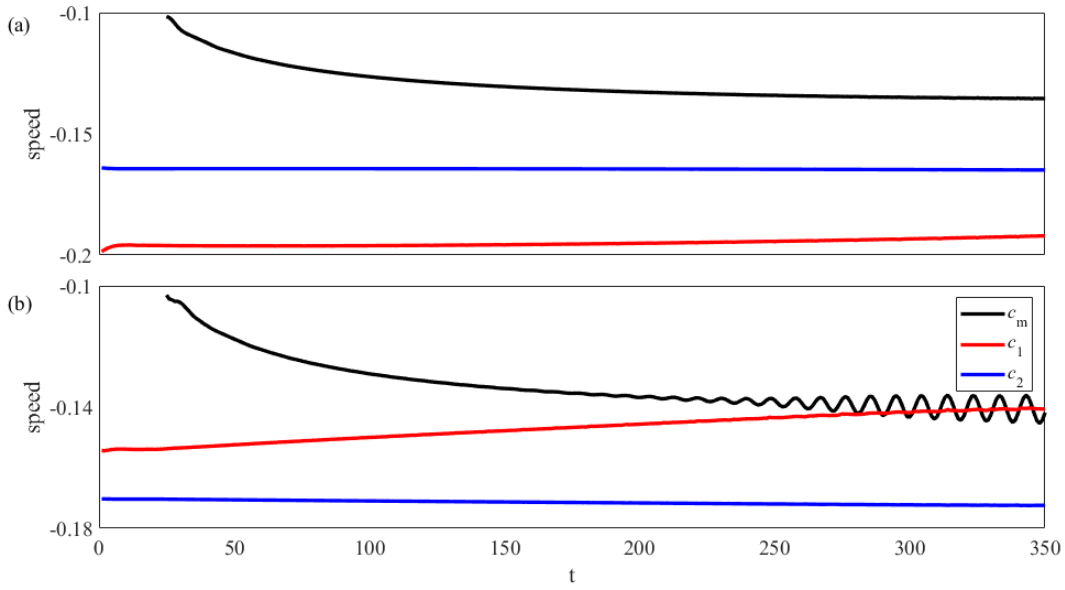

The experiment in (a) was performed with $B_1(0) = 1600$ and $B_2(0) = 1900$. For the simulation in (b), the second layer PV signature was reduced to $B_2(0) = 1300$.

F. PROPAGATION OF COHERENT VORTICES IN EDDYING FLOWS

The previous experiments modeled relatively quiescent flows where the sole source of variability was the vortex itself. Another question becomes apparent: how will a baroclinically unstable environment affect the propagation of a coherent eddy? In this regard, we first note that the discriminant (19) of the TAVS condition (18) becomes negative for the baroclinically unstable regions of the parameter space (Table 1) and therefore no combinations of (B_1, B_2) can yield a completely adjusted state. Thus, vortices in unstable shears are fundamentally incapable of approaching the TAVS limit. Based on our earlier experience (Sec. 5), one can further surmise that they would be relatively short-lived. On the other hand, we should not a priori rule out the possibility that the eddy will partially equilibrate.

To clarify these issues, we perform a series of experiments in which Gaussian vortices are introduced into baroclinically unstable eddying flows. For consistency, these experiments were conducted using the same configuration, baseline values of (B_1, B_2), domain size, and stratification (F_1, F_2) as previously (Secs.4,5). In addition, we insist that they satisfy the following requirements. First, baroclinic instability must be in a fully developed quasi-equilibrated state when the Gaussian vortex is introduced into the flow field. This requirement prevents the ambiguity of attributing the temporal variation of the system to either developing background flow instabilities or to the evolution of the coherent vortex itself. The state of equilibrium is determined by the inspection of the net eddy kinetic energy in each layer (E_i, $i = 1, 2$). When $E_i(t)$ were no longer rapidly increasing but, rather, remained at the same level and mildly fluctuating about statistically steady values, the system was viewed as quasi-equilibrated. Second, we insist that the level of background turbulence is representative of typical oceanic conditions. Third, we demand that the strength of a coherent vortex introduced and traced in simulations substantially exceeds that of irregular mesoscale variability generated by the baroclinic instability of the

background current. This requirement is critical for diagnostics since the subject eddy must be distinguishable from the background flow.

Figure 12. Snapshots of the upper layer potential vorticity (q_1) for a vortex in westward eddying flow.

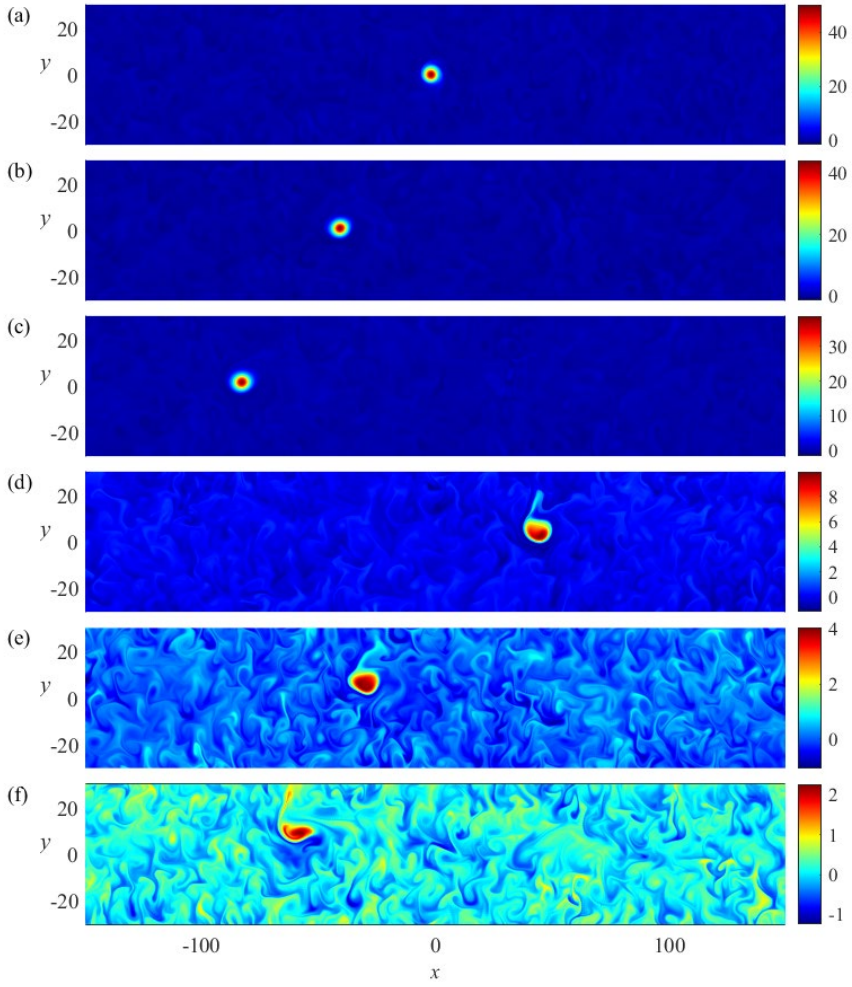

Images at t = 1, 25, 50, 350, 600, and 825 are shown in (a)–(f), respectively. By the end of the simulation the vortex has passed through the computational domain four times due to the periodic boundary conditions. Only a central 300 x 60 area of the full 300 x 150 simulation domain is depicted for better visualization.

Figure 13. The initial and final values of c_1 and c_2.

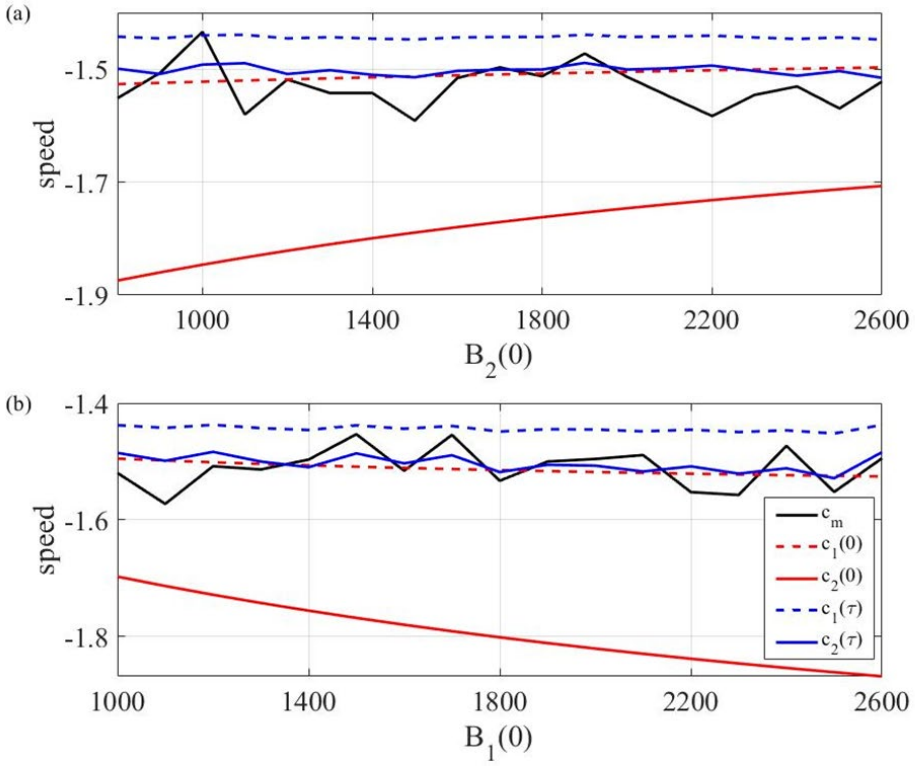

The series of experiments plotted as functions of $B_1(0)$ and $B_2(0)$ were performed with (a) $B_1(0) = 1600$ and $B_2(0)$ varied from 800 to 2600. In (b), $B_2(0) = 1600$ and $B_1(0)$ is varied from 1000 to 2600.

To ensure that background flows are unstable, the selection of governing parameters was based on the Charney-Stern condition (21). In particular, for westward flows we used $\beta_1 < 0, \beta_2 > 0$, while $\beta_1 > 0, \beta_2 < 0$ was employed for eastward currents. Small-amplitude random perturbations were introduced initially to seed the baroclinic instability. The specific values of β and U_2 were selected by insisting that the mean equilibrium eddy kinetic energy in the upper layer is consistent with representative satellite-based estimates (e.g., Stammer and Wunsch, 1999). When the system reached a quasi-equilibrated state of baroclinic instability, the Gaussian vortex (22) was added to the flow field.

Based on these criteria, the westward eddying flow experiment was set up with $\beta_1 = -0.05$ and $\beta_2 = 2.45$, which corresponds to $\beta = 1.45$ and $U_2 = 0.25$. The first stage of the experiment, devoted to the development and equilibration of baroclinic instability, was extended for $t = 1000$ units. At this point, a Gaussian vortex with $B_1 = 1600$ and $B_2 = 2000$ was introduced and its subsequent evolution is depicted in Figure 12. Figs. 12b-e reveal that the vortex moves in a predominantly westward direction. However, the vortex spins down and loses its Gaussian shape much faster than its counterpart in the stable current (Figure 1). Nevertheless, it persisted in an identifiable form throughout the entire simulation period, during which it translated zonally over the distance of $L = 1350$ from the origin.

Figure 13 is the counterpart of Figure 4 for the eddying background experiments. It presents plots of (c_1, c_2) at the instants when the vortex was introduced into the system ($t = 0$) and (c_1, c_2, c_m) at the end of the experiments ($t = \tau$). The simulations in (a) were performed with $B_1(0) = 1600$ while varying $B_2(0)$. For (b), we used constant $B_2(0) = 1600$ and varied $B_1(0)$. Because the background instability can cause a substantial fluctuation of the rms error of the Gaussian fit, the definition of the reliability interval (τ) was relaxed. In all eddying experiments, we used the maximal relative error of 0.3 for the Gaussian fit as a criterion for τ. Figure 13 illustrates the apparent tendency for partial translational adjustment. Although the measured speed is prone to variations, which could be attributed

to the instability, the values of c_1 and c_2 at $t = \tau$ are much closer than their initial values. This result is particularly intriguing in view of the lack of exact solutions of the adjustment condition (18) in the chosen parameter regime. Even though TAVS does not exist, the system still evolves in a manner that minimizes translational disbalance. The theoretical drift rate (c_2) and the vortex speed diagnosed from simulations (c_m) also converge substantially in time.

Figure 14 presents the temporal patterns of (c_1, c_2, c_m) in two representative simulations selected from the set in Figure 13, with $(B_1, B_2) =$ (1600, 2000) in (a) and $(B_1, B_2) =$ (1600, 1000) in (b). The patterns in (a) and (b) are structurally similar, revealing the systematic convergence of c_1 and c_2 in time. In addition, Figure 14 shows that $c_2 \approx c_m$ throughout the simulation, with the differences in their mean values of 0.87% and 1.18 % in (a) and (b) respectively. Both theoretical (c_2) and (c_m) velocity patterns directly diagnosed from simulations exhibit substantial temporal oscillations, likely caused by the interaction of the vortex with ambient mesoscale variability. The oscillations in c_2 are notably weaker than in c_m.

Our final examples show the vortex evolution in eastward eddying flows (Figure 15). The background instability was established as before with $\beta = 0.130$ and $U_2 = 0.454$. These parameters correspond to $\beta_1 = 1.22$ and $\beta_2 = -0.05$, satisfying the Charney-Stern condition for instability (21). Due to the rapid deterioration of the vortices in this doubly-adverse (unstable and eastward) environment, simulations were conducted with stronger vortices, which afforded longer observation periods. The simulations with $(B_1, B_2) =$ (2500, 2500) and $(B_1, B_2) =$ (2500, 1500) are presented in (a) and (b) respectively. These simulations reached the end of the reliability interval at $\tau = 115$ and $\tau = 105$; nearly five times faster than their westward counterparts despite the increase in initial strength. The relative differences between theoretical (c_2) and modeled (c_m) mean translational velocities were 29.2% and 36.5% in (a) and (b), respectively. By the end of the simulations ($t = \tau$), the differences between c_2 and c_m reduced slightly to 17.9% (a) and 21.2% (b).

As in the corresponding stable eastward flow experiments (Figure 11), the vortices in Figure 15 exhibited no signs of translational adjustment.

Figure 14. The temporal records of c_1, c_2 and c_m for two representative unstable westward flow cases.

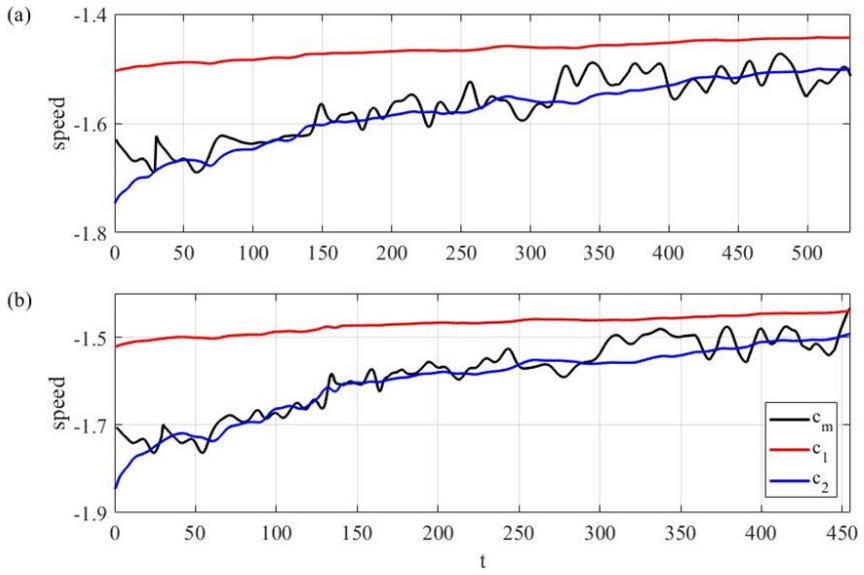

Figure 15. The temporal record of c_1 (red), c_2 (blue), and c_m (black) for two representative unstable eastward flow cases

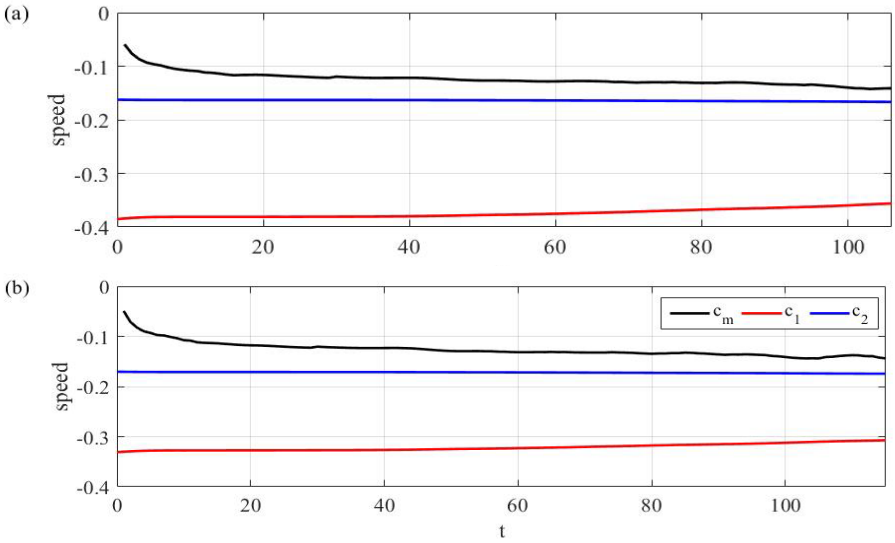

G. SUMMARY OF CHAPTER II

This study explores the dynamics and propagation tendencies of strong isolated vortices using a combination of a theoretical model and numerical simulations. The analytical framework is based on the centroid theorem (McWilliams and Flierl 1979), generalized here to multi-layer quasi-geostrophic shear flows. The investigation is framed in terms of a comparative analysis of the vortex evolution in predominantly westward and eastward flows, which could be either baroclinically stable or unstable.

The presented analysis is motivated by two key questions: Can strong coherent vortices embedded in large-scale flows evolve to a state of uniform zonal propagation, and what are the ramification of such transformation for vortex longevity? The answer to these questions proved to be regime-dependent. The generalized centroid theorem (Sec. 3) permits the emergence of Translationally Adjusted Vortex States (TAVS) for baroclinically stable background currents and precludes them for unstable flows. However, numerical experiments have shown that the situation is even more complex.

A series of simulations performed using a two-and-a-half layer spectral model revealed that, even in stable flows, the initially unbalanced vortices may or may not evolve towards the TAVS limit. Vortices embedded in westward flows (Sec. 4) generally exhibit an adjustment tendency, albeit the process could be slow and incomplete. In contrast, eddies in eastward flows (Sec. 4) do not adjust to steady zonal propagation. Their propagation speeds contain a significant meridional component, which leads to their spin-down and eventual disintegration. Vortices in westward flows often survive as coherent entities over decadal time scales, whereas the lifetime of their eastward-flow counterparts is typically less by almost an order of magnitude. Somewhat counterintuitively, the longevity of vortices in eastward flows is still controlled by the proximity of their initial configurations to the TAVS limit (Figure 8).

The fundamental differences in the dynamics of coherent vortices in westward and eastward flows are attributed to the dissimilar background PV patterns. In westward currents, the flow component of the upper layer meridional PV gradient is negative, thereby opposing the positive gradient of the planetary component (β). The partial cancellation of

these two PV components creates favorable conditions for surface-intensified coherent vortices to persist for long periods, maintaining a predominantly zonal motion pattern with very limited meridional displacement. In eastward flows, the planetary and flow PV gradients in the upper layer mutually reinforce each other, which leads to relatively rapid meridional drift of the vortex towards the rest latitude, its systematic weakening, and eventual fragmentation. The remarkable longevity of vortices in the westward subtropical corridors is borne out in satellite-based measurements (Chelton et al. 2007, 2011; Sangrà et al. 2009; Fu et al. 2010; Dilmahamod et al. 2018; Chen and Han 2019) and our study brings much-needed insight into the physical mechanisms at play.

Coherent vortices in baroclinically unstable eddying flows also exhibit direction-dependent dynamics. While the generalized centroid theorem (Sec. 3) formally precludes the emergence of fully adjusted vortical configurations, vortices in westward flows still tend to adjust partially to steady zonal propagation. In eastward currents, such a tendency is notably absent—a feature which likely accounts for the fragility and shorter lifespans of vortices harbored by such flows. Overall, however, vortices in baroclinically unstable shears, both westward and eastward, tend to be less robust than their counterparts in stable currents. This could be attributed to a combination of several factors, which include the lack of TAVS states and the adverse dispersive effects of the irregular ambient mesoscale variability.

Another key conclusion from this study is that the theoretical model is capable of delivering adequate estimates of translational velocity ($c = c_m$). The drift-rate theory is particularly accurate in representing the speeds of mature vortices in westward flows, where its relative error averages ~0.6 %. Such predictive skill is comforting and perhaps surprising, given that the analytical model assumes balanced quasi-steady zonal propagation that is only partially realized in simulations. Another interesting feature of the analytical model (Sec. 3) is that the drift rate it predicts is independent of the background flow pattern. Such an extreme manifestation of the anti-Doppler effect, previously noted for the equivalent-barotropic model (Nycander 1994), seems counter-intuitive. Furthermore, it appears to be at odds with oceanographic measurements, indicating that the effect of large-scale flows on isolated vortices can be substantial. Particularly suggestive

in this regard are the observations of eastward drifting eddies advected by strong eastward currents (e.g., Chen and Han 2019). The resolution of the advection conundrum lies in the possibility that a large fraction of vortices in the ocean may be non-adjusted. For such regimes, the very concept of the preferred propagation speed, commonly invoked in most drift-rate theories, may be questioned.

While this study has considerably advanced the theory of vortex-current interaction, the body of knowledge in this area is still far from complete. A logical next step would be to systematically advance the complexity and realism of the considered configurations. For instance, the transition to a more general shallow-water framework would remove the restrictions imposed by quasi-geostrophic approximation on the intensity of flow patterns, making it possible to analyze phenomena with finite Rossby numbers, such as salt lenses or Meddies. A viable objective in this regard is the identification of the integral adjustment conditions for systems with order-one variation in layer thickness. Subsequently, both the theory and modeling effort should be extended to continuously stratified systems. There is much to be learned by examining the vortex drift-rates and adjustment tendencies in the presence of topographic features. This line of research should address the dynamically dissimilar effects of both large-scale variability (Dewar 1998; Zhao et al. 2019) and small-scale bottom roughness (Gulliver and Radko 2022). The theoretical description of the temporal patterns of vortex adjustment is also of great interest. Such an endeavor would require the development of an analytical framework representing the leakage of the vortex thickness anomaly into the far-field—an interesting challenge in its own right. The largely unexplored dynamics of vortices in non-zonal background flows (e.g., Brown et al. 2019), motivate the corresponding generalization of the vortex propagation and adjustment theory. These extensions should incorporate strong horizontal shears often found in western boundary currents. Lastly, we strongly encourage the attempts to diagnose the key properties of coherent long-lived vortices in comprehensive global oceanic re-analysis models (Trott et al. 2019; Petersen et al. 2013; Thoppil et al. 2011) such as the Community Earth System Model (CESM) or Hybrid Coordinate Ocean Model (HYCOM). Of particular interest in this regard is to determine to what extent the principle of translational adjustment is reflected in more realistic scenarios.

The answer to this question could lead to advancements in representing long-lived coherent vortices in global climate models.

THIS PAGE INTENTIONALLY LEFT BLANK

III. TOPOGRAPHIC STABILIZATION OF OCEAN RINGS

This chapter was originally published in *Geophysical Research Letters* with co-author Dr. Timour Radko (Gulliver and Radko 2022b).

A. INTRODUCTION

Coherent vortices are among the most intriguing but still poorly understood features of the World Ocean. Many are formed by instabilities of intense, large-scale flows, which lead to meanders that break away forming a ring of current (Robinson 2012). Others spontaneously emerge from irregular patterns of active mesoscale variability, are generated by topographic features, or through the interactions between other vortices (Jia et al. 2011). There is general consensus regarding their importance in controlling the distribution of heat, salt, nutrients, pollutants, and other tracers on planetary scales (Kamenkovich et al. 1986; Robinson 2012; Vallis 2019). Rings in the North Atlantic, for instance, represent only 10–15 % of the ocean surface but are largely responsible for the transport of life-sustaining zooplankton and nutrients to the Sargasso Sea (Ring Group 1981). A particularly challenging and long-standing dynamical problem in the theory of coherent vortices concerns their longevity and stability. Large-scale vortices with radii of 50–150 km in the ocean are known to last for months and even years (Fu et al., 2010; Chelton et al., 2011; Chen & Han, 2019). However, stability analyses and numerical experiments performed with seemingly realistic vortex patterns (Dewar & Killworth, 1995; Killworth et al., 1997; Benilov & Flanagan, 2008; Mahdinia et al., 2017; Sokolovskiy & Verron, 2014; Yim et al., 2016) reveal their strong baroclinic instability and the tendency to disintegrate on the time-scale of several weeks. For a comprehensive discussion of the dynamics and properties of baroclinic instability, the readers are referred to the monographs by Vallis (2017) and Smyth & Carpenter (2019).

There have been several attempts to address the stability conundrum. Stable solutions can be constructed using the sign-definite potential vorticity (PV) gradient

criterion for vortex stability (Dritschel 1988). Specific examples of such solutions include the models of Meddies—North Atlantic salt lenses containing water masses of Mediterranean origin (Sutyrin & Radko, 2016; Radko & Sisti, 2017). The numerical simulations performed by Sutyrin & Radko (2016) and Radko & Sisti (2017) confirmed that the sign-definite PV gradient models produce stable and robust vortices, maintaining their initial structure for several years or more. However, the technique used in these studies suffers from a significant limitation. It can be applied only to relatively small-scale vortices with radii comparable to, or less than, the first radius of deformation. Attempts to derive analogous solutions for larger vortices result in nearly barotropic structures. In this sense, the sign-definite models are unrepresentative of most observed baroclinic, surface-intensified ocean rings with radii in the range of 50–150 km, substantially exceeding the radius of deformation (Olson, 1991; Chelton et al., 2011).

To develop fully baroclinic solutions for large-scale vortices, Benilov (2018) proposed an asymptotic model in which the strongly stratified active surface layer was placed above a deep, nearly motionless, and more homogeneous abyssal layer. This configuration allowed for vortices with radii exceeding the radius of deformation to remain stable and thereby helped to resolve the stability conundrum. The question that arises regarding such models is whether the asymptotic limit of the deep abyssal layer adequately represents typical oceanic conditions. Numerical simulations presented here using surface-intensified vortices in the flat-bottom ocean model with the realistic mean ocean depth and stratification pattern indicate that large vortices can still be unstable and rapidly disintegrate. This finding implies the presence of some other stabilizing mechanisms controlling the evolution of ocean rings.

This paper explores the possibility that the stability and dynamics of large-scale rings could be affected by the non-uniform bottom topography. The significance of flow-topography interactions for large-scale ocean processes is widely recognized (Holloway 1992; Alvarez et al. 1994). O'Kane & Frederiksen (2004), for instance, showed that even in barotropic flows small-scale topography acts to localize energy and enstrophy transfers, which impacts the lifetimes of larger scale coherent structures. In fact, some of the longest-lived coherent structures are situated over prominent topographic features (Dewar 1998;

de Miranda et al. 1999), which can be attributed to the mechanisms originally advocated by Bretherton & Haidvogel (1976) and Verron & Le Provost (1985). Topographic influences on baroclinic instability have been explored by Hart (1975), Benilov (2005), Rabinovich et al. (2018), and Brown et al. (2019). Promising attempts have also been made to parameterize the effects of topography using statistical circulation models (Alvarez et al. 1994; Polyakov 2001; Chavanis and Sommeria 2002; Merryfield and Holloway 2002; Okane and Frederiksen 2004; Frederiksen and O'Kane 2005). However, most studies consider relatively large topographic scales (Chen & Kamenkovich, 2013; Radko & Kamenkovich, 2017) or isolated topographic features (Verron and Le Provost 1985; Benilov 2005; Zavala Sansón 2019).

In contrast, our analysis is focused on irregular bathymetric patterns with dominant scales that are less than the size of the phenomena of interest, a configuration hereafter referred to as the "sandpaper" model. We assume and subsequently verify that eddy stresses generated by the rough bottom topography adversely affect the circulation in the abyssal zone. This effect draws associations with the sandpaper glued face-up to a smooth surface, like non-skid on the deck of a vessel, preventing the slippage of large objects in stormy conditions. Baroclinic instability, on the other hand, is principally driven by the interaction of flow patterns located at different levels (e.g., Phillips, 1951). Thus, it is likely that the sandpaper effect can suppress the baroclinic instability of large-scale vortices, ultimately extending their lifespan. In this regard, it should be noted that vortices in the reduced gravity models, where the abyssal layer is a priori assumed to be quiescent, tend to be relatively stable and persistent (Radko and Stern 1999, 2000; Radko 2021). The tendency of sub-mesoscale bottom roughness to stabilize large- and mesoscale parallel flows has already been demonstrated (LaCasce et al. 2019; Radko 2020b). The present investigation provides evidence that this effect is also at work in ocean rings and could account for their remarkable longevity.

This study is organized as follows. In Sec. 2 we present the model configuration and governing multilayer quasi-geostrophic equations. Topography is represented by the observationally-derived spectrum of Goff & Jordan (1988). Section 3 describes the numerical experiments and linear stability analyses conducted using the minimal two-layer

model. To ensure that our results are not biased by the crude representation of stratification, selected simulations are reproduced using the ten-layer model (Section 4). Conclusions are drawn in Section 5.

B. FORMULATION

1. Governing Equations

In order to represent the evolution of a large-scale surface-intensified vortex, we consider a quasi-geostrophic *n*-layer, rigid lid model (Charney, 1948; Pedlosky, 1983).

$$\begin{cases} \dfrac{\partial q_i}{\partial t} + J(\psi_i, q_i) = \nu \nabla^4 \psi_i, \quad i = 1,...,(n-1) \\ \dfrac{\partial q_n}{\partial t} + J(\psi_n, q_n) + \dfrac{f}{H_n} J(\psi_n, \eta) = \nu \nabla^4 \psi_n, \end{cases} \tag{27}$$

where ψ_i is the streamfunction in layer *I*, which determines the lateral velocity $(u_i, v_i) = \left(-\dfrac{\partial \psi_i}{\partial y}, \dfrac{\partial \psi_i}{\partial x} \right)$, H_i is the layer thickness, and *n* represents the bottom layer. Here, η is the variation in the bottom depth, ν is the viscosity, and *J* is the Jacobian: $J(a,b) \equiv \dfrac{\partial a}{\partial x}\dfrac{\partial b}{\partial y} - \dfrac{\partial a}{\partial y}\dfrac{\partial b}{\partial x}$.

The Coriolis parameter *f* in (27) is assumed to be constant, which makes it possible to unambiguously analyze the stability characteristics of circularly symmetric vortices. The potential vorticity (q_i) is expressed in terms of streamfunction as follows:

$$\begin{cases} q_1 = \nabla^2 \psi_1 + \dfrac{f^2}{g' H_1} (\psi_2 - \psi_1) \\ q_i = \nabla^2 \psi_i + \dfrac{f^2}{g' H_i} (\psi_{i-1} + \psi_{i+1} - 2\psi_i) \qquad i = 2,...,(n-1) \\ q_n = \nabla^2 \psi_n + \dfrac{f^2}{g' H_n} (\psi_{n-1} - \psi_n) \ , \end{cases} \tag{28}$$

where $g' = g\Delta\rho / \rho_0$ is the local reduced gravity. The formulation is simplified by assuming identical density differences between adjacent layers $(\Delta\rho = \rho_i - \rho_{i-1})$. In the following simulations, we use the mid-latitude Coriolis parameter of $f = 10^{-4}$ s^{-1} and the minimal value of viscosity needed to maintain the numerical stability of simulations $\nu = 30$ m^{2}s^{-1}. The net reduced gravity of $g'_{tot} = (n-1)g' = 0.01$ m s^{-2} is based on the density variation over the entire water column with a representative ocean depth of $H = \sum_{i=1}^{n} H_i = 4000$ m.

2. Bottom Roughness Model

To determine the effects of bottom roughness on the stability of coherent vortices, it is imperative to introduce a realistic model of the ocean depth variability. Our work is based on the empirical spectrum of topography derived by Goff & Jordan (1988) using the ocean depth sampling provided by actual echo-sounding systems:

$$P_h = \frac{\eta_0^2(\mu-2)}{(2\pi)^3 k_0 l_0}\left(1+\left(\frac{k}{2\pi k_0}\right)^2+\left(\frac{l}{2\pi l_0}\right)^2\right)^{-\mu/2}. \qquad (29)$$

Typical values of parameters in the doubly-periodic domain (29) suggested by Nikurashin et al. (2014) and used in the present study are

$$\mu = 3.5, \quad k_0 = 1.8\times10^{-4} \text{ m}^{-1}, \quad l_0 = 1.8\times10^{-4} \text{ m}^{-1} \qquad (30)$$

where k and l are zonal and meridional wavenumbers respectively. In the following calculations, we construct bottom topography as a sum of Fourier modes with random phases and spectral amplitudes conforming to the Goff-Jordan spectrum (29). The coefficient η_0 controls the height of topographic features. It will be systematically varied to quantify the link between the seafloor roughness and the vortex stability. The representative seafloor variability in the ocean (Goff and Jordan 1988) corresponds to the RMS bathymetric height of $H_{rms} \sim 305\,m$. A recent analysis of satellite marine gravity data reveals that H_{rms} varies between 10 m and 400 m in different regions of the World Ocean (Goff 2020). These estimates will guide our exploration of the parameter space.

It should be noted that the quasi-geostrophic model is designed to represent relatively large-scale (low Rossby number) flow patterns. Therefore, we exclude from the topographic spectrum all Fourier modes with wavelengths of $L_{\min} = 10$ km or less. This restriction makes it possible to keep the effective Rossby number below 0.075 in all simulations, thereby satisfying assumptions of the quasi-geostrophic model (27). To be specific, the Rossby number is defined here as $Ro = \left|\nabla^2 \psi_1\right| / f$ and averaged over the vortex area. The typical pattern of seafloor generated in this manner is shown in Figure 16.

Figure 16. The "sandpaper" model configuration.

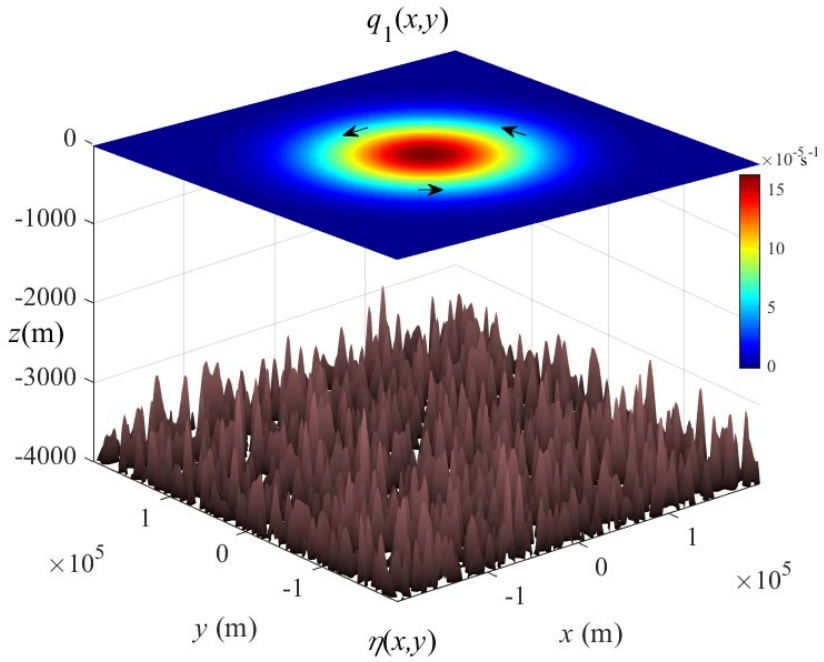

The upper plane shows the pattern of the sub-surface potential vorticity in the cyclonic vortex, with high values shown in red and low values in blue. The vortex is located above the irregular seafloor (brown surface) with the depth variance of $H_{rms} = 305$ m . Only a fraction (400 km x 400 km in x and y) of the computational domain is shown.

C. TWO-LAYER MODEL

1. Model Configuration

To assess the effects of bottom roughness on vortex stability, a series of simulations are conducted. The governing quasi-geostrophic equations (27) and (28) are solved using the pseudospectral dealiased Fourier-based algorithm employed and described in our previous works (Radko & Kamenkovich, 2017; Sutyrin & Radko, 2021). The temporal integrations use the fourth-order Runge-Kutta scheme with the adjustable time-step based on the CFL (Courant-Fredrichs-Lewy) condition. The computational domain of lateral extent $L_x \times L_y = 1500\,\text{km} \times 1500\,\text{km}$ is resolved by $N_x \times N_y = 1024 \times 1024$ grid points.

The experiments in this section are performed with the two-layer (n=2) version of the model, with layer heights of H_1 = 1000 m and H_2 =3000 m. The upper layer represents the main mid-latitude thermocline, and the lower layer—the abyssal ocean. Thus, the baroclinic radius of deformation based on the thermocline depth in this configuration is

$$R_d \equiv \frac{\sqrt{g' H_1}}{f} \approx 31.6\ \text{km}. \tag{31}$$

The simulations are initiated by using a Gaussian streamfunction pattern for the upper layer:

$$\bar{\psi}_1 = -A \exp(-\alpha r^2), \tag{32}$$

where r is the distance from the ring center. The lower layer, on the other hand, is assumed to be initially quiescent ($\bar{\psi}_2 = 0$) where the overbar denotes the basic state. This pattern represents an isolated surface-intensified vortex. Given the invariance of quasi-geostrophic equations with respect to the transformation $(\psi, y) \to (-\psi, -y)$, we consider only cyclonic eddies $(A > 0)$, without loss of generality. The coefficients A and α control the vortex intensity and size. Here they are determined by insisting that the maximal azimuthal velocity is $V_{\max} \equiv \max_r \left(\left| \frac{\partial \bar{\psi}_1}{\partial r} \right| \right) = 1\ \text{ms}^{-1}$ and the radius of maximal velocity is $r_{\max} = 70\ \text{km}$

—values that are representative of the observed ocean rings (Olson 1991). These parameters correspond to $A = 6\times10^{-6}$ m^{2}s^{-1} and $\alpha = 9.5\times10^{-11}$ m^{-2}.

2. Nonlinear Simulations

Seventeen simulations were conducted in which the amplitude of topographic roughness was systematically increased from the flat-bottom limit (H_{rms} = 0) to the maximal RMS depth variance of H_{rms} = 400 m (Goff 2020). Each experiment was extended for two years of model time. Snapshots of the upper layer potential vorticity for three selected simulations are shown in Figure 17 at t=0, 70 days, 100 days, and 2 years. The eddy in the flat seafloor experiment (Figure 17a-d) becomes unstable in just over two months (68 days). The primary vortex loses form, breaks apart, and re-forms into much smaller eddies that irregularly transit the computational domain throughout the rest of the simulation.

In all simulations with the depth variance of $H_{rms} < 150$ m, the vortex lifespan is extremely limited, ranging from 62 to 75 days. However, as H_{rms} is elevated above 150 m, the eddy lifespan begins increasing rapidly. Figs. 2e-h present the potential vorticity patterns for the simulation with $H_{rms} = 175$ m. The primary vortex in this experiment persists for 105 days, outlasting its flat-bottom counterpart by over a month. For H_{rms} = 200 m and above, the primary vortices do not break apart for the full two years—the entire duration of simulations. A representative example of such stable systems ($H_{rms} = 305$ m) is shown in figs. 2i-l.

Figure 17. Snapshots of the upper-layer potential vorticity.

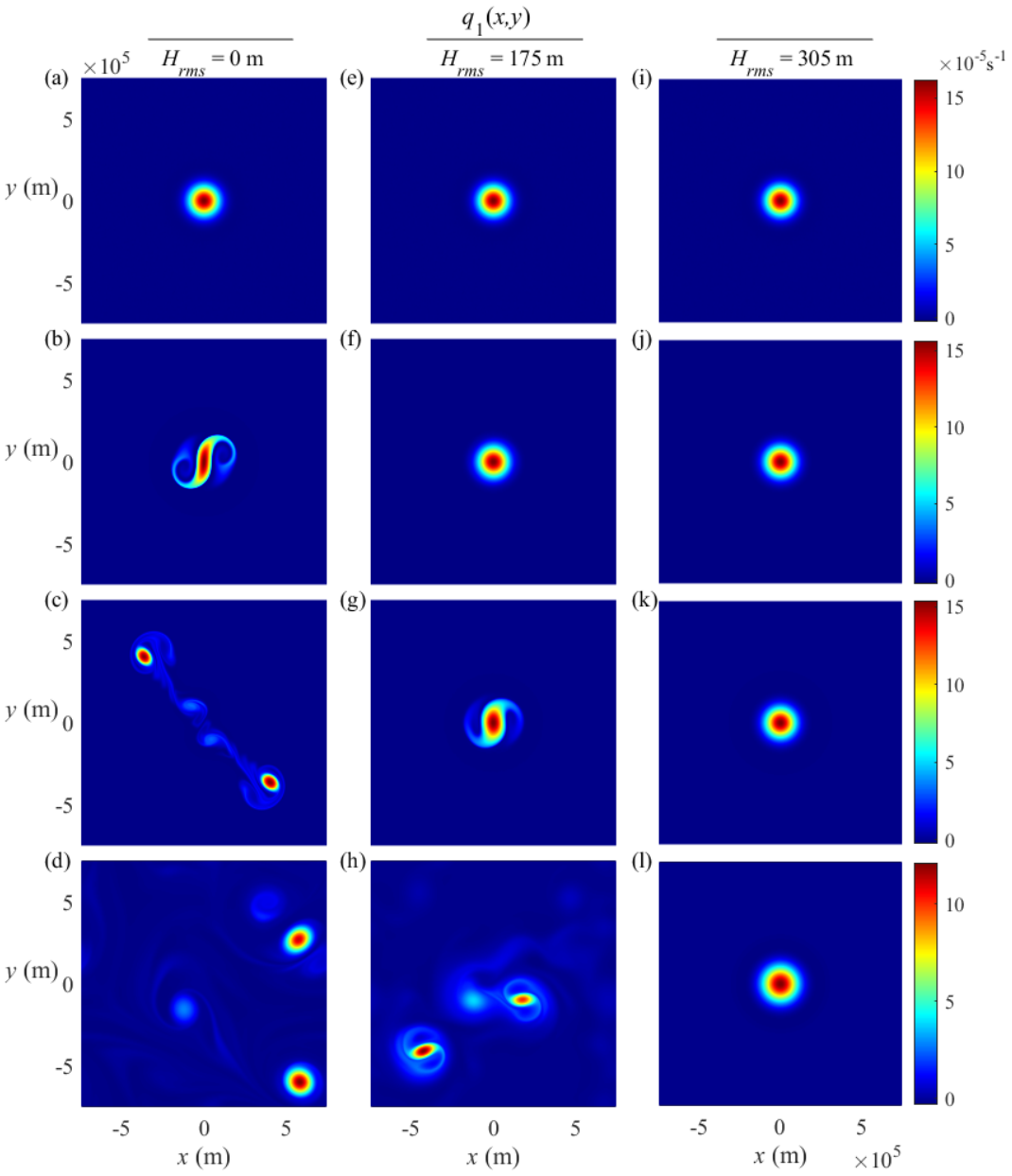

Three representative simulations at t=0 days, 70 days, 100 days, and 2 years. Panels (a-d) represent the flat-bottom simulation ($H_{rms} = 0$), (e-h) — $H_{rms} = 175$ m, and (i-l) show the experiment performed with the nominal observed value of $H_{rms} = 305$ m. As H_{rms} increases, the lifespan of vortices increases as well.

3. Linear Stability Analysis

To further explore the bathymetric stabilization, we perform the linear stability analysis of the primary vortex (32). The purpose of this inquiry is two-fold. The first objective is the confirmation of the link between vortex longevity, stability, and the bottom roughness. We wish to ascertain that the fragmentation of vortices for low H_{rms} is caused by linear instability, rather than by some unidentified nonlinear processes. Likewise, we would like to demonstrate that the vortex persistence for large H_{rms} can be attributed to their enhanced stability. The second benefit of the linear stability analysis is the opportunity to unambiguously determine the instability growth rate (λ) and its dependence on H_{rms}. We begin by linearizing the governing equations (27) about the basic state (32). For a two-layer system, this linearization yields

$$\begin{cases} \dfrac{\partial q_1'}{\partial t} + J(\overline{\psi}_1, q_1') + J(\psi_1', \overline{q}_1) = \nu \nabla^4 \psi_1' \\ \dfrac{\partial q_2'}{\partial t} + \dfrac{f}{H_2} J(\psi_2', \eta) = \nu \nabla^4 \psi_2', \end{cases} \tag{33}$$

where primes denote perturbations: $(\psi_i', q_i') = (\psi_i, q_i) - (\overline{\psi}_i, \overline{q}_i)$.

The linear simulations were initiated by the random distribution of ψ_i' and system (33) was integrated in time using the pseudo-spectral algorithm, analogous to the one used for the nonlinear simulations (Sec. 3.2). The evolution of the linear system is eventually dominated by the fastest exponentially growing mode with a well-defined growth rate. To quantify the magnitude of the perturbation and its evolutionary pattern, we use the spatially integrated specific energy

$$E'(t) = \frac{1}{2} \iint H_1 \left|\nabla \psi_1'\right|^2 + H_2 \left|\nabla \psi_2'\right|^2 + \frac{f^2}{g'} (\psi_1' - \psi_2')^2 \, dxdy. \tag{34}$$

The energy is non-dimensionalized by its initial value $E'(0)$, and the growth rate (λ) of the vortex instability is evaluated accordingly:

$$\lambda = \frac{1}{2}\frac{d}{dt}\ln\left(\frac{E'(t)}{E'(0)}\right). \tag{35}$$

Figure 18a presents $\frac{1}{2}\ln\left(\frac{E'(t)}{E'(0)}\right)$ as a function of time for the topographic variance ranging from $H_{rms} = 0$ to 400 m. In each case, after a brief initial period of adjustment (~ 3 months), the perturbation starts growing exponentially, as evidenced by the straight lines representing the energy records in logarithmic coordinates (Figure 18a). The slopes of these lines represent the growth rates (λ), which are evaluated as a best linear fit to the data in Figure 18a over the interval $t > 3$ months. The resulting growth rates are plotted as a function of H_{rms} and p in Figure 18b.

Figure 18. Linear analysis of the two-layer quasi-geostrophic model.

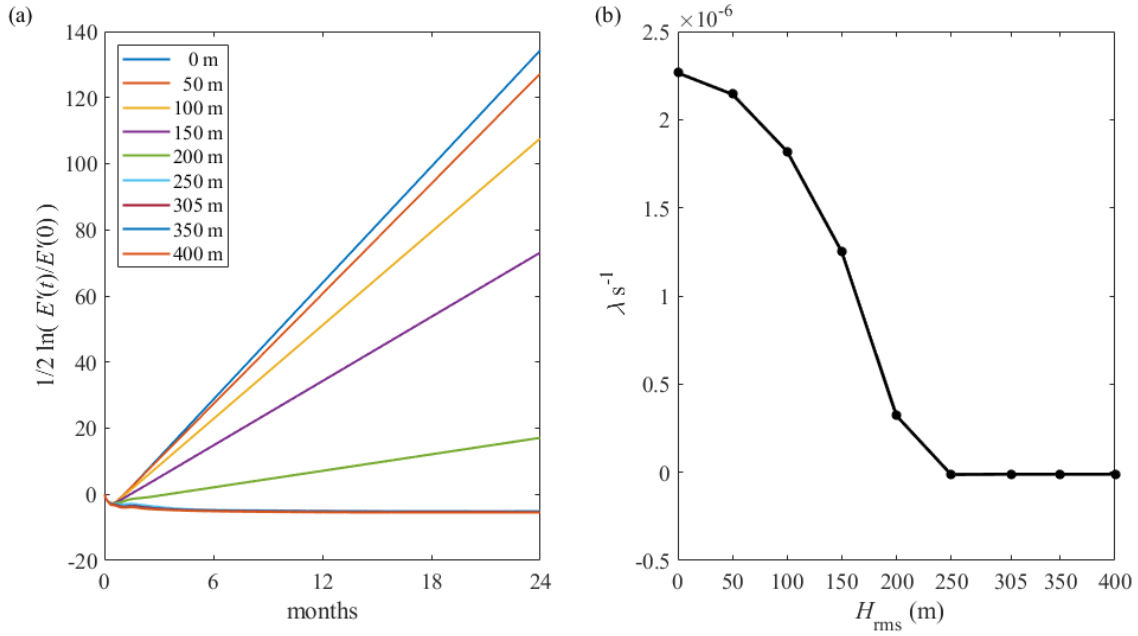

Panel (a) shows the natural log of the net perturbation energy for values of H_{rms} from 0 m to 400 m. Panel (b) presents the growth rate (λ) as a function of roughness (H_{rms}), illustrating the systematic weakening of vortex instability with increasing variance of sea-floor topography.

The linear analysis in Figure 18b leads to two key conclusions regarding bathymetric stabilization: (i) the vortex instability monotonically weakens with the increasing H_{rms}, and (ii) there exists a critical value of the depth variance $H_{cr} \sim 250$ m above which vortex becomes linearly stable $(\lambda < 0)$. It should be emphasized that the nominal value of the observed depth variance $H_{rms} = 305$ m suggested by Goff & Jordan (1988) exceeds H_{cr}. Thus, the stability condition $H_{rms} > H_{cr}$ is commonly met in the World Ocean. The apparent longevity of the observed ocean rings could therefore be attributed to the sandpaper effect—the adverse action of the small-scale topographic variability on the abyssal circulation. The foregoing stability analysis is also fully consistent with the nonlinear simulations (Sec. 3.2) revealing rapid vortex fragmentation for $H_{rms} < H_{cr}$ and their long-term persistence for $H_{rms} > H_{cr}$. For low values of H_{rms}, the growth rates are $\lambda \sim 10^{-6} s^{-1}$. The corresponding instability timescale is $\lambda^{-1} \sim 10$ days, which also reflects the vortex evolution in the nonlinear experiments.

Figure 19. Plot of the maximal azimuthal velocity (V_{max}) in each isopycnal layer coded by color.

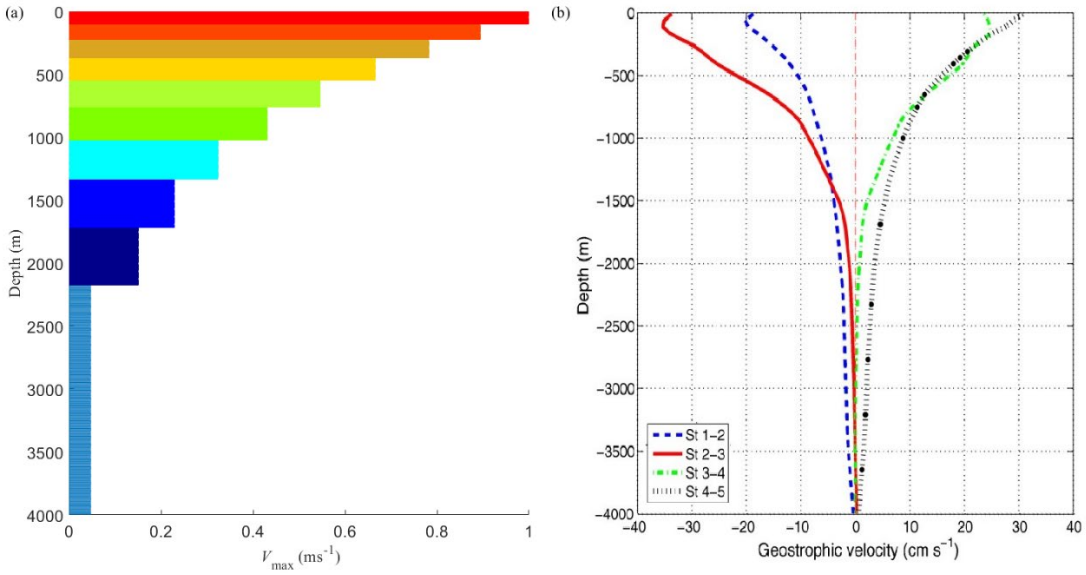

(a) Plot of the maximal azimuthal velocity. For comparison, (b) Four profiles of geostrophic velocity at CTD stations monitoring an Agulhas ring during the period 8 Feb – 10 March, 2010 (adapted from Casanova-Masjoan et al., 2017)

D. TEN-LAYER MODEL

The two-layer model of bathymetric stabilization (Sec. 3) offered a basic proof of concept and permitted the efficient exploration of the parameter space. However, it is prudent to ensure, at this point, that our inferences are not biased by the model's minimalistic representation of stratification. To this end, we present our second set of experiments in which the number of layers (n) is increased to ten. The height of each layer (H_i) increases from 100 m on the surface, to 2000 m at i=10. The lower layer is chosen to be relatively deep to ensure that the quasi-geostrophic requirement $\eta \ll H_n$ is met. To represent the surface-intensified ocean rings, we consider the circulation pattern that exponentially decreases with depth

$$\bar{\psi}_i = -A \exp(Z_i / H_0) \exp(-\alpha r^2), \tag{36}$$

where $\bar{\psi}_i$ $(i = 1,...,10)$ is the basic streamfunction in layer *i*, $H_0 = 1000$ m is the effective vertical extent of the ring, and Z_i is the location of the *i*-th layer center.

As in the two-layer case, A and α are chosen to yield the ring radius of $r_{\max} = 70$ km and the maximal surface velocity of $V_{\max} = 1\ \text{ms}^{-1}$. The resulting speed pattern is shown in Figure 19a, where the length of each bar represents the maximal azimuthal velocity in each layer and its vertical extent—the layer height. The chosen velocity pattern is consistent with observations of ocean rings. For instance, Figure 19b shows four profiles of geostrophic velocity in the interior of a South-Atlantic Agulhas ring (from Casanova-Masjoan et al., 2017). These measurements reveal that the velocity decreases with depth in a nearly exponential manner with the e-folding scale of approximately 1000 m, which is reflected in the employed vortex model (36).

The snapshots of the upper layer potential vorticity in Figure 20 reveal the evolution of vortices in experiments with H_{rms} values of 0 m, 175 m, and 305 m. As with the two-layer experiment, the vortex lifespan monotonically and dramatically increases with the increasing depth variance. In the flat bottom simulation (Figure 20a-e), the vortex loses coherence at $t \sim 120$ days, later than in the corresponding two-layer case, splitting into multiple smaller eddies. The vortex in Figure 20f-j $(H_{rms} = 175\ \text{m})$ does not exhibit signs of instability for six months before breaking apart, as seen in Figure 20j. Importantly, the vortex simulated using the nominal observed depth variance of $H_{rms} = 305$ m remains coherent throughout the entire two-year long experiment.

Figure 20. Ten-layer simulations.

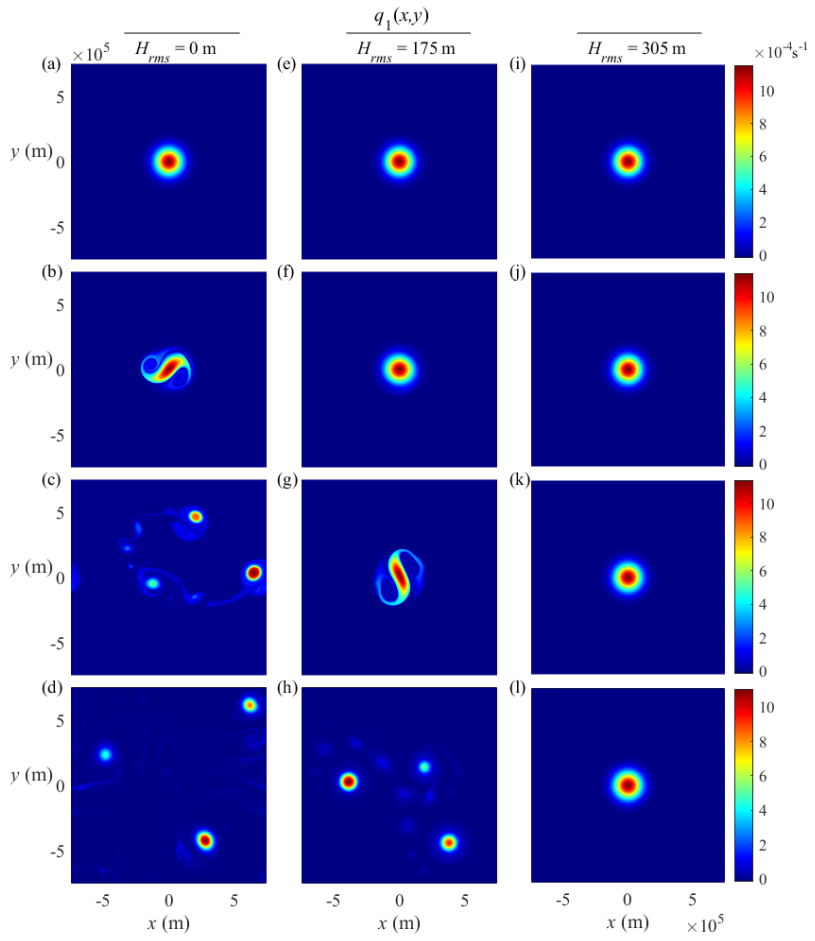

The same setup as Figure 17 for the ten-layer simulations at t=0, 4 months, 6 months, and 2 years. Panels (a-d), (e-h), and (i-l) represent the experiments performed for $H_{rms} = 0$, 175 m, and 305 m, respectively. As in the two-layer experiments, the lifespan of vortices increases with increasing H_{rms}.

E. SUMMARY OF CHAPTER III

The key outcome of this study is the discovery and validation of the "sandpaper" effect. We demonstrate that irregular topography of realistic magnitude and spatial pattern can stabilize large surface-intensified ocean rings by suppressing the circulation in the abyssal layer. Our numerical simulations indicate that vortices above a rough seafloor are much more robust and have larger lifespans than those over a flat bottom. The larger the magnitude of the depth variability, the more stable and long-lived are the modeled rings. Furthermore, we show that there is a critical value ($H_{cr} \sim 250$ m) of the depth variance above which the large-scale vortices are linearly stable. This condition ($H_{rms} > H_{cr}$) is unrestrictive and is met in many ocean regions.

Our results offer a plausible resolution of the long-standing stability conundrum—why large-scale ocean rings are stable and long-lived even when they satisfy the formal instability condition (Dritschel 1988). Concurrently, this work draws attention to the limitations of commonly used flat-bottom circulation theories and motivates efforts to parameterize the effects of bottom roughness on larger scales of motion.

The present study can be advanced in numerous directions by systematically increasing the complexity and realism of the model configuration. The minimal model used in our investigation can be extended to more general frameworks, such as the shallow-water and Navier–Stokes systems. In this regard, we note that the present quasi-geostrophic configuration a priori excludes several potentially significant topographic effects, including the lee-wave bottom drag (e.g., Eden et al., 2021; Klymak et al., 2021). Thus, the calculations in this study could underestimate the effects of variable topography on the dynamics of ocean rings. Furthermore, the present version of the sandpaper model does not represent topographic features with lateral extents less than 10 km —the limitation posed by the quasi-geostrophic approximation. However, such sub-mesoscale topographic features are widespread in the ocean (e.g., Goff, 2020) and can also affect the dynamics and stability of large-scale flows (Radko, 2020). Nevertheless, even the analysis of the most basic system suggests that the topographic influences on ocean rings could be profound and should be explored further.

IV. VIRTUAL LABORATORY EXPERIMENT ON THE INTERACTION OF A VORTEX WITH SMALL-SCALE TOPOGRAPHY

This study presents numerical analogs of laboratory experiments designed to explore the interaction of broad geophysical flows with irregular small-scale bathymetry. We validate the "sandpaper" theory of topographic forcing discussed in Chapter III and extend the analysis beyond the quasi-geostrophic and hydrostatic models. In agreement with theory, we observe (i) a major increase in spin-down rates of rotating flows above the rough bottom, (ii) the homogenization of small-scale potential vorticity, and (iii) the accelerated expulsion of motion from slow currents. These simulations are expected to guide the setup and parameter choice of future physical rotating tank experiments.

A. INTRODUCTION

The control of large-scale ocean circulation by the sea floor variability fascinated oceanographers for over a century. In some of the earliest rotating tank experiments, Taylor (1921) observed curving of surface flow around a cylinder placed on the bottom of the tank. In particular, researchers are becoming more aware of the effects of small-scale topography, commonly described as bottom roughness, on ocean circulation. Interaction with the topography may produce a secondary circulation which can reinforce mean flow (Holloway 1987, 1992) or create energy cascades which concentrate the mean flow into narrow currents (Vallis and Maltrud 1993).

Basic numerical simulations of ocean rings show that bottom roughness above a critical threshold may have radical effects on eddy stability, potentially adding years to their lifespan (Gulliver and Radko 2022b). This 'sandpaper effect' was further explored by Radko (2022), who used a multi-scale quasi-geostrophic model to show that even modest variation in seafloor depth may cause the rapid spin-down of basin-scale flows. A theoretical model was developed that accurately represented the eddy decay rate attributed to the irregular variability in the seafloor relief. The key physical mechanism of the topographic spin-down involves the homogenization of potential vorticity (PV). This

homogenization is caused by weak dissipative processes which systematically reduce variability of otherwise quasi-conservative potential vorticity (Rhines & Young, 1982). One example of this occurs in stationary atmospheric eddies which have a seasonal effect on climate due to interactions with the Earth's surface (Kirk-Davidoff and Lindzen 2000). For general circulation models, a parameterization of sub-scale topography could prove immeasurably valuable, making it possible to improve the accuracy of simulations without a major increase in resolution and associated computational costs. However, the effectiveness and precision of the proposed closure models must first be validated on a set of progressively realistic configurations that go beyond the original simplified quasi-geostrophic framework (Radko, 2022a,b).

The configuration we examine in this chapter is inspired by laboratory rotating tank experiments, which have been fully embraced by the oceanographic community as an effective tool for both education and research (McNoldy et al. 2003; Mackin et al. 2012). Laboratory oceanographic experiments provide a means for the direct observation of processes that are often difficult to explore in nature. Their ability to identify and isolate key mechanisms makes them an indispensable tool for the analyses of the basic physics at play. A relatively recent development in this area is brought by "virtually enhanced fluid laboratories"—a concept that takes advantage of the mutually reinforcing combination of ground-truth experiments and more accessible simulations (Illari et al. 2017). Following this approach, we perform simulations that represent the laboratory setup illustrated in Figure 21. The irregular topography in the anticipated physical experiments will conform to an observationally derived spectrum (Goff & Jordan, 1988) and will be manufactured using tiled 3D printing. While laboratory experiments are remarkably effective in terms of revealing the basic dynamics of rotating flows, the variety of circulation patterns that could be easily produced in a rotating tank is somewhat limited. For instance, a canonical Gaussian vortex model, commonly used in numerical simulations of ocean rings, could prove difficult to recreate in a rotating tank. Therefore, we anticipate using a simpler alternative. The water in the tank will be spun up into the solid-body rotation with the reference rotation rate (Ω_0). Then, the rotation rate will be changed by a relatively small amount $(\Delta\Omega \ll \Omega_0)$, forcing the flow over topography. Initially, the azimuthal velocity will

linearly increase with the distance from the tank center, and the circulation will gradually slow down until the azimuthal velocity matches the tank rotation once again. The PIV system will be used to monitor the flow over time.

Figure 21. Setup of the rotating tank experiment.

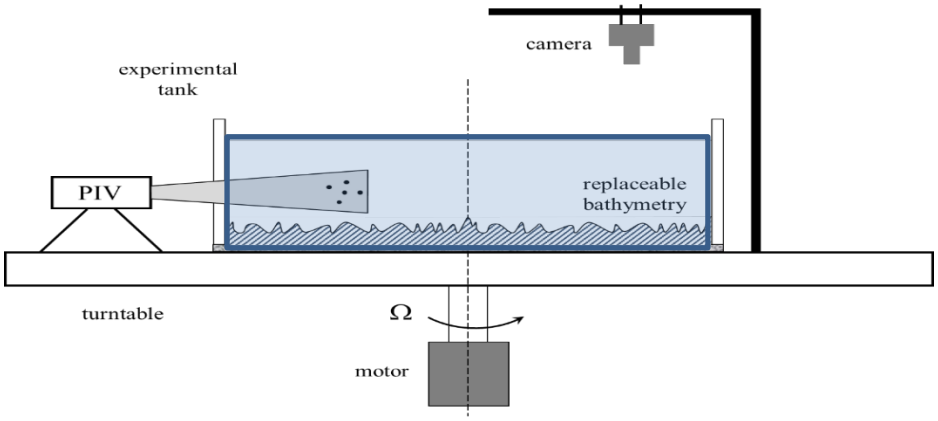

In this study, we examine the evolution of the flow field in the numerical analog of the envisioned experiment, which will pave the way for laboratory efforts and concurrently test the sandpaper model. In particular, the theory of Radko (2022a, b) offered three major predictions that require a numerical, laboratory, or observational validation: (i) irregular topography dramatically amplifies the spin-down rate, (ii) this reduction of velocity is caused by Reynolds stresses induced by topographically generated eddies, which, in turn, are controlled by PV-homogenization, and (iii) the accurate parameterization of the topographic spin-down can be developed using the spectrum of the seafloor depth. All three hypotheses will be validated using the results of virtual experiments. This study is organized as follows: Section B describes the numerical model and introduces governing equations. The setup of experiments is presented in Section C. The results are discussed in Section D and conclusions are listed in section E.

B. FORMULATION

To represent the proposed spinning up the flow into the solid body rotation and slightly changing the tank's rotation rate, we initiate simulations with linear the azimuthal velocity relative to the tank (V_0):

$$V_0(r) = \frac{V_{\max}}{R} r \tag{37}$$

where R is the tank radius, r is the distance from its center, and $(V_{\max})$ is the maximum velocity realized near the tank's wall.

A fundamental requirement for our analysis is a realistic bottom roughness model that reflects the observed seafloor patterns in the World Ocean. To that end, this study makes use of the empirical topographic spectrum of Goff and Jordan (1988), which is described by equation (29) in Chapter III. Following Gulliver and Radko (2022), we construct bottom topography as a sum of Fourier modes with random phases and spectral amplitudes conforming to (29). However, in the following simulations, the RMS height of topography (η_0) and its nominal wavenumbers (k_0, l_0) are scaled down to match the dimensions of the rotating tank.

To analyze the effects of the seafloor variability on large-scale flow patterns, we focus on the temporal variation of the mean azimuthal velocity $V(r,t)$. This quantity is computed by azimuthally averaging the local velocities and comparing them to the vortex spin-down model of Radko (2022a). The key result of the sandpaper theory (Radko, 2022a) is the large-scale model in which topography is parameterized as follows:

$$\frac{\partial \nabla^2 \psi}{\partial t} + J(\psi, \nabla^2 \psi) + \beta \frac{\partial \psi}{\partial x} + D + \gamma \nabla^2 \psi = 0\,, \tag{38}$$

where ψ is the streamfunction associated with the large-scale flow (u,v) and D is the topographic forcing given by

$$D = G\left(\frac{\partial}{\partial x}\left(\frac{v}{u^2+v^2}\right)-\frac{\partial}{\partial y}\left(\frac{u}{u^2+v^2}\right)\right). \tag{39}$$

The coefficient G in (39) is fully determined by the topographic spectrum, which in our case is based on the Goff-Jordan model, and the dissipation parameters:

$$G = 2\pi\int_{\kappa_{\min}}^{\kappa_{\max}} \frac{\mu-2}{(2\pi)^3}\left(\frac{f_0 h}{H k_0}\right)^2\left(1+\left(\frac{\kappa}{2\pi k_0}\right)^2\right)^{-\frac{\mu}{2}}\left(\frac{\gamma}{\kappa}+\upsilon\kappa\right)\mathrm{d}\kappa, \tag{40}$$

where υ in the present context represents molecular viscosity, $\kappa = \sqrt{k^2+l^2}$, H is fluid depth, h is the nominal scale of the RMS depth variability, $[\kappa_{\min}, \kappa_{\max}]$ is the range of wavenumbers present in the bathymetric spectrum, and $\gamma = \frac{1}{H}\sqrt{\frac{f\nu}{2}}$ is the Ekman bottom drag coefficient.

Eq. (38) can be cast in a more tractable form by rewriting it in the polar coordinate system (r,θ) and assuming that the large-scale flow is predominantly azimuthal and circularly symmetric. The azimutal velocity $V_{theor} = \frac{\partial\psi}{\partial r}$ in this case varies with the distance from the tank center (r), but is independent of the polar angle θ, which reduces (38) to

$$\frac{\partial V_{theor}}{\partial t} = -\frac{G}{V_{theor}} - \gamma V_{theor}. \tag{41}$$

Eq.(41) can be readily solved for $V_{theor} = V_{theor}(r,t)$:

$$V_{theor} = \sqrt{\exp(-2\gamma t)\left(V_0^2+\frac{G}{\gamma}\right)-\frac{G}{\gamma}}. \tag{42}$$

Hence, the spin-down is controlled by the initial azimuthal velocity V_0, bottom friction γ, and by the pattern of seafloor roughness that determines the coefficient G. However, it is the dependence of spin-down on the topography that is central to our

discussion. Note that the topographic forcing, represented by the first term on the right-hand-side of (41) is inversely dependent on the velocity. Therefore, we expect the rapid expulsion of motion from slow parts of the flow, whereas relatively strong currents will not be significantly affected by the topography. Testing this somewhat counterintuitive proposition is one of the main objectives of the virtual laboratory experiments that are presented next.

C. VIRTUAL LABORATORY EXPERIMENT

The virtual laboratory simulations represent circulation in a typical rotating tank with $R = 1\,\mathrm{m}$ radius and the water depth of $H^* = 50\,\mathrm{cm}$. We employ the Massachusetts Institute of Technology general circulation model (MITgcm), chosen for its flexible design and non-hydrostatic capabilities (Campin et al. 2022). In order to fully resolve topography, we truncate the bathymetric spectrum at the minimal wavelength of $L_{\min} = \frac{2\pi}{\kappa_{\max}} = 1\,\mathrm{cm}$. The simulations were performed using the barotropic model that assumes a vertically uniform motion throughout the water column. This simplification dramatically reduces the computational cost of simulations by removing the requirement to resolve the Ekman circulation in the bottom boundary layers, which makes simulations prohibitively expensive for variable topography. Thus, the flow field is effectively two-dimensional and is resolved by a Cartesian grid of $Nx \times Ny = 1024 \times 1024$, delivering a 2 mm lateral resolution. We assume a homogeneous temperature of 20 ˚C and perform simulations in the non-hydrostatic mode. The molecular viscosity of water is $\upsilon = 1\times10^{-6}\ \mathrm{m^2 s^{-1}}$ and the corresponding bottom drag coefficient is $\gamma = \frac{1}{H_0}\sqrt{\frac{\upsilon f}{2}} = 2\cdot10^{-3}\,s^{-1}$ and $\beta = 0$. For these simulations, we made use of MITgcm's capability to discretize partially-filled 'shaved cells' designed for resolving sub-grid topography (Adcroft et al. 1997). A Coriolis parameter of $f = 2\ \mathrm{s^{-1}}$ is assigned based on previously vetted rotating tank experiments (Chen 2022; van Heijst and Clercx 2009; McNoldy et al. 2003; Tian et al. 2001).

To represent the slight reduction of the rotation rate by $\Delta\Omega/\Omega_0 = 0.02$ that forces the fluid motion relative to the tank (Fig. 21), we initiate simulations using the linear pattern (37) with a maximum velocity of $V_{\max} = 0.02$ ms^{-1}. The impact of planetary rotation on oceanic flows is traditionally quantified by the Rossby number:

$$Ro = \frac{V_{\max}}{fL}. \tag{43}$$

and the chosen value of $V_{\max}$ ensures that the Rossby numbers in the experiment are commensurate with their oceanic counterparts. We also note that the very definition of the Rossby number may be ambiguous, as it is dependent on the choice of a relevant lateral scale (L). In the present problem, one can identify at least three distinct scales. $L_1 = 2$ m is the diameter of the tank, and it corresponds to $Ro_1 = 0.01,$ which conforms to the Rossby numbers of large ocean rings. Scale $L_2 = 1/k_0$ represents the typical wavelength of rough topography, resulting in $Ro_2 = 0.09$ which is, again, broadly consistent with the oceanic parameters. The smallest scale present in the system is $L_{\min}$ which represents submesoscale processes with $Ro_3 = 1$.

The baseline simulation (ExpB) is based on a nominal wavenumber of the Goff-Jordan spectrum chosen to be $k_0 = l_0 = 9$ m^{-1} and the RMS variation in depth of $h_{rms} = 3$ cm. Two other experiments are performed to test the sensitivity to the variation in the vertical and (ExpH) horizontal (ExpK) scale of the bottom relief. Their distinguishing parameters are listed in Table 2. Finally, to identify features, we present the corresponding flat bottom experiment (ExpFB). Two quantitative points of comparison of simulations with the sandpaper theory are based on (i) the evidence of the expulsion of weak flows, suggested by (41) and (ii) the tendency of the PV-homogenization—one of the pillars of the sandpaper theory Radko (2022a, b) . The latter objective is accomplished by computing the correlation coefficient,

$$r_{corr} = -\frac{\langle \eta\zeta \rangle}{\sqrt{\langle \eta^2 \rangle}\sqrt{\langle \zeta^2 \rangle}}, \tag{44}$$

where η is the variation in topographic height, and $\zeta = (\partial v/\partial x - \partial u/\partial y)$ is the relative vorticity, and angle brackets represent the spatial averaging. In quasi-geostrophic flows with fully homogenized PV, the small-scale relative vorticity (ζ) and the topographic height (η) represent mirror images of each other and therefore $r_{corr-full} = 1$. Thus, the proximity of r_{corr} to this limiting value will offer a convenient measure of performance of the homogenization realized in simulations. These results will be discussed in the next section.

Table 2. A summary of the virtual lab simulations.

	ExpB	**ExpK**	**ExpH**	**ExpFB**	**ExpOC**
$k_0=l_0$	9 m^{-1}	18 m^{-1}	9 m^{-1}	N/A	1.8 x 10–^{4} m^{-1}
h_{rms}	3 cm	3 cm	2 cm	0	305 m
r_{corr} $(t = 180)$	0.93	0.93	0.93	N/A	0.86 (t = 7 days)
r_{corr} $(t = 360)$	0.96	0.95	0.96	N/A	0.85 (t = 14 days)
r_{corr} $(t = 540)$	0.93	0.93	0.97	N/A	0.81 (t = 28 days)

D. RESULTS

The convincing evidence for PV-homogenization is presented in Figure 22, which shows the flow fields realized for all three standard tank experiments at $t = 360$ s. The magnified views of ζ (Figure 22a, c, e) and η (Figure 22b, d, f) mirror each other in fine detail. To offer a more quantitative assessment, we also present r_{corr} values for all experiments in Table 1 at $t = 180$ s, when the simulation has reached a fully equilibrated state, $t = 360$ s and $t = 540$ s. Over the period $180 \text{ s} < t < 540 \text{ s}$, r_{corr} remains limited to the range from 0.93 to 0.97 for all virtual laboratory experiments. This further supports the sandpaper theory of flow-topography interaction (Radko 2022a) and, in particular, the PV-homogenization origin of the small-scale eddies and the associated Reynolds stresses.

An essential component of the following analysis is based on the azimuthally averaged velocity, $V(r,t)$, which is diagnosed from simulations summarized in Table 2. One of the intriguing questions this analysis may shed light on is the relative significance of the topographic form drag and the Reynolds stresses in the flow spin-down. Because form drag increases with velocity, its effects would be strongest near the tank wall $(r \to R)$. The topographic forcing induced by the Reynolds stresses, on the other hand, decreases with the increasing velocity (Radko 2022a, b) and therefore it is expected to affect the flow near the axis $(r \to 0)$. Figure 23, shows the radial patterns of V diagnosed from all virtual laboratory simulations at 180 s, 360 s and 540 s. The comparison of the topography-resolving and flat-bottom simulations shows that rough topography indeed enhances the vortex spin-down. The effect is more pronounced near the tank center, which concurrently validates the weak-flow expulsion hypothesis and suggests that the form drag plays only a secondary role in the spin-down dynamics. As time progresses, the spin-down rate increases in each of the topographic simulations, and by $t = 540$ s their dissimilarities with the flat-bottom experiment become glaringly obvious (Figure 23c, f, g). It is also comforting to see that the spin-down theory (42), denoted by the dashed black line, adequately represents all experiments. This indicates that the sandpaper model captures essential processes even in the present—non-hydrostatic and non quasi-geostrophic—system.

Figure 22. Topographic mirroring in relative vorticity.

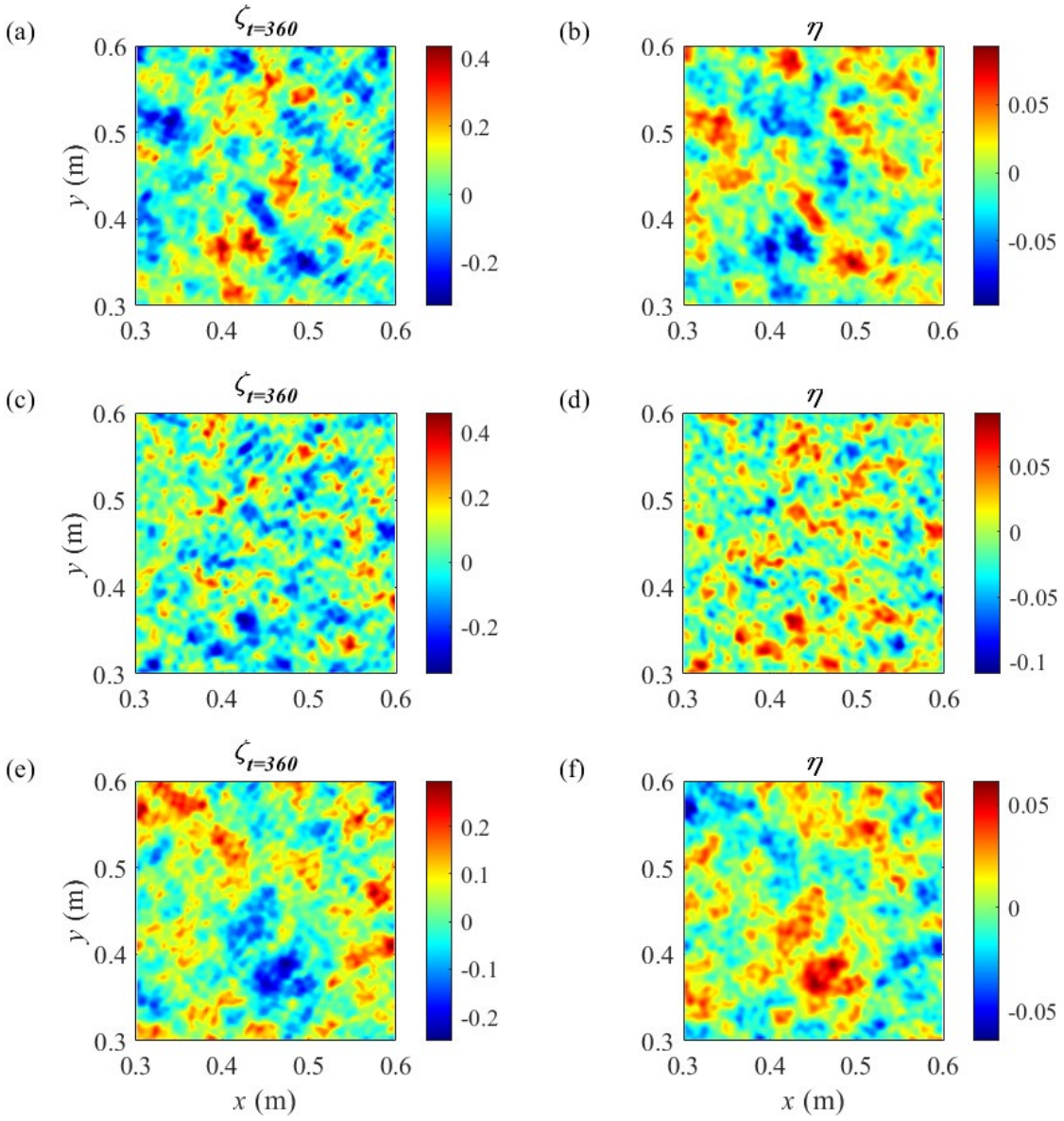

Plotted here are ζ at t=360 s and η respectively for ExpB (a-b), ExpK (c-d) and ExpH (e-f). A strong anticorrelation between vorticity and topography is maintained in all three experiments as listed in Table 2.

Figure 23. Azimuthal velocities for virtual experiments.

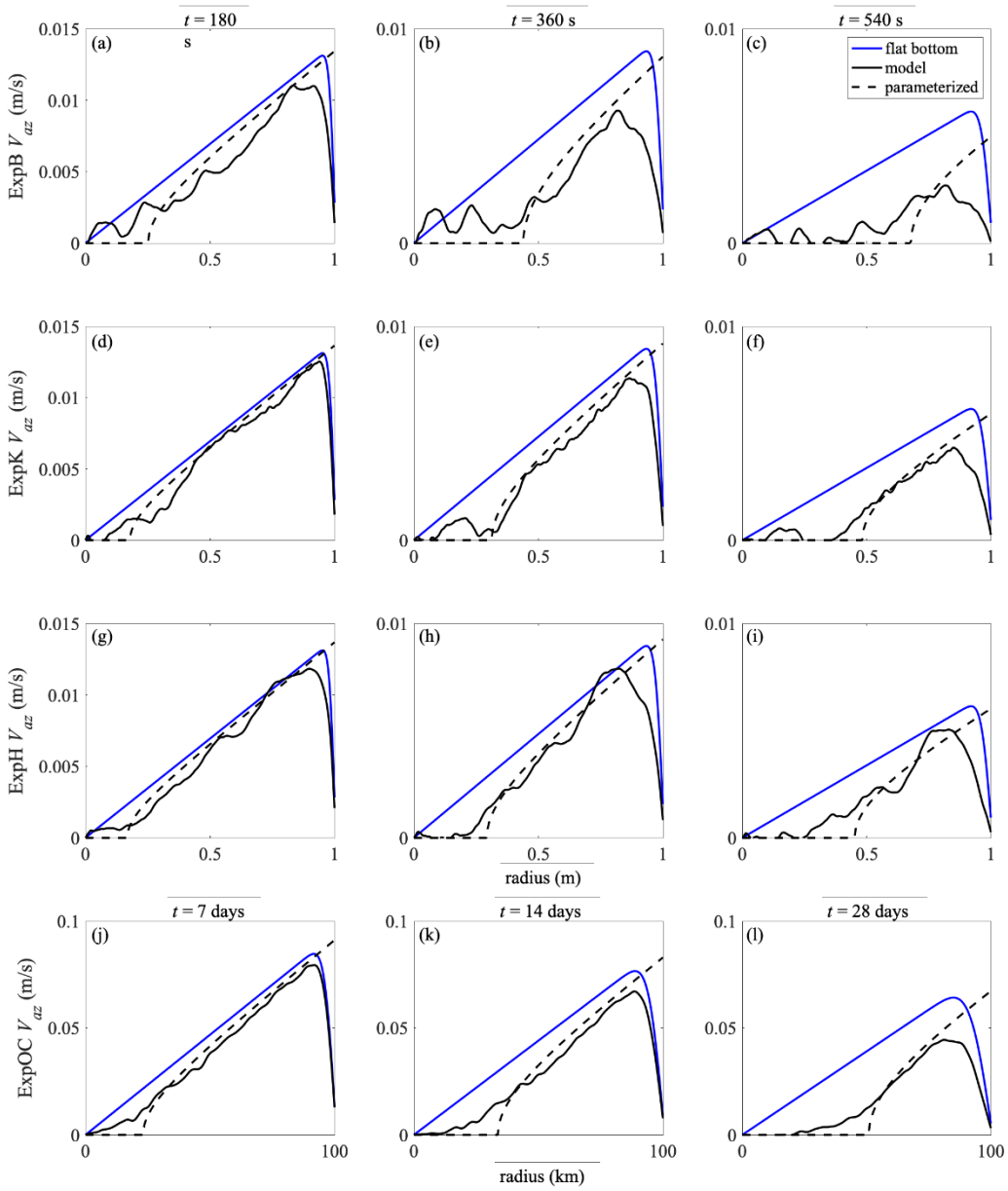

Azimuthal velocity profiles for ExpB (a-c), ExpK (d-f), and ExpH (g-i) and ExpOC (j-l) at t = 180 s, 360 s and 540 s. The blue line represents the flat bottom ExpFB , solid black is the respective topographic simulation and the dashed line is the theoretical model (42).

Finally, to ensure that the dynamics captured by the virtual laboratory experiments remain relevant for oceanic scales, we conducted an experiment (ExpOC) with $R = 100$ km $V_{\max} = 0.1\ \mathrm{ms}^{-1}$, $H_0 = 4$ km, $\upsilon = 10\ \mathrm{m}^2\mathrm{s}^{-1}$, and $\gamma = 1\times10^{-7}\ \mathrm{s}^{-1}$. It should be emphasized, however, that the dissipation parameters υ and γ in the ocean-scale simulation represent eddy-induced (rather than molecular) processes. Their values were chosen based on estimates in Li et al. (2018) and Arbic & Flierl (2004). The topography for this experiment was reconstructed using $k_0 = l_0 = 1.8\times10^{-4}\ \mathrm{m}^{-1}$ and $h_{\max} = 305$ m, as suggested by Nikurashin et al. (2014). ExpOC resulted in slightly lower r_{corr}, ranging from 0.81 to 0.86 as listed in Table 2. However, the V patterns shown in Fig. 23(j-l) at $t = 7, 14,$ and 28 days show that topographically-induced spin-down plays an even greater role in ExpOC than in the virtual tank simulations. Most notably, the theoretical model (42) remains fully consistent with the topography-resolving simulation.

E. SUMMARY OF CHAPTER IV

This investigation examines the effects of small-scale irregular topography on large-scale flows using virtual rotating tank simulations. Our conclusion advances previous studies, which were limited to quasi-geostrophic systems. The sandpaper effect—rapid suppression of large-scale flows by rough topography—is shown to be robust and model-independent, which instills confidence that is realized in many areas of the World Ocean. All experiments support the predicted tendency for the expulsion of weak motions by rough topography and provide evidence of PV homogenization. We also find that the previously derived parameterization of Reynolds stresses (Radko 2022a, b) adequately captures the spin-down dynamics. This investigation sets the stage for future physical rotating tank laboratory experiments, which will employ 3D printing for manufacturing the irregular bottom topography and PIV for visualization. These experiments can further validate our theoretical predictions and move us a step further to the final frontier: parameterization of the effects of rough topography in operational models.

V. CONCLUSIONS

In this investigation we explored several environmental factors which influence the lifespan of large coherent vortices, exemplified by Agulhas and Gulf Stream rings. Through this research, three controlling mechanisms for vortex longevity were determined: (i) the vortices ability to adjust to the ambient large-scale currents, (ii) the stabilization caused by rough topography and (iii) the bathymetric spin-down of the eddy's abyssal flows.

Our exploration commences with a set of experiments and the associated theory (Chapter II) characterizing the dynamics of vortices embedded in ambient vertical shear flows. This study examined the possibility of vortex adjustment to a quasi-equilibrium state and the ramifications of this transition for the vortex longevity. The extent to which a vortex evolves towards the so-called Translationally Adjusted Vortical State (TAVS) is controlled by the properties of ambient large-scale flows. Particularly important is the direction of shear flow, as westward flows create favorable conditions for quasi-uniform zonal propagation. In eastward flows, on the other hand, vortices generally fail to approach TAVS as they rapidly move towards their rest latitudes and disintegrate on relatively short timescales. The ambient baroclinic instability adversely affects the adjustment of the vortex to the TAVS. While vortices in eddying westward flows still partially adjust, their eastward counterparts are much more fragile and short-lived. This east-west asymmetry is evidenced by satellite and drifter observations which track eddies in western currents for several years. It also provides opens an exciting opportunity to explore the adjustment tendency in oceanographic datasets and comprehensive general circulation models

In Chapters III and IV, we explored the effects of small-scale irregular topography on ocean rings. First (Chapter III) we find that small-scale topography prolongs the lifespan of large vortices by enhancing their stability. The variability in seafloor depth tends to suppress abyssal flows, which, in turn, has a detrimental effect on baroclinic instability. The quasi-geostrophic simulations using realistic seafloor patterns proved that irregular small-scale topography can dramatically reduce the growth rate of instability. Above a certain fairly modest amplitude of topographic variability—which is commonly realized in

the ocean— vortices become linearly stable. This tendency was aptly named the "sandpaper effect," a reference to the friction provided by the abrasive small-scale particles of a sandpaper. These simulations instilled confidence that the sandpaper effect is realized in nature and must be studied further.

Chapter IV attempts to further validate the sandpaper effect by abandoning the quasi-geostrophic and hydrostatic approximations assumed earlier (Chapter III). The configuration chosen for this study represents a virtual tank experiment, which was performed using MITgcm, a comprehensive and versatile model suitable for non-hydrostatic simulations on laboratory scales. This experiment was designed to stimulate and guide future laboratory experiments on the interaction of rotating flows with irregular topography. These virtual tank experiments unequivocally proved that the sandpaper effect is realized even in non-hydrostatic and non quasi-geostrophic flows. The basis for this conclusion is two-fold. First, we see clear evidence of the small-scale homogenization of potential vorticity—a cornerstone of the sandpaper theory of Radko (2022a,b)—with levels of homogenization as high as 97%. In addition, we confirmed the peculiar inverse relationship between velocity and topographic forcing, predicted by the sandpaper theory. This relation is manifested very clearly through an expulsion of weak flows, where the gentler currents are rapidly suppressed, while the swift ones are much less affected by topography. The results show that the expulsion of weak flows is consistently represented by both the sandpaper theory and MITgcm based simulations, and is key to the theory of vortex spin-down. We also validate the spin-down model using the virtual laboratory experiments and show that it is even more accurate at oceanic scales. . The inclusion of parameterizations based on the sandpaper theory will likely improve their forecasting skills without the increase in resolution and associated computational costs.

While this work has tangibly advanced our understanding of the dynamics, stability, and maintenance mechanisms of coherent vortices, these research areas are still far from complete. The next step is to have the effects of adjustment and topography verified using field data from ocean research. Joint venture projects, like the Naval Oceanography Partnership Program (NOPPS), provide the ideal framework for collecting and sampling data used for verifying theory such as this. These projects build teams of researchers from

universities, industry, and government organizations around the globe to collaborate on efforts to investigate fundamental research questions such as the ones addressed here. In addition, the upcoming launch of the NASA/CNES Surface Water and Ocean Topography satellite (SWOT) will be a game changer, with a 2 km grid and daily sample rate that will spatially and temporally resolve even the smallest of eddies. There is also an implied need for higher resolution deep-water ocean mapping. With the benefit of deep water hydrographic vessels like the HMS Scott, AUVs, and satellite altimetry, the scientific community is rapidly enhancing our understanding of the deep ocean landscape (Zwolak and Felski 2017; Caress et al. 2008; McNeill et al. 2005; Pappalardi et al. 2001).

Future theoretical advancements should be aimed at improving the representation of eddies in global models, particularly by capturing small-scale and typically unresolved phenomena that impact the vortex dynamics. These efforts should systematically increase the realism and complexity of model configurations, moving beyond the present quasi-geostrophic framework. With seemingly endless string of open questions and opportunities, it is clear that we still have a long way to go until the last chapter is written in the glamorous history of eddy research in oceanography.

More information on NOPPS and SWOT can be found at https://nopp.org and https://swot.jpl.nasa.gov respectively.

THIS PAGE INTENTIONALLY LEFT BLANK

LIST OF REFERENCES

Abernathey, R., and G. Haller, 2018: Transport by Lagrangian vortices in the eastern Pacific. *J. Phys. Oceanogr.*, **48**, 667–685, https://doi.org/10.1175/JPO-D-17-0102.1.

Abernathey, R. P., and J. Marshall, 2013: Global surface eddy diffusivities derived from satellite altimetry. *J. Geophys. Res. Oceans*, **118**, 901–916, https://doi.org/10.1002/jgrc.20066.

Adcroft, A., C. Hill, and J. Marshall, 1997: Representation of topography by shaved cells in a height coordinate ocean model. *Mon. Weather Rev.*, **125**, 2293–2315.

Aguedjou, H. M. A., I. Dadou, A. Chaigneau, Y. Morel, and G. Alory, 2019: Eddies in the Tropical Atlantic Ocean and Their Seasonal Variability. *Geophys. Res. Lett.*, **46**, 12156–12164, https://doi.org/10.1029/2019GL083925.

Alvarez, A., J. Tintoré, G. Holloway, M. Eby, and J. M. Beckers, 1994: Effect of topographic stress on circulation in the western Mediterranean. *J. Geophys. Res.*, **99**, 16053, https://doi.org/10.1029/94JC00811.

Arbic, B. K., and G. R. Flierl, 2004: Baroclinically unstable geostrophic turbulence in the limits of strong and weak bottom Ekman friction: application to midocean eddies. *J. Phys. Oceanogr.*, **34**, 2257–2273.

Armi, L., and W. Zenk, 1984: Large Lenses of Highly Saline Mediterranean Water. *J. Phys. Oceanogr.*, **14**, 1560–1576, https://doi.org/10.1175/1520-0485(1984)014%3C1560:LLOHSM%3E2.0.CO;2.

Bakun, A., 2006: Fronts and eddies as key structures in the habitat of marine fish larvae: opportunity, adaptive response and competitive advantage. *Sci. Mar.*, **70**, 105–122, https://doi.org/10.3989/scimar.2006.70s2105.

Bell, T. H., 1975: Statistical features of sea-floor topography. *Deep Sea Res. Oceanogr. Abstr.*, **22**, 883–892, https://doi.org/10.1016/0011-7471(75)90090-X.

Benilov, E. S., 1996: Beta-induced translation of strong isolated eddies. *J. Phys. Oceanogr.*, **26**, 2223–2229, https://doi.org/10.1175/1520-0485(1996)026%3C2223:BITOSI%3E2.0.CO;2.

——, 2005: Stability of a two-layer quasigeostrophic vortex over axisymmetric localized topography. *J. Phys. Oceanogr.*, **35**, 123–130, https://doi.org/10.1175/JPO-2660.1.

——, 2018: Can large oceanic vortices be stable? *Geophys. Res. Lett.*, **45**, 1948–1954, https://doi.org/10.1002/2017GL076939.

Benilov, E. S., and J. D. Flanagan, 2008: The effect of ageostrophy on the stability of vortices in a two-layer ocean. *Ocean Model.*, **23**, 49–58, https://doi.org/10.1016/j.ocemod.2008.03.004.

Beron-Vera, F. J., Y. Wang, M. J. Olascoaga, G. J. Goni, and G. Haller, 2013: Objective detection of oceanic eddies and the Agulhas leakage. *J. Phys. Oceanogr.*, **43**, 1426–1438, https://doi.org/10.1175/JPO-D-12-0171.1.

Brach, L., P. Deixonne, M. F. Bernard, E. Durand, M.-C. Desjean, E. Perez, E. van Sebille, and A. ter Halle, 2018: Anticyclonic eddies increase accumulation of microplastic in the North Atlantic subtropical gyre. *Mar. Pollut. Bull.*, **126**, 191–196, https://doi.org/10.1016/j.marpolbul.2017.10.077.

Bretherton, F. P., and D. B. Haidvogel, 1976: Two-dimensional turbulence above topography. *J. Fluid Mech.*, **78**, 129–154, https://doi.org/10.1017/S002211207600236X.

Brown, J. M., L. T. Gulliver, and T. Radko, 2019: Effects of topography and orientation on the nonlinear equilibration of baroclinic instability. *J. Geophys. Res. Oceans*, **124**, 6720–6734, https://doi.org/10.1029/2019JC015297.

Byrne, D. A., A. L. Gordon, and W. F. Haxby, 1995: Agulhas eddies: A synoptic view using Geosat ERM data. *J. Phys. Oceanogr.*, **25**, 902–917, https://doi.org/10.1175/1520-0485(1995)025%3C0902:AEASVU%3E2.0.CO;2.

Campin, J.-M., and Coauthors, 2022: *MITgcm/MITgcm: checkpoint68i*. Zenodo,.

Caress, D., and Coauthors, 2008: High-resolution multibeam, sidescan, and subbottom surveys using the MBARI AUV. *Marine Habitat Mapping Technology for Alaska*, J. Reynolds and H. Greene, Eds., Alaska Sea Grant, University of Alaska Fairbanks, 47–70.

Casanova-Masjoan, M., J. L. Pelegrí, P. Sangrà, A. Martínez, D. Grisolía-Santos, M. D. Pérez-Hernández, and A. Hernández-Guerra, 2017: Characteristics and evolution of an Agulhas ring. *J. Geophys. Res. Oceans*, **122**, 7049–7065, https://doi.org/10.1002/2017JC012969.

Chaigneau, A., M. Le Texier, G. Eldin, C. Grados, and O. Pizarro, 2011: Vertical structure of mesoscale eddies in the eastern south Pacific ocean: A composite analysis from altimetry and Argo profiling floats. *J. Geophys. Res.*, **116**, C11025, https://doi.org/10.1029/2011JC007134.

Charney, J. G., 1948: On the scale of atmospheric motions. *Geofys. Publ.*, **17**, 251–265.

Charney, J. G., 1971: Geostrophic turbulence. *J. Atmospheric Sci.*, **28**, 1087–1095.

Charney, J. G., and M. E. Stern, 1962: On the stability of Internal baroclinic jets in a rotating atmosphere. *J. Atmospheric Sci.*, **19**, 159–172, https://doi.org/10.1175/1520-0469(1962)019%3C0159:OTSOIB%3E2.0.CO;2.

Chassignet, E. P., D. B. Olson, and D. B. Boudra, 1990: Motion and evolution of oceanic rings in a numerical model and in observations. *J. Geophys. Res.*, **95**, 22121, https://doi.org/10.1029/JC095iC12p22121.

Chavanis, P. H., and J. Sommeria, 2002: Statistical mechanics of the shallow water system. *Phys. Rev. E*, **65**, 026302, https://doi.org/10.1103/PhysRevE.65.026302.

Chelton, D. B., M. G. Schlax, R. M. Samelson, and R. A. de Szoeke, 2007: Global observations of large oceanic eddies. *Geophys. Res. Lett.*, **34**, https://doi.org/10.1029/2007GL030812.

——, ——, and ——, 2011: Global observations of nonlinear mesoscale eddies. *Prog. Oceanogr.*, **91**, 167–216, https://doi.org/10.1016/j.pocean.2011.01.002.

Chen, C., and I. Kamenkovich, 2013: Effects of topography on baroclinic instability. *J. Phys. Oceanogr.*, **43**, 790–804, https://doi.org/10.1175/JPO-D-12-0145.1.

Chen, G., and G. Han, 2019: Contrasting short-lived with long-lived mesoscale eddies in the global ocean. *J. Geophys. Res. Oceans*, **124**, 3149–3167, https://doi.org/10.1029/2019JC014983.

Chen, H.-C., 2022: Interaction of barotropic vortices over topography based on similarity laws: rotating tank experiment and shallow-water simulation. *Arab. J. Geosci.*, **15**, 276, https://doi.org/10.1007/s12517-022-09534-0.

Cheng, Y.-H., C.-R. Ho, Q. Zheng, and N.-J. Kuo, 2014: Statistical Characteristics of Mesoscale Eddies in the North Pacific Derived from Satellite Altimetry. *Remote Sens.*, **6**, 5164–5183, https://doi.org/10.3390/rs6065164.

Church, P. E., 1932: Surface temperatures of the Gulf Stream and Its bordering waters. *Geogr. Rev.*, **22**, 286, https://doi.org/10.2307/209180.

——, 1937: Temperatures of the western North Atlantic from thermograph records. *Secrétariat ssociation Univ.*,.

Cornillon, P., R. Weyer, and G. Flierl, 1989: Translational velocity of warm core rings relative to the slope water. *J. Phys. Oceanogr.*, **19**, 1317–1332, https://doi.org/10.1175/1520-0485(1989)019%3C1317:TVOWCR%3E2.0.CO;2.

Cushman-Roisin, B., T. Benyang, and E. P. Chassignet, 1990: Westward motion of mesoscale eddies. *J. Phys. Oceanogr.*, **20**, 758–768, https://doi.org/10.1175/1520-0485(1990)020%3C0758:WMOME%3E2.0.CO;2.

Dewar, W. K., 1998: Topography and barotropic transport control by bottom friction. *J. Mar. Res.*, **56**, 295–328, https://doi.org/10.1357/002224098321822320.

——, and P. D. Killworth, 1995: On the stability of oceanic rings. *J. Phys. Oceanogr.*, **25**, 1467–1487, https://doi.org/10.1175/1520-0485(1995)025%3C1467:OTSOOR%3E2.0.CO;2.

Dilmahamod, A. F., B. Aguiar-González, P. Penven, C. J. C. Reason, W. P. M. De Ruijter, N. Malan, and J. C. Hermes, 2018: SIDDIES corridor: A major east-west pathway of long-lived surface and subsurface eddies crossing the subtropical South Indian Ocean. *J. Geophys. Res. Oceans*, **123**, 5406–5425, https://doi.org/10.1029/2018JC013828.

Dritschel, D. G., 1988: Nonlinear stability bounds for inviscid, two-dimensional, parallel or circular flows with monotonic vorticity, and the analogous three-dimensional quasi-geostrophic flows. *J. Fluid Mech.*, **191**, 575, https://doi.org/10.1017/S0022112088001715.

Dugan, J. P., R. P. Mied, P. C. Mignerey, and A. F. Schuetz, 1982: Compact, intrathermocline eddies in the Sargasso Sea. *J. Geophys. Res.*, **87**, 385, https://doi.org/10.1029/JC087iC01p00385.

Early, J. J., R. M. Samelson, and D. B. Chelton, 2011: The Evolution and Propagation of Quasigeostrophic Ocean Eddies*. *J. Phys. Oceanogr.*, **41**, 1535–1555, https://doi.org/10.1175/2011JPO4601.1.

Eden, C., D. Olbers, and T. Eriksen, 2021: A closure for lee wave drag on the large-scale ocean circulation. *J. Phys. Oceanogr.*, **51**, 3573–3588, https://doi.org/10.1175/JPO-D-20-0230.1.

Frederiksen, J. S., and T. J. O'Kane, 2005: Inhomogeneous closure and statistical mechanics for Rossby wave turbulence over topography. *J. Fluid Mech.*, **539**, 137, https://doi.org/10.1017/S0022112005005562.

Fu, L.-L., D. Chelton, P.-Y. Le Traon, and R. Morrow, 2010: Eddy dynamics from satellite altimetry. *Oceanography*, **23**, 14–25, https://doi.org/10.5670/oceanog.2010.02.

Ganachaud, A., and C. Wunsch, 2003: Large-scale ocean heat and freshwater transports during the world ocean circulation experiment. *J. Clim.*, **16**, 696–705.

Gaube, P., C. D. Braun, G. L. Lawson, D. J. McGillicuddy, A. D. Penna, G. B. Skomal, C. Fischer, and S. R. Thorrold, 2018: Mesoscale eddies influence the movements of mature female white sharks in the Gulf Stream and Sargasso Sea. *Sci. Rep.*, **8**, 7363, https://doi.org/10.1038/s41598-018-25565-8.

Godø, O. R., A. Samuelsen, G. J. Macaulay, R. Patel, S. S. Hjøllo, J. Horne, S. Kaartvedt, and J. A. Johannessen, 2012: Mesoscale Eddies Are Oases for Higher Trophic Marine Life. *PLoS ONE*, **7**, e30161, https://doi.org/10.1371/journal.pone.0030161.

Goff, J. A., 2020: Identifying Characteristic and Anomalous Mantle From the Complex Relationship Between Abyssal Hill Roughness and Spreading Rates. *Geophys. Res. Lett.*, **47**, https://doi.org/10.1029/2020GL088162.

——, and T. H. Jordan, 1988: Stochastic modeling of seafloor morphology: inversion of sea beam data for second-order statistics. *J. Geophys. Res. Solid Earth*, **93**, 13589–13608, https://doi.org/10.1029/JB093iB11p13589.

Griffies, S. M., and Coauthors, 2015: Impacts on ocean heat from transient mesoscale eddies in a hierarchy of climate models. *J. Clim.*, **28**, 952–977, https://doi.org/10.1175/JCLI-D-14-00353.1.

Gulliver, L. T., and T. Radko, 2022a: On the propagation and translational adjustment of isolated vortices in large-scale shear flows. *J. Phys. Oceanogr.*, **52**, 1655–1675, https://doi.org/10.1175/JPO-D-21-0257.1.

Gulliver, L. T., and T. Radko, 2022b: Topographic stabilization of ocean rings. *Geophys. Res. Lett.*, **49**, https://doi.org/10.1029/2021GL097686.

Haller, G., 2005: An objective definition of a vortex. *J. Fluid Mech.*, **525**, 1–26, https://doi.org/10.1017/S0022112004002526.

Hart, J. E., 1975: Baroclinic instability over a slope. Part I: linear theory. *J. Phys. Oceanogr.*, **5**, 625–633, https://doi.org/10.1175/1520-0485(1975)005%3C0625:BIOASP%3E2.0.CO;2.

van Heijst, G. J. F., and H. J. H. Clercx, 2009: Laboratory modeling of geophysical vortices. *Annu. Rev. Fluid Mech.*, **41**, 143–164, https://doi.org/10.1146/annurev.fluid.010908.165207.

Holloway, G., 1987: Systematic forcing of large-scale geophysical flows by eddy-topography interaction. *J. Fluid Mech.*, **184**, 463–476, https://doi.org/10.1017/S0022112087002970.

——, 1992: Representing topographic stress for large-scale ocean models. *J. Phys. Oceanogr.*, **22**, 1033–1046, https://doi.org/10.1175/1520-0485(1992)022%3C1033:RTSFLS%3E2.0.CO;2.

Huxley, A., 2012: *Ends and means: an inquiry into the nature of ideals*. Transaction Publishers, 386 pp.

Ienna, F., I. Bashmachnikov, and J. Dias, 2022: Meddies and their sea surface expressions: Observations and theory. *J. Phys. Oceanogr.*, https://doi.org/10.1175/JPO-D-22-0081.1.

Illari, L., J. Marshall, and W. D. McKenna, 2017: Virtually Enhanced Fluid Laboratories for Teaching Meteorology. *Bull. Am. Meteorol. Soc.*, **98**, 1949–1959, https://doi.org/10.1175/BAMS-D-16-0075.1.

Iselin, C.-O., 1936: A study of the circulation of the western North Atlantic.

Isern-Fontanet, J., E. García-Ladona, and J. Font, 2003: Identification of marine rddies from altimetric maps. *J. Atmospheric Ocean. Technol.*, **20**, 772–778, https://doi.org/10.1175/1520-0426(2003)20%3C772:IOMEFA%3E2.0.CO;2.

——, J. Font, E. García-Ladona, M. Emelianov, C. Millot, and I. Taupier-Letage, 2004: Spatial structure of anticyclonic eddies in the Algerian basin (Mediterranean Sea) analyzed using the Okubo–Weiss parameter. *Deep Sea Res. Part II Top. Stud. Oceanogr.*, **51**, 3009–3028, https://doi.org/10.1016/j.dsr2.2004.09.013.

Jia, Y., P. H. R. Calil, E. P. Chassignet, E. J. Metzger, J. T. Potemra, K. J. Richards, and A. J. Wallcraft, 2011: Generation of mesoscale eddies in the lee of the Hawaiian Islands. *J. Geophys. Res.*, **116**, C11009, https://doi.org/10.1029/2011JC007305.

Kamenkovich, V. M., M. N. Koshlyakov, and A. S. Monin, 1986: *Synoptic Eddies in the Ocean*. D. Reidel Publ. Company, 433 pp.

Killworth, P. D., 1986: On the propagation of isolated multilayer and continuously stratified eddies. *J. Phys. Oceanogr.*, **16**, 709–716, https://doi.org/10.1175/1520-0485(1986)016%3C0709:OTPOIM%3E2.0.CO;2.

——, J. R. Blundell, and W. K. Dewar, 1997: Primitive equation instability of wide oceanic rings. Part I: linear theory. *J. Phys. Oceanogr.*, **27**, 941–962.

Kirk-Davidoff, D. B., and R. S. Lindzen, 2000: An Energy Balance Model Based on Potential Vorticity Homogenization. *J. Clim.*, **13**, 431–448.

Klocker, A., and R. Abernathey, 2014: Global patterns of mesoscale eddy properties and diffusivities. *J. Phys. Oceanogr.*, **44**, 1030–1046, https://doi.org/10.1175/JPO-D-13-0159.1.

Klymak, J. M., D. Balwada, A. N. Garabato, and R. Abernathey, 2021: Parameterizing nonpropagating form drag over rough bathymetry. *J. Phys. Oceanogr.*, **51**, 1489–1501, https://doi.org/10.1175/JPO-D-20-0112.1.

Kravtsov, S., and G. Reznik, 2019: Numerical solutions of the singular vortex problem. *Phys. Fluids*, **31**, 066602, https://doi.org/10.1063/1.5099896.

LaCasce, J. H., J. Escartin, Eric. P. Chassignet, and X. Xu, 2019: Jet instability over smooth, corrugated, and realistic bathymetry. *J. Phys. Oceanogr.*, **49**, 585–605, https://doi.org/10.1175/JPO-D-18-0129.1.

Li, Q., L. Sun, and C. Xu, 2018: The lateral eddy viscosity derived from the decay of oceanic mesoscale eddies. *Open J. Mar. Sci.*, **08**, 152–172, https://doi.org/10.4236/ojms.2018.81008.

Mackin, K. J., N. Cook-Smith, L. Illari, J. Marshall, and P. Sadler, 2012: The Effectiveness of Rotating Tank Experiments in Teaching Undergraduate Courses in Atmospheres, Oceans, and Climate Sciences. *J. Geosci. Educ.*, **60**, 67–82, https://doi.org/10.5408/10-194.1.

Mahdinia, M., P. Hassanzadeh, P. S. Marcus, and C.-H. Jiang, 2017: Stability of three-dimensional Gaussian vortices in an unbounded, rotating, vertically stratified, Boussinesq flow: linear analysis. *J. Fluid Mech.*, **824**, 97–134, https://doi.org/10.1017/jfm.2017.303.

Maslowski, W., and W. H. Lipscomb, 2003: High resolution simulations of Arctic sea ice, 1979–1993. *Polar Res.*, **22**, 67–74, https://doi.org/10.3402/polar.v22i1.6445.

McNeill, L., T. Henstock, and D. Tappin, 2005: The eastern Indian ocean earthquake and tsunami : first seafloor survey by Royal Navy's HMS Scott. *Hydro Int.*, **9**, 7–9.

McNoldy, B. D., A. Cheng, Z. A. Eitzen, R. W. Moore, J. Persing, K. Schaefer, and W. H. Schubert, 2003: Design and construction of an affordable rotating table for classroom demonstrations of geophysical fluid dynamics principles. *Bull. Am. Meteorol. Soc.*, **84**, 1827–1834, https://doi.org/10.1175/BAMS-84-12-1827.

McWilliams, J. C., and G. R. Flierl, 1979: On the evolution of isolated, nonlinear vortices. *J. Phys. Oceanogr.*, **9**, 1155–1182, https://doi.org/10.1175/1520-0485(1979)009%3C1155:OTEOIN%3E2.0.CO;2.

Merryfield, W. J., and G. Holloway, 2002: Predictability of quasi-geostrophic turbulence. *J. Fluid Mech.*, **465**, 191–212, https://doi.org/10.1017/S0022112002001039.

de Miranda, A. P., B. Barnier, and W. K. Dewar, 1999: On the dynamics of the Zapiola Anticyclone. *J. Geophys. Res. Oceans*, **104**, 21137–21149, https://doi.org/10.1029/1999JC900042.

MODE group, 1978: The Mid-Ocean Dynamics Experiment. *Deep Sea Res.*, **25**, 859–910, https://doi.org/10.1016/0146-6291(78)90632-X.

Mory, M., 1985: Integral constraints on bottom and surface isolated eddies. *J. Phys. Oceanogr.*, **15**, 1433–1438, https://doi.org/10.1175/1520-0485(1985)015%3C1433:ICOBAS%3E2.0.CO;2.

Nikurashin, M., R. Ferrari, N. Grisouard, and K. Polzin, 2014: The impact of finite-amplitude bottom topography on internal wave generation in the southern ocean. *J. Phys. Oceanogr.*, **44**, 2938–2950, https://doi.org/10.1175/JPO-D-13-0201.1.

Nof, D., 1981: On the β-induced movement of isolated baroclinic eddies. *J. Phys. Oceanogr.*, **11**, 1662–1672, https://doi.org/10.1175/1520-0485(1981)011%3C1662:OTIMOI%3E2.0.CO;2.

——, 1983: On the migration of isolated eddies with application to Gulf Stream rings. *J. Mar. Res.*, **41**, 399–425, https://doi.org/10.1357/002224083788519687.

——, Y. Jia, E. Chassignet, and A. Bozec, 2011: Fast wind-induced migration of Leddies in the South China Sea. *J. Phys. Oceanogr.*, **41**, 1683–1693, https://doi.org/10.1175/2011JPO4530.1.

Nycander, J., 1988: New stationary vortex solutions of the Hasegawa–Mima equation. *J. Plasma Phys.*, **39**, 413–430, https://doi.org/10.1017/S0022377800026738.

Nycander, J., 1994: Steady vortices in plasmas and geophysical flows. *Chaos Interdiscip. J. Nonlinear Sci.*, **4**, 253–267, https://doi.org/10.1063/1.166006.

——, 2001: Drift velocity of radiating quasigeostrophic vortices. *J. Phys. Oceanogr.*, **31**, 2178–2185, https://doi.org/10.1175/1520-0485(2001)031%3C2178:DVORQV%3E2.0.CO;2.

Okane, T. J., and J. S. Frederiksen, 2004: The QDIA and regularized QDIA closures for inhomogeneous turbulence over topography. *J. Fluid Mech.*, **504**, 133–165, https://doi.org/10.1017/S0022112004007980.

Okubo, A., 1970: Horizontal dispersion of floatable particles in the vicinity of velocity singularities such as convergences. *Deep Sea Res. Oceanogr. Abstr.*, **17**, 445–454, https://doi.org/10.1016/0011-7471(70)90059-8.

Olson, D. B., 1991: Rings in the ocean. *Annu. Rev. Earth Planet. Sci.*, **19**, 283–311, https://doi.org/10.1146/annurev.ea.19.050191.001435.

Pappalardi, F., S. J. Dunham, and M. E. Leblang, 2001: HMS Scott: United Kingdom Ocean Survey Ship.

Pedlosky, J., 1983: The growth and decay of finite-amplitude baroclinic waves. *J. Atmospheric Sci.*, **40**, 1863–1876.

——, 1987: *Geophysical fluid dynamics*. 2nd ed. Springer-Verlag, 710 pp.

Petersen, M. R., S. J. Williams, M. E. Maltrud, M. W. Hecht, and B. Hamann, 2013: A three-dimensional eddy census of a high-resolution global ocean simulation. *J. Geophys. Res. Oceans*, **118**, 1759–1774, https://doi.org/10.1002/jgrc.20155.

Phillips, N. A., 1951: A simple three-dimensional model for the study of large-scale extratropical flow patterns. *J. Atmospheric Sci.*, **8**, 381–394, https://doi.org/10.1175/1520-0469(1951)008%3C0381:ASTDMF%3E2.0.CO;2.

Pinet, P. R., 2019: *Invitation to oceanography*. Eighth edition. Jones & Bartlett Learning, 598 pp.

Polyakov, I., 2001: An eddy parameterization based on maximum entropy production with application to modeling of the Arctic Ocean Circulation. *J. Phys. Oceanogr.*, **31**, 2255–2270, https://doi.org/10.1175/1520-0485(2001)031%3C2255:AEPBOM%3E2.0.CO;2.

Rabinovich, M., Z. Kizner, and G. Flierl, 2018: Bottom-topography effect on the instability of flows around a circular island. *J. Fluid Mech.*, **856**, 202–227, https://doi.org/10.1017/jfm.2018.705.

Radko, T., 2020a: Rectilinear propagation of quasi-monopolar vorticity patches. *J. Fluid Mech.*, **904**, A22, https://doi.org/10.1017/jfm.2020.667.

——, 2020b: Control of baroclinic instability by submesoscale topography. *J. Fluid Mech.*, **882**, A14, https://doi.org/10.1017/jfm.2019.826.

——, 2021: Playing pool on the beta-plane: how weak initial perturbations predetermine the long-term evolution of coherent vortices. *J. Fluid Mech.*, **915**, A89, https://doi.org/10.1017/jfm.2021.129.

——, 2022a: Spin-down of a barotropic vortex by irregular small-scale topography. *J. Fluid Mech.*, **944**, A5, https://doi.org/10.1017/jfm.2022.488.

——, 2022b: Spin-down of a baroclinic vortex by irregular small-scale topography. *J. Fluid Mech.*, **953**, A7.

——, and M. E. Stern, 1999: On the propagation of oceanic mesoscale vortices. *J. Fluid Mech.*, **380**, 39–57, https://doi.org/10.1017/S0022112098003371.

——, and ——, 2000: Self-propagating eddies on the stratified f-plane. *J. Phys. Oceanogr.*, **30**, 3134–3144.

——, and I. Kamenkovich, 2017: On the topographic modulation of large-scale eddying flows. *J. Phys. Oceanogr.*, **47**, 2157–2172, https://doi.org/10.1175/JPO-D-17-0024.1.

——, and C. Sisti, 2017: Life and demise of intrathermocline mesoscale vortices. *J. Phys. Oceanogr.*, **47**, 3087–3103, https://doi.org/10.1175/JPO-D-17-0044.1.

Reasor, P. D., M. T. Montgomery, and L. D. Grasso, 2004: A new look at the problem of tropical cyclones in vertical shear flow: vortex resiliency. *J. Atmospheric Sci.*, **61**, 3–22, https://doi.org/10.1175/1520-0469(2004)061%3C0003:ANLATP%3E2.0.CO;2.

Rhines, P. B., 1979: Geostrophic turbulence. *Annu. Rev. Fluid Mech.*, **11**, 401–441.

——, and W. R. Young, 1982: Homogenization of potential vorticity in planetary gyres. *J. Fluid Mech.*, **122**, 347, https://doi.org/10.1017/S0022112082002250.

Ring Group, 1981: Gulf Stream Cold-Core Rings: Their physics, chemistry, and biology. *Science*, **212**, 1091–1100, https://doi.org/10.1126/science.212.4499.1091.

Robinson, A. R., ed., 2012: *Eddies in marine science*. Springer, 609 pp.

Rossby, C. G., 1948: On displacements and intensity changes of atmospheric vortices. *J. Mar. Res.*, **Res 7**, 175–187.

Rossby, T., D. Dorson, and J. Fontaine, 1986: The RAFOS system. *J. Atmospheric Ocean. Technol.*, **3**, 672–679, https://doi.org/10.1175/1520-0426(1986)003%3C0672:TRS%3E2.0.CO;2.

Samelson, R. M., M. G. Schlax, and D. B. Chelton, 2014: Randomness, symmetry, and scaling of mesoscale eddy life cycles. *J. Phys. Oceanogr.*, **44**, 1012–1029, https://doi.org/10.1175/JPO-D-13-0161.1.

Sangrà, P., and Coauthors, 2009: The Canary Eddy Corridor: A major pathway for long-lived eddies in the subtropical North Atlantic. *Deep Sea Res. Part Oceanogr. Res. Pap.*, **56**, 2100–2114, https://doi.org/10.1016/j.dsr.2009.08.008.

Smyth, W. D., and J. R. Carpenter, 2019: *Instability in Geophysical Flows*. 1st ed. Cambridge University Press,.

Sokolovskiy, M. A., and J. Verron, 2014: *Dynamics of Vortex Structures in a Stratified Rotating Fluid*. 1st ed. 2014. Springer International Publishing : Imprint: Springer, 1 pp.

Sun, B., C. Liu, and F. Wang, 2019: Global meridional eddy heat transport inferred from Argo and altimetry observations. *Sci. Rep.*, **9**, 1345, https://doi.org/10.1038/s41598-018-38069-2.

Sutyrin, G., and T. Radko, 2016: Stabilization of isolated vortices in a rotating stratified fluid. *Fluids*, **1**, 26, https://doi.org/10.3390/fluids1030026.

Sutyrin, G. G., 2020a: How oceanic vortices can be super long-lived. *Phys. Oceanogr.*, **27**, https://doi.org/10.22449/1573-160X-2020-6-677-691.

Sutyrin, G. G., 2020b: How baroclinic vortices intensify resulting from erosion of their cores and/or changing environment. *Ocean Model.*, **156**, 101711, https://doi.org/10.1016/j.ocemod.2020.101711.

——, and T. Radko, 2019: On the peripheral intensification of two-dimensional vortices in smaller-scale randomly forcing flow. *Phys. Fluids*, **31**, 101701, https://doi.org/10.1063/1.5118752.

Sutyrin, G. G., and T. Radko, 2021: Why the most long-lived oceanic vortices are found in the subtropical westward flows. *Ocean Model.*, **161**, 101782, https://doi.org/10.1016/j.ocemod.2021.101782.

Sutyrin, G. G., T. Radko, and J. Nycander, 2021: Steady radiating baroclinic vortices in vertically sheared flows. *Phys. Fluids*, **33**, 031705, https://doi.org/10.1063/5.0040298.

Swallow, J. C., 1955: A neutral-buoyancy float for measuring deep currents. *Deep Sea Res. 1953*, **3**, 74–81, https://doi.org/10.1016/0146-6313(55)90037-X.

Talley, L. D., G. L. Pickard, and W. J. Emery, eds., 2011: *Descriptive Physical Oceanography: An Introduction*. 6th ed. Academic Press, 555 pp.

Taylor, G. I., 1921: Experiments with rotating fluids. *Proc. R. Soc. Lond. Ser. Contain. Pap. Math. Phys. Character*, **100**, 114–121, https://doi.org/10.1098/rspa.1921.0075.

Thoppil, P. G., J. G. Richman, and P. J. Hogan, 2011: Energetics of a global ocean circulation model compared to observations. *Geophys. Res. Lett.*, **38**, https://doi.org/10.1029/2011GL048347.

Tian, Y., E. R. Weeks, K. Ide, J. S. Urbach, C. N. Baroud, M. Ghil, and H. L. Swinney, 2001: Experimental and numerical studies of an eastward jet over topography. *J. Fluid Mech.*, **438**, 129–157, https://doi.org/10.1017/S0022112001004372.

Tomczak, M., and J. S. Godfrey, 2003: *Regional Oceanography: An Introduction*. 2. ed. Daya Publ. House, 390 pp.

Trott, C. B., B. Subrahmanyam, and E. S. Nyadjro, 2019: Influence of mesoscale features on mixed layer dynamics in the Arabian Sea. *J. Geophys. Res. Oceans*, **124**, 3361–3377, https://doi.org/10.1029/2019JC014965.

Vallis, G. K., 2017: *Atmospheric and Oceanic Fluid Dynamics: Fundamentals and Large-scale Circulation*. 2nd ed. Cambridge university press,.

——, 2019: *Essentials of atmospheric and oceanic dynamics*. Cambridge university press,.

——, and M. E. Maltrud, 1993: Generation of mean flows and jets on a beta plane and over topography. *J. Phys. Oceanogr.*, **23**, 1346–1362.

Vandermeirsh, F., Y. Morel, and G. G. Sutyrin, 2002: Resistance of a coherent vortex to a vertical shear. *J. Phys. Oceanogr.*, **32**, 3089–3100, https://doi.org/10.1175/1520-0485(2002)032%3C3089:ROACVT%3E2.0.CO;2.

Verron, J., and C. Le Provost, 1985: A numerical study of quasi-geostrophic flow over isolated topography. *J. Fluid Mech.*, **154**, 231–252, https://doi.org/10.1017/S0022112085001501.

Watanabe, E., and Coauthors, 2014: Enhanced role of eddies in the Arctic marine biological pump. *Nat. Commun.*, **5**, 3950, https://doi.org/10.1038/ncomms4950.

Weiss, J., 1991: The dynamics of enstrophy transfer in two-dimensional hydrodynamics. *Phys. Nonlinear Phenom.*, **48**, 273–294, https://doi.org/10.1016/0167-2789(91)90088-Q.

Williams, J., 1793: Memoir of Jonathan Williams, on the use of the Thermometer in Discovering Banks, Soundings, etc. *Trans. Am. Philos. Soc.*, **3(1793)**, 82–100.

Yim, E., P. Billant, and C. Ménesguen, 2016: Stability of an isolated pancake vortex in continuously stratified-rotating fluids. *J. Fluid Mech.*, **801**, 508–553, https://doi.org/10.1017/jfm.2016.402.

Zavala Sansón, L., 2019: Nonlinear and time-dependent equivalent-barotropic flows. *J. Fluid Mech.*, **871**, 925–951, https://doi.org/10.1017/jfm.2019.354.

Zhao, B., E. Chieusse-Gérard, and G. Flierl, 2019: Influence of bottom topography on vortex stability. *J. Phys. Oceanogr.*, **49**, 3199–3219, https://doi.org/10.1175/JPO-D-19-0049.1.

Zwolak, K., and A. Felski, 2017: Current state of deep ocean bathymetric exploration. *Annual of Navigation*, **24**, no. 1. doi:10.1515/aon-2017-0019.

INITIAL DISTRIBUTION LIST

1. Defense Technical Information Center
   Ft. Belvoir, Virginia

2. Dudley Knox Library
   Naval Postgraduate School
   Monterey, California